Title
Cold Pools, Effective Buoyancy, and Atmospheric Convection

Author
Jeevanjee, Nadir

Publication Date
2016

Peer reviewed|Thesis/dissertation

Cold Pools, Effective Buoyancy, and Atmospheric Convection

by

Nadir Jeevanjee

A dissertation submitted in partial satisfaction of the

requirements for the degree of

Doctor of Philosophy

in

Physics

in the

Graduate Division

of the

University of California, Berkeley

Committee in charge:

Professor David M. Romps, Co-chair
Professor Jonathan Wurtele, Co-chair
Professor William D. Collins
Professor Robert Jacobsen

Spring 2016

Cold Pools, Effective Buoyancy, and Atmospheric Convection

Abstract

Cold Pools, Effective Buoyancy, and Atmospheric Convection

by

Nadir Jeevanjee

Doctor of Philosophy in Physics

University of California, Berkeley

Professor David M. Romps, Co-chair

Professor Jonathan Wurtele, Co-chair

'Cold pools' are pools of air that have been cooled by rain evaporation, and which subsequently slump down and spread out across the Earth's surface due to their negative buoyancy. Such cold pools, which typically arise from rain produced by convection, also feed back upon convection by kicking up new convection at their edges.

This thesis studies the interaction of cold pools and convection at two levels of detail: on one end, we study the dynamics and thermodynamics of a single, idealized cold pool, and on the other, we study the interplay between a steady-state ensemble of convection and the many cold pools that accompany it. A recurring notion is that of 'effective buoyancy', which is the *net* acceleration experienced by a density anomaly such as a cold pool, including the back-reaction of the environment (i.e. the 'virtual mass effect') which reduces the net acceleration from its Archimedean value. We derive analytical formulae for the effective buoyancy of cold pools and other roughly cylindrical density anomalies, and use the same framework to understand the forces at play when cold pools trigger new convection. We also analyze the sizes and lifetimes of cold pools, and examine the impact of cold pools on the organization (i.e. clustering) of convection.

To My Parents

Contents

List of Figures

List of Tables

Acknowledgments

This long journey could not have been completed without the patience, forbearance, and support of loved ones, the faith and firm push of a wise and caring advisor, and the help and fellowship of wonderful colleagues. Many thanks are due to all of them.

Chapter 1

Introduction

Convection is the primary means by which the Earth's surface cools itself. In the annual and global mean, the surface absorbs roughly 150 W/m^2 of sunlight, but re-reradiates away (in the infrared) only 50 W/m^2 of that because of strong, opposing downwelling infrared radiation from the atmosphere (i.e., the greenhouse effect). The remaining $\sim$ 100 W/m^2 is carried away from the surface by convection, mostly in the form of latent heat associated with water vapor that has evaporated from the surface [28].

Despite its importance in the planetary energy balance, however, much about convection remains ill-understood. We are uncertain about many things, including:

1. How clouds are initiated
2. Why and how they sometimes 'clump' together, i.e. organize
3. How they mix with their environment
4. What sets their vertical velocity
5. How suspended cloud condensate grows to form precipitation

Furthermore, this inability to understand clouds in the present day precludes accurate predictions about how clouds will change with global warming. Since global climate models (GCMs) cannot resolve clouds explicitly, they must 'parameterize' them, i.e. make their best guess about what clouds will do under any given circumstance. Since the questions above are (like the clouds) unresolved, these guesses vary quite widely between models, and hence so do the models' representation of clouds and their changes with warming. Furthermore, since clouds can both strongly reflect sunlight as well as strongly enhance the greenhouse effect, these uncertain changes in clouds have large climate implications. In fact, clouds are the dominant source of uncertainty in global warming projections [5], a lingering state of affairs that has persisted for over a generation [10].

Progress will likely require a bottom-up approach of understanding the various phenomena listed above, from as theoretical a point-of-view as possible. This is a long-term project

ranging over many subfields of physics (fluid mechanics, thermodynamics, radiation, etc.), and much work will be required before even any one of the questions above will be answered satisfactorily enough such that GCMs do not significantly vary in how the corresponding process is parameterized.

Our goal in this thesis, then, will be to focus on one or two of the questions listed above, and to try and add some validated mathematical and physical understanding to our picture of the relevant phenomena. Even if we achieve our goal, it will not immediately reduce uncertainty in estimates of global warming, nor will it allow us to revise these estimates, but it will put us a few steps closer to having cloud parameterizations that are grounded in process-based understanding, rather than inspired guesswork.

That said, we will focus on convective triggering (question 1) and convective organization (question 2) in this thesis. Both of these phenomena impact the general climate as well as particular variables of interest, such as temperature and precipitation. Convective triggering, for instance, is crucial for the variability of precipitation. The upper atmosphere is often unstable and hence would permit convection and the accompanying precipitation, but this is suppressed by a stable layer near the surface which inhibits convection. A triggering mechanism is required to overcome this stability, and so an understanding of what triggers convection and how should lead to better understanding and modeling of the variability of convection and precipitation. This variability is typically underestimated by current GCMs [e.g. 43], whose convective parameterizations [such as the Zhang-McFarlane scheme, ref. 83] do not necessarily take triggering into account.

As for organization, it is has been observed that organized systems such as mesoscale convective systems [MCSs, see e.g. 57] are major contributors to total rainfall [21] and extreme rainfall [72]. Furthermore, MCSs decrease the water-vapor greenhouse effect by drying out their environment [77]. Despite their importance for precipitation and climate, however, MCSs are not currently represented with any fidelity in GCMs, and it has been suggested that this could be an important missing feedback [50]. Thus, a better understanding of MCSs and organized convection in general is clearly desirable.

A common thread between the phenomena of triggering and organization are 'cold pools', which are pools of air near the surface that have been cooled by rain evaporation, and subsequently slump down and spread out due to their negative buoyancy; see Fig. 1.1. These cold pools are produced by convection via the associated rainfall, but also feed back upon convection by triggering new convection at their edges (see [78] and Fig. 2.2 below). It is also know that when convection is organized, cold pools can negatively feed back upon this organization [57]. Given this close interplay between convection and cold pools, then, we pose the following questions:

1. What are the forces that produce new convection at a cold pool's edge? Is the triggering mechanical in nature, so that new convection is 'pushed up' by the outflow at the cold pool's edge? Or, does the temperature contrast between a cold pool and its environment mean that air near the cold pool edge feels an enhanced buoyant acceleration? It has also been observed [78, 42] that the edges of cold pools are anomalously

moist; does this also play a role in triggering, perhaps via the 'virtual effect', i.e. the fact that water vapor is lighter than dry air and hence moist air is more buoyant?

2. What are the dynamics of cold pools themselves? General arguments [32] show that parcels with large aspect ratios – i.e., that are much wider than they are tall – experience a marked reduction of acceleration from the naive Archimedean value, because they must push significant amounts of environmental air out of their way as they accelerate [the 'virtual mass' effect, 18, not to be confused with the virtual effect of water vapor discussed above]. This effect is well-known but has not been straightforward to estimate without involved numerical calculation. Cold pools certainly exhibit large aspect ratios – is there a way to estimate the effect of this on their acceleration? And does their close proximity to the surface alter this effect?

3. What is the thermodynamic evolution of a cold pool? The surface will typically warm a cold pool as the cold pool traverses it, ultimately 'killing' the cold pool by warming it up to the ambient temperature. Both numerical and observational studies show that this typically happens after 2-3 hours, at a radius of order ~ 10 km [e.g. 78, 84]. What determines these length and time scales?

4. Idealized numerical simulations show that even without external forcing, convection can spontaneously clump together, or 'self-aggregate'. This only happens, however, when the horizontal dimensions of the simulation are greater than ~ 300 km. What is the role, if any, of cold pools in determining this critical length scale? And why is it domains *larger* than this length scale that favor self-aggregation?

These questions will be addressed in Chapters 2-5, respectively. A summary and discussion of future work is given in Chapter 6.

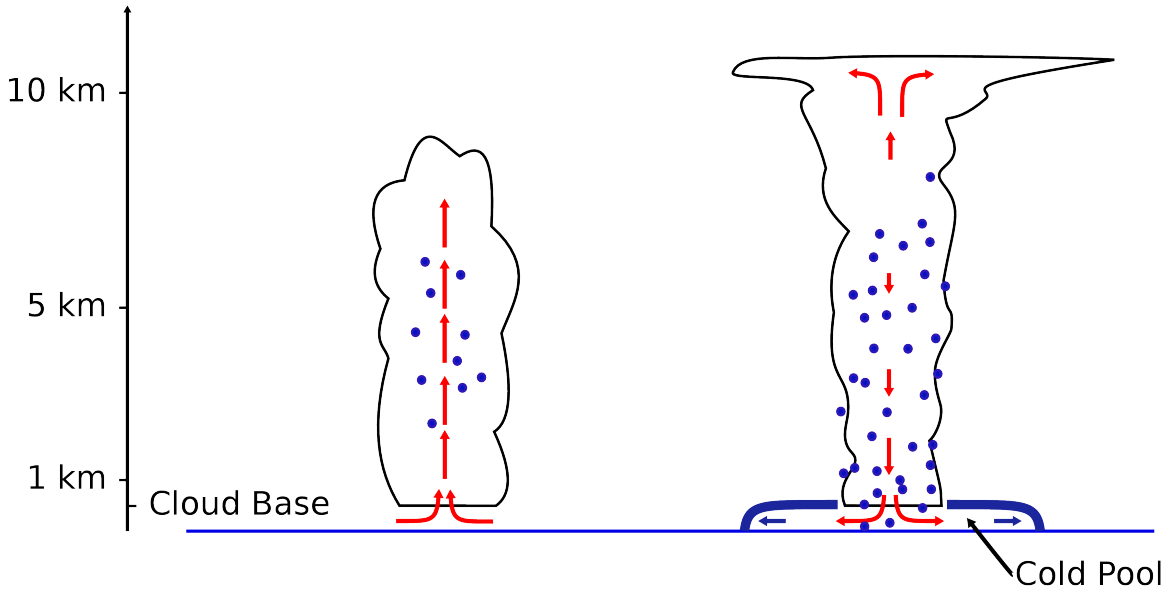

Figure 1.1: Schematic of convection and cold pool generation. **Left**: As a cloud grows, water condenses and is lofted up along with the rising air (red arrows). **Right**: As the cloud mature some of the condensed water begins to fall as rain. Some of this rain evaporates on the way down, creating negatively buoyant air which begins to descend (red arrows). When this air reaches the ground it slumps down and spreads out, forming a cold pool. Figure courtesy Wolfgang Langhans.

Chapter 2

Effective Buoyancy, Inertial Pressure, and the Mechanical Triggering of Convection by Cold Pools

2.1 Introduction

The initiation of convection is an outstanding and pressing issue in cloud dynamics. Clarification of the mechanisms involved is necessary for the construction of reliable convective parameterizations in global climate models, and in particular for reliably 'closing' mass flux schemes, which must diagnose cloud-base mass flux in terms of prognostic variables. Many current mass flux schemes, such as the Zhang-McFarlane scheme [83] currently employed in the Community Atmosphere Model[1] [55], have closures that rely on uncertain convective timescale parameters, to which the parent models exhibit considerable sensitivity [61, 51, 52]. Thus, a firm understanding of how convection is initiated is critical for trustworthy convective parameterizations and accurate simulations of global climate.

Though convection can take many forms (e.g., trade cumulus, squall lines, mesoscale convective systems) and is variously influenced by the large-scale environment (e.g., surface temperature gradients, wind shear, and large-scale vertical motion), the mass flux closure problem remains unsolved even in the simple case of unorganized radiative-convective equilibrium (RCE) over an ocean with uniform temperature[2]. It is known, however, that in cloud-resolving-model (CRM) studies of RCE, convection is preferentially triggered at cold-pool gust fronts, as demonstrated by [78] (hereafter T01). Thus, a closer study of what happens at such gust fronts is necessary to understand how convection in RCE is generated.

[1]The Community Atmosphere Model is the atmospheric component of the Community Earth System Model, one of two state-of-the-art American climate models participating in the Intergovernmental Panel on Climate Change's global warming assessments [35].

[2]RCE simulations typically feature periodic boundary conditions in the horizontal, so that the atmosphere is energetically closed, with energy coming in from the surface in the form of latent heat of water vapor and escaping to space via infra-red radiation.

That gust fronts in general can trigger convection (i.e., generate boundary-layer plumes with significant vertical velocity) is well known, e.g., from the study of squall lines [81] or midlatitude continental convection [16]. In these cases it has generally been assumed that the triggering is dynamical in nature, i.e., that it arises from horizontal convergence at the gust front. For oceanic RCE, however, T01 noted that the thermal recovery of mature cold pools, along with pronounced moisture anomalies at the gust front, yield a dramatic reduction in convective inhibition (CIN) and enhancement of convective available potential energy (CAPE) there, pointing to a strong thermodynamic role for cold pools in organizing convection. While neither CIN nor CAPE directly relate to the generation of boundary-layer mass flux, the thermal recovery of the mature cold pools pointed out by T01, along with the virtual effect due to the moisture anomalies at the gust front, raise the possibility that there is a significant buoyant contribution to the initial triggering. Our main goal in this paper is to assess this possibility, by evaluating the relative roles of mechanical and thermodynamical forces in generating mass flux at cold-pool gust fronts in oceanic RCE. We will focus on how low-level ($z = 300$ m) mass flux is generated, and leave aside for the time being the question of how that low-level mass flux relates to cloud-base mass flux. Answering the latter question will be critical for solving the mass flux closure problem discussed above, and our work here can be seen as a first step in that direction.

Assessing the relative roles of thermodynamical and mechanical accelerations will require us to define these quantities, so we propose here the following simple definitions. We define the *vertical buoyant acceleration* [or 'effective buoyancy', [13], hereafter DJ03] a_b to be the Lagrangian acceleration that would result if the wind fields were instantaneously zeroed out, i.e.

$$a_b \equiv \left.\frac{dw}{dt}\right|_{\mathbf{u}=0} \tag{2.1}$$

where $\mathbf{u} = (u, v, w)$ is the wind field. Up to a factor of $\overline{\rho}(z)$ (a reference density profile), this will be our 'thermodynamic force'. We analogously define the *vertical inertial acceleration* a_i to be the Lagrangian vertical acceleration resulting from an instantaneous zeroing out of any horizontal density anomalies, i.e.

$$a_i \equiv \left.\frac{dw}{dt}\right|_{\rho=\overline{\rho}} \tag{2.2}$$

where ρ is the system density (including the weight of hydrometeors). Up to a factor of $\overline{\rho}$ this will be our 'mechanical' or 'dynamical' force, though it is really due entirely to inertia, as we will see.

We will show in the next section that $\frac{dw}{dt} = a_b + a_i$ and that a_b and a_i depend entirely on density and wind fields, respectively, and thus comprise a suitable decomposition of vertical force into thermodynamic and mechanical components. Mathematically equivalent decompositions are somewhat well-known and have been considered by previous authors [e.g., DJ03; 82, 39], but the definitions (2.1) and (2.2) are new. In addition to bearing a simple physical interpretation, these definitions also yield unambiguous boundary conditions

for a_b and a_i, which are often imposed by hand [DJ03; 38] and can be a source of ambiguity [see 49, pg.29].

A central feature of the definition (2.1) is that the buoyant acceleration a_b includes both the Archimedean buoyancy B as well as the environmental response to the accelerations produced by B. We will see that a_b can be very different in magnitude and spatial distribution than B, to the degree that B cannot always be considered a first approximation for a_b. Thus, a proper determination of the character of convective triggering by cold pools depends crucially on considering a_b rather than B, as advocated by [15].

We begin by using the definitions (2.1) and (2.2) to derive diagnostic Poisson equations for a_b and a_i. With a proper force decomposition in hand, we then run a CRM in RCE and diagnose a_b and a_i at cold pool gust fronts and across the entire domain. From this, we derive evidence that the inertial acceleration a_i is the primary driver behind tropical convective triggering, and give a simple argument for why this should be. Our argument suggests that in the absence of cold pools a_b may dominate; we confirm this by running a shallow-to-deep convection simulation, during which the dominant forcing transitions from a_b to a_i as precipitation sets in and cold pools appear.

2.2 Buoyant and Inertial accelerations

Vertical force decomposition

We begin by deriving diagnostic equations for a_b and a_i. Our starting point is the anelastic momentum equation

$$\overline{\rho}\frac{d\mathbf{u}}{dt} = -\nabla p - \rho g\hat{\mathbf{z}} \tag{2.3}$$

where p is the pressure and g the gravitational acceleration. There is no Coriolis term as we are considering equatorial, oceanic RCE. A common approach is to approximate (2.3) by introducing a reference pressure profile $\bar{p}(z)$ in hydrostatic balance with $\overline{\rho}$, along with accompanying perturbations $p' \equiv p - \bar{p}$ and $\rho' \equiv \rho - \overline{\rho}$, which leads to

$$\frac{d\mathbf{u}}{dt} = B\hat{\mathbf{z}} - \frac{1}{\overline{\rho}}\nabla p' \tag{2.4}$$

where $B \equiv -\rho' g/\overline{\rho}$ is the usual Archimedean buoyancy. Here, however, we follow the approach taken in DJ03 and [12] and alternatively decompose the pressure field as

$$p = p_{\mathrm{h}} + p_{\mathrm{nh}}\,, \tag{2.5a}$$

$$\text{where} \quad p_{\mathrm{h}} \equiv \int_z^\infty dz' \rho g\,, \tag{2.5b}$$

so that p_{h} is the *local* hydrostatic pressure field and p_{nh} is the local non-hydrostatic pressure field. Plugging this into (2.3) yields

$$\overline{\rho}\frac{d\mathbf{u}}{dt} = -\nabla p_{\mathrm{nh}} - \nabla_h p_{\mathrm{h}}\,, \tag{2.6}$$

where $\nabla_h = \partial_x \hat{\mathbf{x}} + \partial_y \hat{\mathbf{y}}$ and we have an exact cancellation between the gravitational force and $-\partial_z p_{\rm h}$. The z-component of (2.6) is simply

$$\overline{\rho} \frac{dw}{dt} = -\partial_z p_{\rm nh} \,, \tag{2.7}$$

so the Lagrangian vertical acceleration is given by $1/\overline{\rho}$ times the non-hydrostatic vertical pressure gradient force $-\partial_z p_{\rm nh}$. [This result also dates back to [45] and [12].]

To apply the definitions (2.1) and (2.2), we must diagnose $\partial_z p_{\rm nh}$. This can be achieved by taking the divergence of both sides of (2.6) and invoking anelastic mass continuity, which yields the Poisson equation

$$-\nabla^2 p_{\rm nh} = \nabla \cdot [\overline{\rho}(\mathbf{u} \cdot \nabla)\mathbf{u}] + \nabla_h^2 p_{\rm h} \tag{2.8}$$

where ∇^2 is the usual three-dimensional Laplacian and $\nabla_h^2 \equiv \partial_x^2 + \partial_y^2$. Here, as in subsequent equations, we write the Laplacian term with a minus sign so that positive values on the right-hand side of the Poisson equation tend to generate positive responses in the solution (in this case, the solution for $p_{\rm nh}$). Applying $-\partial_z$ to (2.8) yields

$$-\nabla^2 \left(-\partial_z p_{\rm nh}\right) = -\partial_z \nabla \cdot [\overline{\rho}(\mathbf{u} \cdot \nabla)\mathbf{u}] + g \nabla_h^2 \rho, \tag{2.9}$$

where we used the definition (2.5b) of $p_{\rm h}$.

We can now combine the diagnostic equation (2.9) with the result (2.7) and the definition (2.1) to obtain a Poisson equation for a_b:

$$-\nabla^2 (\overline{\rho} a_b) = g \nabla_h^2 \rho. \tag{2.10}$$

Some remarks on this equation are in order. Note that it is horizontal density variations, as opposed to more general thermodynamic variations, that give rise to a_b, which is why we refer to it as a 'buoyant' acceleration rather than a more general 'thermodynamic' acceleration. Also, up to the factor of $\overline{\rho}$ which makes our a_b an acceleration rather than a force per volume, (2.10) is identical to Eqn. (6) of DJ03, so we adopt his nomenclature and alternatively refer to a_b as the 'effective buoyancy'. Finally, an alternative diagnostic expression for the effective buoyancy can be obtained via (2.4); this is the approach used by most other authors [e.g., 15, 82, 39], and we will compare and contrast these approaches in Appendix A.1.

Next, we turn to the diagnosis of the inertial acceleration a_i. Combining (2.9), (2.7), and (2.2) yields the desired expression:

$$-\nabla^2 (\overline{\rho} a_i) = -\partial_z \nabla \cdot [\overline{\rho}(\mathbf{u} \cdot \nabla)\mathbf{u}]. \tag{2.11}$$

Note that a_i is sourced by the advection of momentum, which is nothing but inertia, which is why we refer to a_i as an 'inertial' acceleration. This quantity has appeared in the literature many times before, most often as the z-component of a 'dynamic' pressure gradient [e.g., 49, 70, 38]. It will be both computationally and conceptually expedient for us to also consider

$\overline{\rho}a_i$ as the vertical component of a pressure gradient. We will refer to the corresponding pressure field as the 'inertial pressure', denoted p_i, and we give the details of its definition, interpretation, and computation in Appendix A.2.

Note that the determination of a_b and a_i via the Poisson equations (2.10) and (2.11) is incomplete without boundary conditions (BCs). We will be considering an atmosphere with rigid bottom ($z = 0$) and top ($z = z_t$), so that $w = 0$ at $z = 0$ and $z = z_t$. Equation (2.7) then implies $-\partial_z p_{\rm nh} = 0$ at heights 0 and z_t. These BCs are unchanged by setting $\mathbf{u} = 0$ or $\rho = \overline{\rho}$, and so the definitions (2.1) and (2.2) yield the Dirichlet BCs $a_b = a_i = 0$ at $z = 0$ and $z = z_t$.

Finally, we observe that by Eqns. (2.10), (2.11), and (2.9), $\overline{\rho}a_b + \overline{\rho}a_i$ obeys the same Poisson equation as $-\partial_z p_{\rm nh}$. Furthermore, both quantities have the same BCs. This tells us that $\overline{\rho}a_b + \overline{\rho}a_i = -\partial_z p_{\rm nh}$, and (2.7) then implies

$$\frac{dw}{dt} = a_b + a_i. \tag{2.12}$$

Equation (2.12) is the desired decomposition of the vertical acceleration into buoyant and inertial components. Mathematically equivalent forms of (2.12) can be found elsewhere in the literature, e.g. [49] Eqn 10.15, [39], and [82], and the derivation given here closely follows that given in DJ03 in many respects. The novel elements are the definitions (2.1) and (2.2), which yield unambiguous boundary conditions for a_b and a_i and give them a simple physical interpretation.

Contrasting Archimedean and effective buoyancies

Before describing our experiments and their results, let us get a feel for how the effective buoyancy a_b works and how it differs from Archimedean buoyancy (some intuition for a_i and p_i is developed in Appendix A.2). From (2.10) we see that a_b is sourced by the horizontal Laplacian of ρ, so that buoyant accelerations tend to be strongest at *local* extrema of density (or, more generally, regions of $g\nabla_h^2\rho \neq 0$), rather than at density anomalies defined relative to an arbitrary reference value (as with B). This means that the a_b of a parcel is defined *relative to its immediate surroundings*, so that a very warm parcel surrounded by other warm air may accelerate less than a moderately warm parcel surrounded by cool air.

Since (2.10) is a Poisson equation, effective buoyancy is non-local: that is, localized extrema of density give rise to accelerations everywhere, even where $B = 0$. This is, of course, because any localized acceleration must (by mass continuity) be accompanied by compensating accelerations in the rest of the atmosphere. These compensating accelerations (see Appendix A.1 for their definition) often oppose the buoyancy field B that gives rise to them [49, 32], yielding a reduced net acceleration for air with significant B. For isolated regions of significant buoyancy, we thus expect that $|a_b| < |B|$.

These aspects of a_b are illustrated by Figure 2.1, which shows x-z cross sections of B and a_b for two Gaussian bubbles of the form

$$\rho = \overline{\rho}(z) + \delta\rho \, \exp[-(r/r_0)^n - (z/z_0)^n]$$

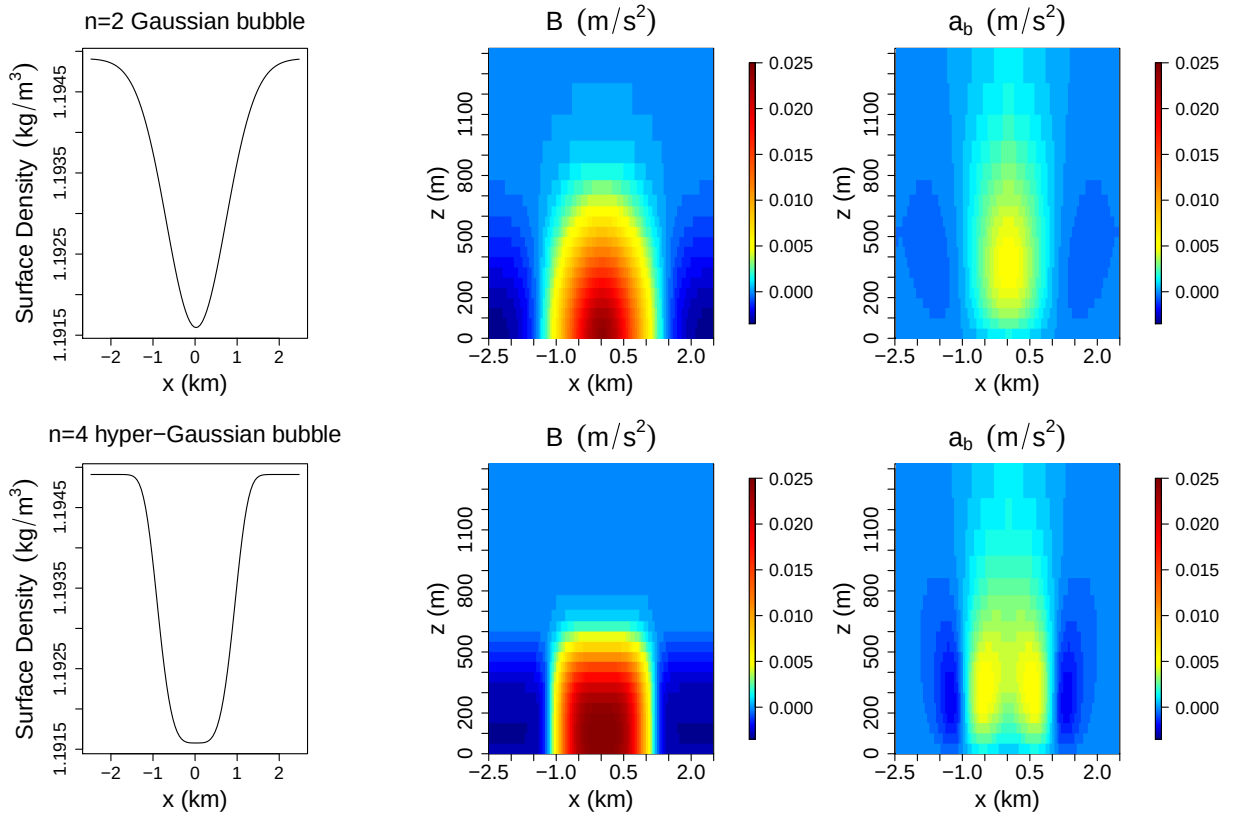

Figure 2.1: An x-z cross-section of Archimedean buoyancy B and effective buoyancy a_b for Gaussian ($n = 2$) and hyper-Gaussian ($n = 4$) density perturbations of the form $\exp[-(r/r_0)^n - (z/z_0)^n]$. The shape of the density perturbations at the surface is given in the left-most panels, and the precise form is given in the text. Note that a_b is only a fraction of B throughout most of both bubbles, and that a_b is non-zero above $z \sim 1000$ m, where $B \approx 0$. Also note the double peak in a_b for the broad $n = 4$ distribution.

for $n = 2$ and 4. Here, $r_0 = 1$ km, $z_0 = 500$ m, and $\delta\rho = \overline{\rho}(0)/300$, where $\overline{\rho}(z)$ is taken from our RCE simulations described below. We calculate B with respect to the horizontal average of ρ rather than $\overline{\rho}$; the fact that such a choice is required, yet somewhat arbitrary, is yet another shortcoming of B [15].

Perhaps the most striking feature (for both values of n) of Figure 2.1 is the degree to which $|a_b| < |B|$, requiring a rather severe stretching of the color bar to render features of both fields visible. Another interesting feature of Figure 2.1, particularly for $n = 4$, is that for $z \gtrsim 1000$ m, $a_b \neq 0$ even though $B \approx 0$. As discussed above, this is because a_b not only accelerates the bubble but also sets up the accompanying environmental circulation.

Finally, for $n = 4$, one can calculate that $\nabla_h^2 \rho$ is a maximum near the 'shoulder' of the density distribution at $r \approx 500$ m, and Figure 2.1 shows a corresponding maximum there in

the a_b field as well. This is to be contrasted with the B field, where the maximum is found at $r = 0$, where ρ itself has a minimum. Again, this is because net thermodynamic accelerations are a function of how buoyant a parcel is relative to its immediate surroundings, and so when the peak of the density distribution is too broad, the parcels there feel less acceleration than their counterparts at the shoulder of the distribution. Thus, the spatial distribution of a_b can indeed differ from that of B; we will see even more dramatic examples of this in the next section.

2.3 RCE simulations

With a preliminary understanding of a_b in hand, we can proceed to investigate whether a_b or a_i dominates the triggering of deep convection by cold pools in CRM simulations of RCE. This section describes the numerical model used, as well as our specific case set-up. We also briefly describe our calculation of a_b and a_i; this is discussed in greater detail in Appendix A.2.

Our cloud-resolving simulations were performed with Das Atmosphärische Modell (DAM) [63]. DAM is a three-dimensional (3-D), fully-compressible, non-hydrostatic cloud-resolving model, which employs the six-class[3] Lin-Lord-Krueger microphysics scheme [44, 46, 40]. Radiation is interactive and is calculated using the Rapid Radiative Transfer Model [53]. We rely on implicit LES [48] for sub-grid scale transport, and thus no explicit sub-grid scale turbulence scheme is used.

Our RCE simulations ran on a square doubly-periodic domain of horizontal dimension $L = 51.2$ km, with a horizontal resolution of $dx = 100$ m. The vertical grid stretches smoothly from 50 m resolution below 1200 m to 100 m resolution above, up to the model top at 30 km. We ran with a fixed sea-surface temperature of 300 K, and calculated surface heat and moisture fluxes using a bulk aerodynamic formula [20].

For a first diagnosis of a_b and a_i in RCE, we spun up the model for 60 days on an $L = 12$ km, $dx = 200$ m domain, then used the vertical profiles from this run to initialize a 13-day run on an $L = 51$ km, $dx = 200$ m domain. This run was then restarted with $dx = 100$ m and run for one more day to iron out any artifacts from changing the resolution. All data in the next section are from the end of this run.

We diagnose the effective buoyancy a_b directly from CRM output via the Poisson equation (2.10). We compute a_i slightly indirectly by first computing the inertial pressure p_i from CRM output via (A.4) and then using $a_i = -(\partial_z p_i)/\overline{\rho}$. We solve both Poisson equations by Fourier-transforming in the horizontal, which yields systems of algebraic equations that can be solved by inverting a tri-diagonal matrix. As discussed in Section 2.2, the fact that $w \equiv 0$ at model top and bottom yields Dirichlet boundary conditions for a_b and Neumann boundary conditions for p_i. The implementation of the latter is somewhat subtle, however, and requires some care; see Appendix A.2 for details.

[3]This refers to the six forms that water takes in the scheme: vapor, non-precipitating liquid water, precipitating liquid water (i.e., rain), non-precipitating ice, snow, and graupel.

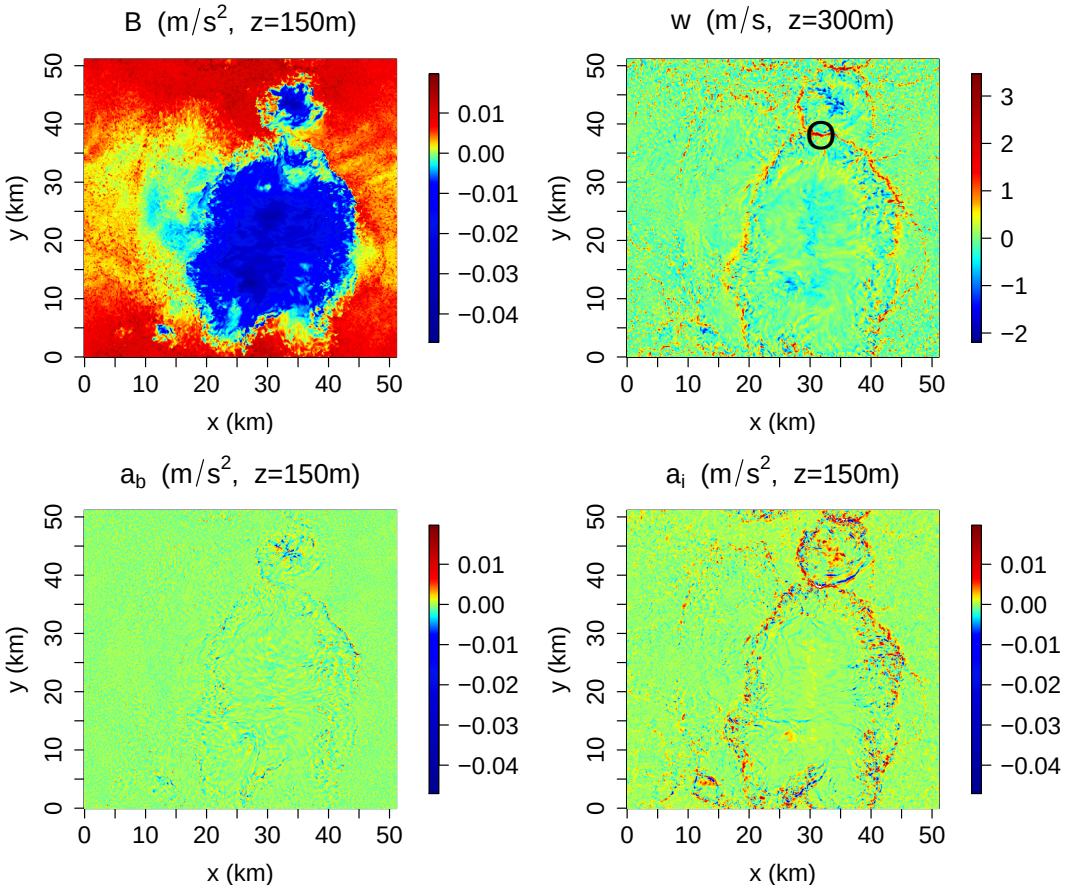

Figure 2.2: Plot of Archimedean buoyancy B, vertical velocity w, effective bouyancy a_b, and inertial acceleration a_i in the boundary layer for a CRM snapshot. Note that incipient convection ($w \gtrsim 1$ m/s) is almost entirely co-located with the cold pool boundaries visible in the B field, and that the vertical acceleration there appears strongly dominated by a_i. Note the stretched color bar for all accelerations. The '**O**' in the w plot marks the gust front whose transect is plotted in Figure 2.3.

2.4 RCE results

Plan views of the vertical velocity w at $z = 300$ m as well as the vertical accelerations B, a_i, and a_b at $z = 150$ m for a CRM snapshot are given in Figure 2.2. Cold pools are clearly visible in the B field, and incipient convection at the cold pool gust fronts is evident in the w field. Comparison of a_i and a_b suggests that this incipient convection is due primarily to a_i rather than a_b. Note the much reduced magnitude and differing spatial scales of a_b relative to B, again requiring a severely stretched color bar; in this circumstance, B is not even a first approximation for a_b. This drastic difference between a_b and B is a result of

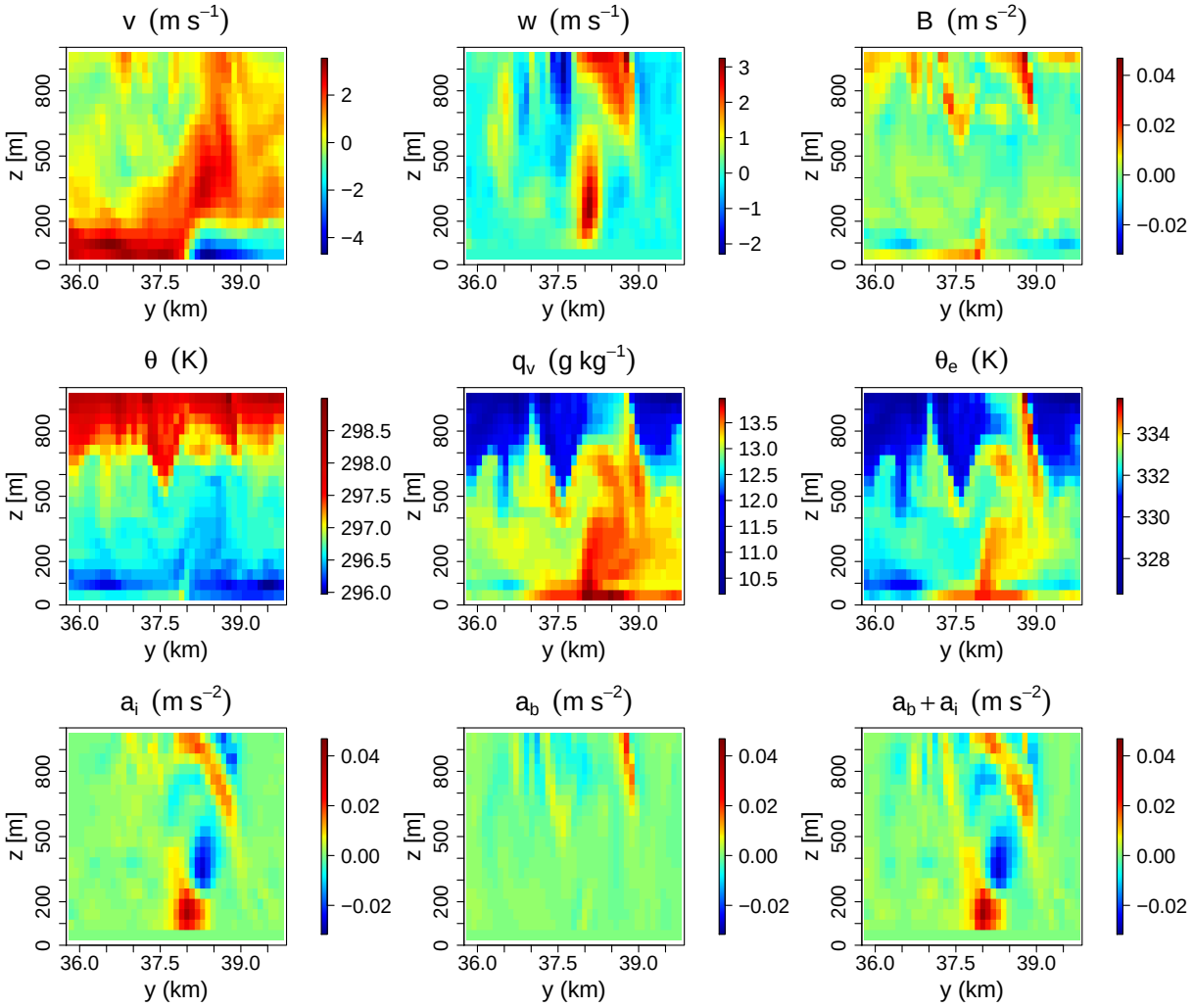

Figure 2.3: Plot of velocities v, w, Archimedean buoyancy B, potential temperature θ, specific humidity q_v, pseudoadiabatic equivalent potential temperature θ_e, inertial acceleration a_i, effective buoyancy a_b, and $a_b + a_i$ for cold pool transect. The nascent plume at $(x, y) =$ (38 km, 150 m), visible in the w field, lies just above the gust front evident in the u field. The plume has anomalously high θ, q, and B but is nonetheless triggered primarily by a_i. Note again the drastic differences in the a_b and B fields.

the extreme aspect ratio of the cold pools as well as their proximity to the ground, where an $a_b = 0$ boundary condition is enforced. Understanding this difference will be the focus of Chapter 3.

To further investigate the dominance of a_i over a_b, we take an y-z transect through a particular cold pool gust front from Figure 2.2 and plot various quantities for this transect

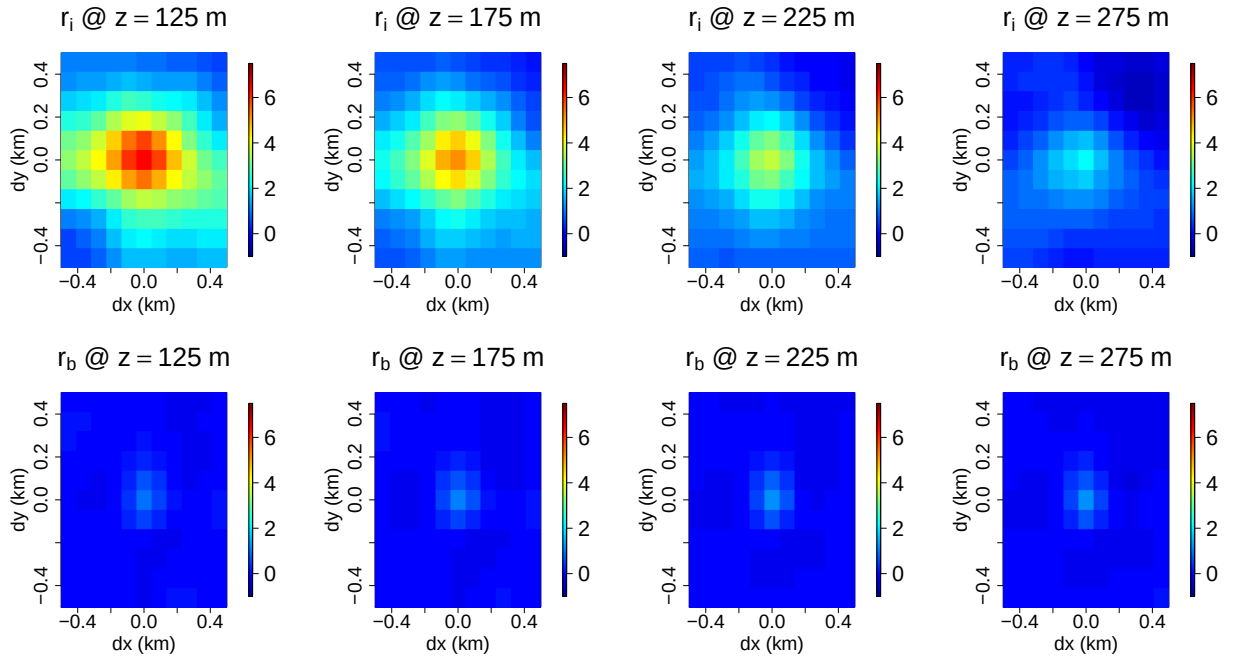

Figure 2.4: Regression coefficients r_i, r_b (units g/m^4) as defined in (2.13), plotted as a function of $(\delta x, \delta y)$ for various z. This more objective and comprehensive test again shows that a_i dominates over a_b.

in Figure 2.3. (This particular gust front is marked with an 'O' in the w plot of Figure 2.2.) We see a vigorous southward-moving cold pool with a gust front at $y \approx 38$ km, as well as a nascent plume ($w > 1$ m/s) just above at around $z = 300$ m. The warm, moist air feeding this plume from below is visible in the plots of Archimedean buoyancy B, potential temperature θ, water-vapor mixing ratio q, and equivalent potential temperature θ_e at $(y, z) \approx (38$ km, 150 m). The gust front and plume indeed exhibit anomalously high θ_e, as noted by T01. *Despite such thermodynamic enhancement, however, the plume's near-surface acceleration is strongly dominated by a_i.* Even when plotted on a stretched color scale, its buoyant acceleration a_b is barely discernible and is much reduced relative to its Archimedean buoyancy, consistent with our results from Section 2.2.

To quantitatively test the hypothesis that the a_i spike is responsible for the nascent plume, we check if w of the nascent plume at $z = 300$ m, which is about 2.5 m/s, is equal to $\sqrt{2a_i h}$ where h is the height of the a_i spike at the gust front. Taking $a_i \approx .02$ m/s^2 and $h \approx 200$ m gives $\sqrt{2a_i h} = 2.8$ m/s, which is consistent with the actual w.

We analyzed several other cold pools and came to similar conclusions. Still, a more comprehensive and objective test of the dominance of a_i is needed. To that end, we identify 'active' columns (defined here to be those (x, y) with $w(x, y, z = 300 \text{ m}) > 0.5$ m/s), and for these regress $\overline{\rho} a_i$ and $\overline{\rho} a_b$ evaluated at $(x + \delta x, y + \delta y, z)$, for various δx, δy, and $z < 300$ m,

against $w^2(x, y, 300\text{ m})$. This yields regression coefficients $r_b(\delta x, \delta y, z),\ r_i(\delta x, \delta y, z)$ which are least-squares fits to

$$\begin{aligned} a_b(x+\delta x, y+\delta y, z) &= r_b(\delta x, \delta y, z) \cdot w^2(x, y, 300\text{ m}) + C_b \\ a_i(x+\delta x, y+\delta y, z) &= r_i(\delta x, \delta y, z) \cdot w^2(x, y, 300\text{ m}) + C_i \end{aligned} \tag{2.13}$$

where the intercepts $C_b,\ C_i$ are negligible and ignored henceforth. We use w^2 rather than w because (by the work-energy theorem) a linear relationship with the forces is expected only for w^2. We regress the forces on w^2, rather than the other way around, because we want the regression coefficient to be directly proportional, rather than inversely proportional, to the magnitude of the forces. Maps of r_b and r_i as a function of $(\delta x, \delta y)$ and at various z are shown in Figure 2.4. [The units and order of magnitude of the coefficients are given by $\rho/2h = (1.2\text{ kg/m}^3)/(2 \times 200\text{m}) = .003\text{ kg/m}^4$.] These maps show clearly and objectively the dominance of a_i over a_b in generating new mass flux in the boundary-layer, and comprise our main numerical result.

2.5 Why does a_i dominate?

The previous section presented anecdotal as well as systematic evidence that a_i dominates over a_b in triggering new low-level mass flux in a simulation of deeply convecting RCE. It remains, however, to gain some insight as to why this should be. In this section we will estimate the ratio of a_i to a_b at a cold pool gust front by estimating the ratio of the relevant source terms in their respective Poisson equations. We justify this approach by noting that variations in a_b and a_i at the gust front occur over the same length scales and so $\nabla^2 a_i / \nabla^2 a_b \approx a_i / a_b$.

First consider the source term $S_{a_i} \equiv -\partial_z \nabla \cdot [\overline{\rho}(\mathbf{u} \cdot \nabla)\mathbf{u}]$ for a_i in (2.11). This can be re-written as

$$S_{a_i} = \partial_z \left[\overline{\rho}\, (\partial_j u_i)(\partial_i u_j) - \overline{\rho}\, w^2 \partial_z^2 \ln \overline{\rho} \right]. \tag{2.14}$$

To analyze this, note that the scale of $\overline{\rho}$ variations is much larger than those for the velocities, so we can neglect derivatives of $\overline{\rho}$. This leaves us with

$$S_{a_i} = \overline{\rho}\, \partial_z \left[(\partial_j u_i)(\partial_i u_j) \right]. \tag{2.15}$$

Let us evaluate this at a gust front boundary, where U is a typical horizontal velocity of the front, W is a typical vertical velocity of a triggered updraft, h is a typical height of the front, and L is the length over which u and B transition from their cold pool values to their ambient values. (From the surface level in Figure 2.3 this is evidently the grid spacing dx, though we will see that our argument is resolution-independent.) Then every $i = 1$ or 2 in (2.15) yields a factor of U/L, and every factor of $i = 3$ yields a factor of W/h, which equals U/L by continuity. The same is true for j. The ∂_z contributes a factor of $1/h$, and so we can estimate (2.15) as

$$S_{a_i} \approx 9 \overline{\rho} \frac{U^2}{L^2 h}.$$

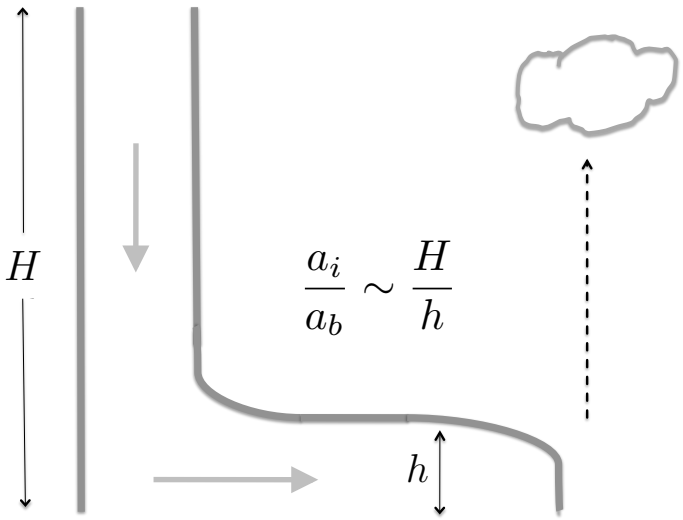

Figure 2.5: Cartoon depicting the dominance of a_i over a_b as resulting primarily from the ratio of downdraft height H to gust front height h, as in Eqn. (2.17).

Similarly, the source term for a_b is given by

$$S_{a_b} \equiv g\nabla_h^2 \rho \approx 2g\frac{\rho'}{L^2}\,,$$

where ρ' is a characteristic density anomaly for a cold pool. Taking the ratio of our expressions for S_{a_i} and S_{a_b} gives

$$\frac{S_{a_i}}{S_{a_b}} \approx \frac{9U^2}{2Bh} \tag{2.16}$$

where B is a characteristic magnitude of Archimedean buoyancy for the cold pool. To evaluate (2.16) we use the empirical observation [26] that for a lock-release density current, the 'total-depth' Froude number $\mathrm{Fr}_H \equiv U/\sqrt{B_0 H}$ is roughly equal to 1/2, independent of time and H.[4] Here H is a characteristic height for the negatively buoyant downdraft which spawned the cold pool, and B_0 is the magnitude of the cold pool's initial buoyancy (typically $B_0 \gtrsim B$). Plugging $U^2 = 0.5B_0H$ into (2.16) gives

$$\frac{S_{a_i}}{S_{a_b}} \approx \frac{9}{4}\frac{B_0 H}{Bh} > 1. \tag{2.17}$$

[4]More specifically, if the initial slug has a radius R_0 then Fr_H is roughly constant until the gust front reaches $8-10\ R_0$, at which point the cold pools in our simulation have transitioned to warm pools.

This is our main theoretical result. Taking typical values of $H = 800$ m, $h = 200$ m, $B_0 = 0.02$ m/s^2, and $B = 0.01$ m/s^2 gives a ratio of about 18, implying that, at the gust fronts, a_i is larger than a_b by about an order of magnitude. This corresponds roughly to what we see in Figures 2.2 and 2.3. A cartoon of this result, emphasizing the ratio of downdraft height H to gust front height h as a determining factor in the dominance of a_i over a_b, is given in Figure 2.5.

2.6 Shallow-to-deep simulation

Given that we have identified a_i as the dominant force component in the generation of boundary-layer mass flux in RCE, it is of interest to ask whether there are other settings in which a_b, rather than a_i, might dominate. One might expect that for shallow non-precipitating convection, the absence of cold pools would mean that the triggering of convection is primarily buoyant in nature.

To test this, we run a shallow-to-deep CRM simulation similar to that of [41], where we use the same model domain and grid spacing as for our RCE simulation above but initialize with a thermodynamic profile based on observations from the Barbados Oceanography and Meteorology Experiment (BOMEX)[5]. For heights between 0 and 3000 m we use the θ and q profiles given in the CRM intercomparison study of this case in [74]. We then simply (and somewhat crudely) extend the θ profile to above 3000 m by linearly interpolating (z, θ) to a tropopause at $(14000\text{ m},\ 350\text{ K})$ and then to the model top at $(30000\text{ m},\ 800\text{ K})$. We similarly extend the q profile via relative humidity RH by interpolating (z, RH) to $(14000\text{ m},\ 0.5)$ and then to $(30000\text{ m}, 0)$. These values roughly approximate those found in our RCE simulations. We fix the latent heat flux at 150 W/m^2 and sensible heat flux at 10 W/m^2, in accordance with [74]. Note the contrast with other studies of the shallow-to-deep transition, such as [41] and [4], where the transition is forced by time-dependent surface fluxes. Here, we are less interested in a realistic transition between shallow and deep convection as we are in contrasting their convective triggering mechanisms, and we deem this simple simulation sufficient for that purpose.

We run this simulation for two days, saving 3-hourly snapshots. For each snapshot, we calculate r_b and r_i as in (2.13) but set $\delta x = \delta y = 0$ for clarity. We thus get one value of r_b and r_i at each height for each snapshot, and time series of these (along with domain mean precipitation) are presented in Figure 2.6. Indeed, we see that a_b dominates while precipitation is negligible, and that a_i takes over as precipitation sets in; this confirms our expectation, and provides a clear hydrodynamical distinction between mass flux generation in the two regimes.

[5]This campaign observed the so-called 'trade cumulus' regime, wherein a temperature inversion around $z \sim 2000$ m caps convection at that height, inhibiting precipitation.

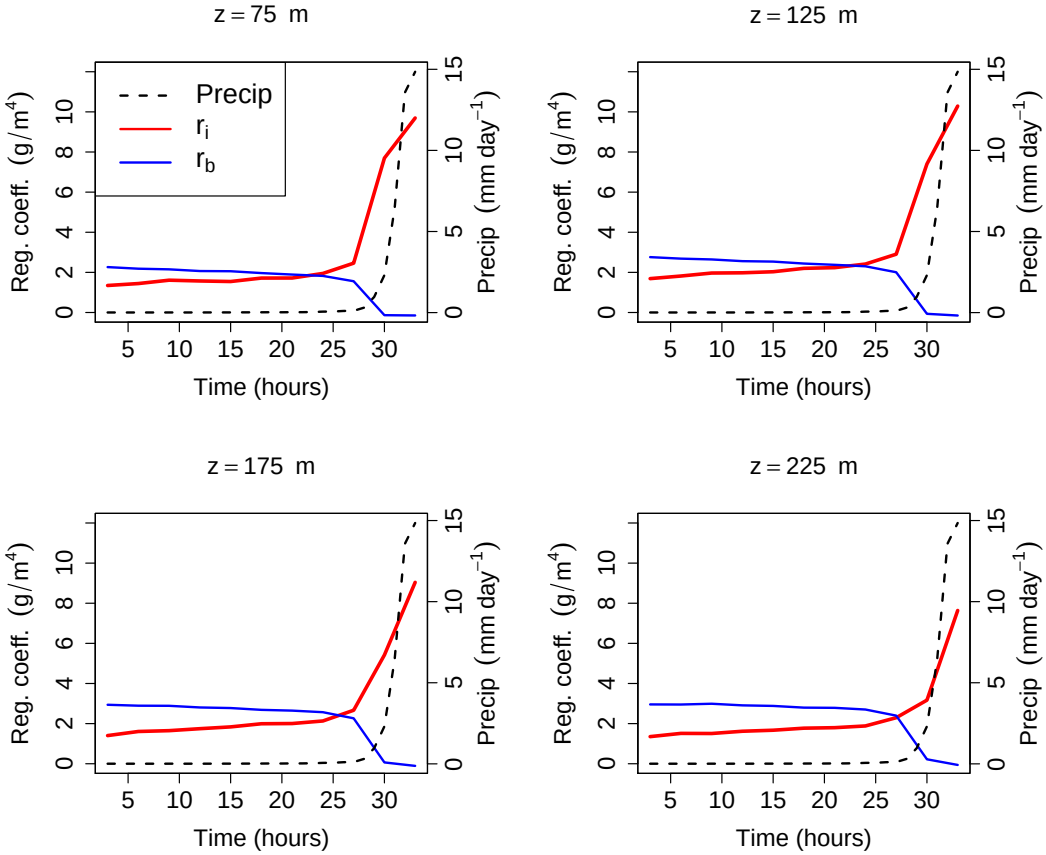

Figure 2.6: Time series of regression coefficients r_i and r_b, computed as in (2.13) for various z but with $\delta x = \delta y = 0$, along with precipitation time series, for the shallow-to-deep simulation. Note that a_b dominates before precipitation sets in, at which point a_i takes over.

2.7 Implications

We have used a carefully chosen formulation of the anelastic equations of motion to decompose vertical accelerations into inertial and buoyant components, and have used the resulting decomposition to analyze the triggering of low-level mass flux by cold pool gust fronts. This can be seen as a first step towards answering the question of how cloud-base mass flux is generated in the boundary layer of an atmosphere in deeply convecting RCE. Along the way, we have also developed some intuition for the inertial and buoyant accelerations, and have addressed some ancillary questions that arise in their interpretation and computation.

The notion of effective buoyancy, though not new, has received relatively little attention. The physics it embodies is well-known, in that it is widely acknowledged in the literature

that buoyant accelerations of parcels are reduced by back-reaction from the environment and that this effect depends on the horizontal extent of the parcel, but these effects are rarely computed explicitly. Furthermore, widely-used diagnostic quantities such as CAPE and CIN, which play central roles in various convective parameterizations [e.g., 83, 8], are based on easily calculated Archimedean buoyancy, rather than on the complete buoyant force.[6] Since the results presented here (and in particular Figures 2.1 and 2.2) suggest that Archimedean buoyancy can be highly inadequate in capturing buoyant acceleration, both in magnitude and spatial distribution, care must be taken in the quantitative application of such diagnostics. If a parcel's CIN, for instance, is a poor estimate of the negative buoyant acceleration it experiences as it makes its way to cloud-base, then there may be little theoretical justification for the CIN/TKE mass-flux closures employed in, e.g., [47] and [8]. There is thus a need for a simple yet quantitatively reliable way to estimate the effective buoyancy of a parcel given some additional datum about its spatial dimensions and proximity to the ground, and we pursue that in Chapter 3.

The other component of vertical force, the inertial pressure gradient $\overline{\rho} a_i = -\partial_z p_i$, seems to be more familiar than effective buoyancy, having in particular played a key role in the analysis of severe storms and tornadoes [e.g., 70, 38, 49]. Despite this exposure, though, p_i remains slightly enigmatic. There seems to be little discussion in the literature of p_i as an enforcer of mass continuity in the face of inertial motions, and how this implies that strain and vorticity generate p_i disturbances of opposing sign. Furthermore, the calculation of p_i via (A.4) raises issues of boundary-condition implementation and finite-difference interpolation that often go unmentioned, but actually require rather exquisite care. We have endeavored to fill these gaps in the interpretation and calculation of p_i in Appendix A.2.

Finally, our result that the inertial acceleration a_i dominates the low-level triggering of new mass flux provides a stepping stone to a more complete picture of mass flux generation in the boundary-layer. Though we have not made a precise connection between the low-level mass flux investigated here and cloud-base mass flux, a positive correlation is to be expected, and thus our results lend preliminary support to convective parameterizations in which the inertial triggering of mass flux at cold pool gust fronts takes center stage, as in [62].

Of course, many details remain to be filled in. For instance, although a_i dominates over a_b in the lower boundary layer, the transect in Figure 2.3 (as well as other transects we inspected) suggest that the force balance may shift as the plume rises, and that a_b may play a role in shepherding nascent plumes through the middle boundary layer and up to their lifting condensation levels. Quantifying this role would be necessary to complete the picture of cloud-base mass flux generation.

Apart from the generation of deep convective mass flux, there are other problems which might be fruitfully analyzed with the approaches taken here. It could be helpful to attempt a scaling estimate for a_i/a_b as in (2.17), but for shallow convection, where turbulent motions instead of cold pools are responsible for generating the heterogeneity in density and wind

[6] As computed via a_b, or by adding in the buoyancy perturbation pressure force $-\partial_z p'_b$, as per (A.1) below.

that generate a_b and a_i. Also, applying the force decomposition (2.12) to convection in the free troposphere could further refine our picture of the vertical momentum budget of thermals, as recently studied in, e.g., [80], [73], and [67].

Finally, we point out a similar recent study which also examines the relative influence of thermodynamic and mechanic properties of cold pools upon convective triggering [79]. Similar to this study, those authors also found that mechanical forces dominate over thermodynamic ones in triggering low-level mass flux. Furthermore, they employed a Lagrangian particle dispersion which allowed them to quantify the influence of cold pool thermodynamics in reducing particles' lifting condensation levels. They also introduced a novel algorithm for tracking the lifetimes of cold pools and the residence times of particles within them, providing new insights into the origins of mass flux triggered by cold pools.

Chapter 3

Effective buoyancy at the surface and aloft

3.1 Introduction

We pointed out in the last chapter that under some circumstances, the Archimedean buoyancy B is a poor approximation to the effective buoyancy β, which gives the true acceleration a density anomaly will experience due to its buoyancy. This was evident in Figs. 2.1 and 2.2, though in those figures it is unclear how much the discrepancy between B and β is due to aspect ratio effects, and how much might be due to (heretofore unstudied) surface effects.

To disentangle this we calculate B and β fields for Gaussian bubbles of a fixed aspect ratio but of variable distance from the ground. More specifically, we consider density distributions of the form

$$\rho(\mathbf{x}) = \overline{\rho}(z) + \Delta\rho \exp\left[-\frac{r^2}{R^2} - \left(\frac{z - z_{\rm cm}}{H/2} \right)^2 \right], \tag{3.1}$$

with height $H = 1000$ m, radius $R = 1000$ m, $\Delta\rho = -\overline{\rho}(z_{\rm cm})/300$ for an approximate temperature anomaly of 1 K, and bubble centers $z_{\rm cm} = 2000,\ 500$, and 0 m. Figure 3.1 shows x-z cross-sections at $y = 0$ of B and β for these bubbles.[1] The ratio of the maximum of β to the maximum of B is roughly 1/2 for the "free" bubble, and this ratio decreases rapidly as the bubble approaches the surface. At the surface one can also see that the maxima of β and B are no longer co-located.

Thus, surface effects can be as significant as aspect ratio effects. We lack simple formulae for estimating either of these effects, which is symptomatic of our fuzzy understanding of them. Our aim in this chapter is to remedy this by developing, testing, and understanding analytical expressions for the effective buoyancy of fluid parcels near the surface and aloft. We will solve the the Poisson equation for β given in [13] (hereafter DJ03) for idealized

[1] The domain set-up and $\overline{\rho}(z)$ for the bubbles is the same as for the large-eddy simulations discussed in section 3.5 below, and we compute β numerically as described in the last chapter.

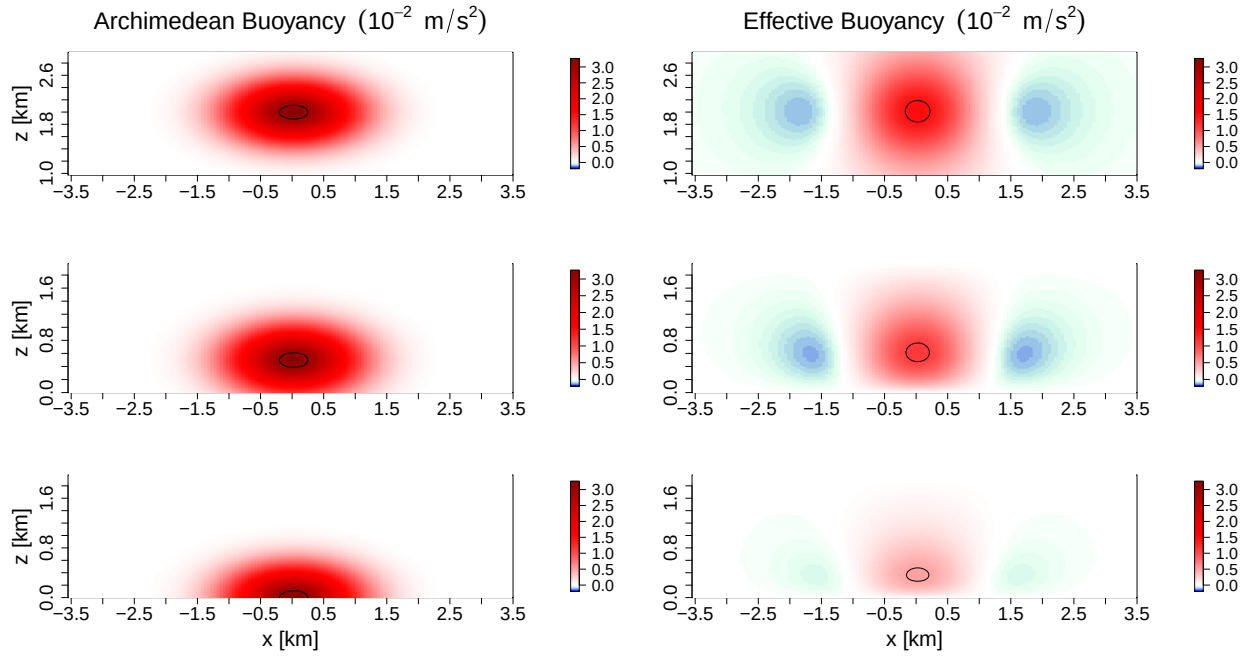

Figure 3.1: x-z cross sections at $y = 0$ of B and $\beta = B - (\partial_z p_b')/\overline{\rho}$ for Gaussian bubbles of the form (3.1) with $R = 1000$ m, $H = 1000$ m, and center height $z_{\text{cm}} = 2000,\ 500$, and 0 m, respectively. Horizontal and vertical dimensions are plotted to scale, though the vertical axis in the top row differs from that of the other rows. The lone contour is drawn at the 95th percentile value in each plot. Note the marked difference in magnitude between B and β, how this difference becomes more pronounced as the bubble moves toward the surface, and how the maximum of β stays a finite height above the surface even as the maximum of B approaches $z = 0$.

density distributions, and employ the closely related 'buoyancy pressure' (Appendix A.1) to gain intuition for our results.

3.2 Preliminaries

The Poisson equation for effective buoyancy

We begin by recalling the definition (2.1) of β as the Lagrangian vertical acceleration that would result from zeroing out the wind fields:

$$\beta \equiv \left.\frac{dw}{dt}\right|_{\mathbf{u}=0}.$$

In the previous chapter we used this to derive the Poisson equation (2.10) for β, originally due to DJ03:

$$-\nabla^2(\overline{\rho}\beta) = g\nabla_h^2\rho \ . \tag{3.2}$$

(Recall that $\nabla_h^2 \equiv \partial_x^2+\partial_y^2$; the difference between ∇_h^2 and ∇^2 is the source of all the interesting physics that follows.) Neglecting vertical variations in $\overline{\rho}$ (since the scale of such variations is larger than the density anomalies we will consider) and noting that $\nabla_h^2\rho = \nabla_h^2\rho'$, we obtain an even simpler form,

$$-\nabla^2\beta = -\nabla_h^2 B \ . \tag{3.3}$$

This is the Poisson equation for β that we will use in this chapter.

Effective buoyancy and the buoyancy pressure

Though Eqn. (3.3) is all we require to obtain analytical expressions for β, getting intuition for what these expressions tell us will require us to consider the *buoyancy pressure* p_β, also discussed in Appendix A.1. Analogous to the definition (2.1), p_β is defined as the non-hydrostatic pressure that would result from zeroing out the wind fields:

$$p_\beta \equiv p_{\rm nh}|_{\mathbf{u}=0} \ .$$

Taking the divergence of (2.6), invoking anelastic mass continuity, and setting $\mathbf{u} = 0$ yields the Poisson equation

$$-\nabla^2 p_\beta = \nabla_h^2 p_{\rm hyd} \ . \tag{3.4}$$

This equation just says that the divergence of $-\nabla p_\beta$ must cancel out any divergence produced by the horizontal hydrostatic pressure gradient $-\nabla_h p_{\rm hyd}$. That Eqn. (3.4) is reminiscent of Eqns. (2.10) and (3.3) is no accident; applying $-\partial_z$ to both sides of (3.4) yields $-\nabla^2(-\partial_z p_\beta) = g\nabla_h^2\rho$, and it follows from (2.6) that the boundary conditions of $-\partial_z p_\beta$ are identical to that of $\overline{\rho}\beta$, so we conclude that

$$\overline{\rho}\beta = -\partial_z p_\beta \ . \tag{3.5}$$

Thus, β is essentially the vertical component of the pressure gradient $-\nabla p_\beta$ which arises to compensate for hydrostatic pressure forces. Considering p_β will give us a picture of the full 3-D circulation resulting from parcel buoyancy, which will facilitate intuition for β.

Back-of-the-envelope estimate of effective buoyancy

We will be interested in solutions of (3.3) for parcels of characteristic height H and horizontal scale D. In terms of these parameters, we can roughly estimate $\partial_r^2 \sim 1/D^2$ (here and below, $r \equiv \sqrt{x^2+y^2}$ is our cylindrical radial coordinate) and $\partial_z^2 \sim 1/H^2$ and plug into (3.3) to obtain

$$\beta = \frac{B}{1+D^2/H^2}. \tag{3.6}$$

This suggests that $|\beta| < |B|$, as we expect, and that the proportionality factor depends quadratically on a parcel's aspect ratio D/H. The exact solutions of (3.3) for isolated cylindrical density anomalies, which we will present below, confirm this.

Before proceeding to that analysis, let us use (3.6) to re-do the usual linear perturbation analysis of a parcel in a stratified environment with potential temperature profile $\theta(z)$ and Brunt-Vaïsala frequency $N \equiv \sqrt{g\, d(\ln\theta)/dz}$. In the linear regime with no background flow there is no 'inertial' or 'dynamic' pressure stemming from the non-linear advection term in the momentum equation, and so $dw/dt = \beta$ (see previous chapter). Applying this to a small displacement δz, and using Eqn. (3.6), we then have

$$\frac{d^2\delta z}{dt^2} = -\frac{N^2}{1 + D^2/H^2}\delta z.$$

Letting $k \equiv 1/D$ and $m \equiv 1/H$, this implies that the parcel will oscillate with angular frequency

$$\omega = \frac{N}{\sqrt{1 + D^2/H^2}} = \frac{Nk}{\sqrt{k^2 + m^2}} \ ,$$

which is just the usual expression for the frequency of a gravity wave with horizontal and vertical wavenumbers k and m [see, for example, 30]. Thus, the reduction of the gravity-wave frequency from the Brunt-Vaïsala value can be seen as just the effect of effective buoyancy. That Eqn. (3.6) gives the exact right answer for ω is no accident, as (3.6) is itself exact for gravity waves, as can be checked by plugging in oscillating fields $B, \beta \sim \exp(i(kx + mz - \omega t))$ into Eqn. (3.3).

Despite the applicability of Eqn. (3.6) in the gravity-wave context, and the fact that it captures the reduction of β relative to B as a function of a parcel's aspect ratio, it is just a crude estimate and does not capture the dependence of β on a parcel's proximity to the surface seen in Fig. 3.1. To make further progress, we will need the exact solutions presented in the next two sections.

3.3 The free cylinder

We now refine the result (3.6) for the case of a 'free' parcel, i.e., a density anomaly in an infinite domain without boundary. The case of a parcel at the surface is treated in the next section. We proceed by partially solving the Poisson equation (3.3) for a uniform cylindrical density anomaly centered around the origin with Archimedean buoyancy B_0, diameter D, and height H. This is illustrated in Fig. 3.2a. The buoyancy field thus has the form

$$B = B_0\, \mathcal{H}(D/2 - r)\, \mathcal{H}(z + H/2)\, \mathcal{H}(H/2 - z) \tag{3.7}$$

where the Heaviside step functions $\mathcal{H}$ serve to restrict the density anomaly to our cylinder. Plugging this into (3.3) yields

$$-\nabla^2\beta = \frac{B_0}{r}\, \partial_r(r\delta(r - D/2))\, \mathcal{H}(z + H/2)\, \mathcal{H}(H/2 - z) \tag{3.8}$$

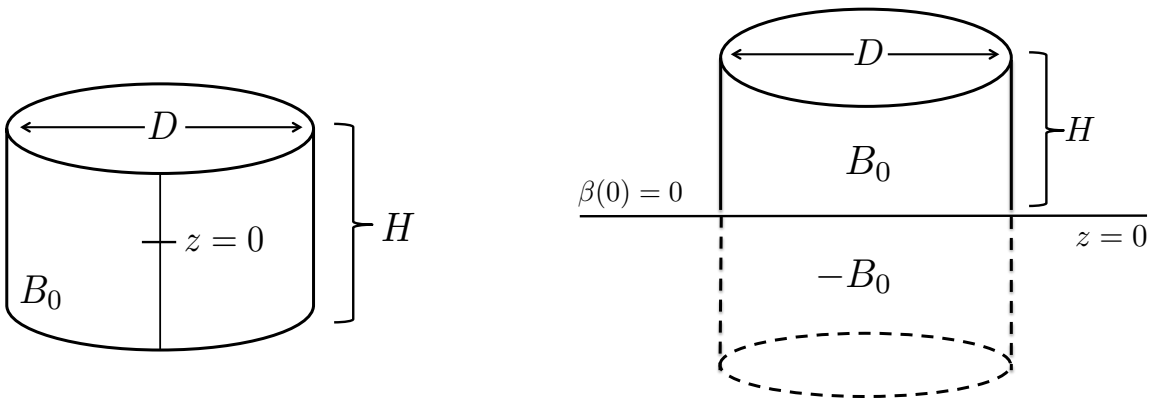

(a) Free Cylinder **(b)** Surface Cylinder

Figure 3.2: Illustrations of the buoyancy distributions appearing on the right-hand side of (3.3) for **(a)** the free cylinder and **(b)** the surface cylinder. The distribution is even about $z = 0$ for the free cylinder, but odd for the surface cylinder, enforcing a $\beta(0) = 0$ boundary condition for the latter.

where $\delta(r) = \partial_r \mathcal{H}(r)$ is the Dirac delta function.

A complete analytical solution of (3.8) would be arduous, if not impossible, but here we seek only the solution for β on the z-axis, which simplifies the problem considerably. Since the Green's function $G(\mathbf{x}; \mathbf{x}')$ for the Laplacian ∇^2 for a field with 'open' boundary conditions (i.e., a field which vanishes at infinity) is just $1/(4\pi|\mathbf{x} - \mathbf{x}'|)$, and since we are interested only in $\mathbf{x} = (0, 0, z)$, $\beta(z)$ on the z-axis is given by

$$\begin{aligned}\beta(z) &= \int d^3\mathbf{x}'\, G((0,0,z)\,;\mathbf{x}')\,\nabla_h^2 B(\mathbf{x}') \\ &= \frac{B_0}{2}\int_{-H/2}^{H/2} dz' \int_0^\infty dr' \frac{\partial_{r'}(r'\delta(r' - D/2))}{\sqrt{r'^2 + (z - z')^2}}\,.\end{aligned}$$

This double integral can be evaluated using integration by parts, the definition of the delta function, and trigonometric substitution. The result is

$$\beta(z) \;= \frac{B_0}{2}\left(\frac{1 - 2z/H}{\sqrt{D^2/H^2 + (1 - 2z/H)^2}} + \qquad \frac{1 + 2z/H}{\sqrt{D^2/H^2 + (1 + 2z/H)^2}}\right)\,. \tag{3.9}$$

This analytical expression is one of the main results of this paper.

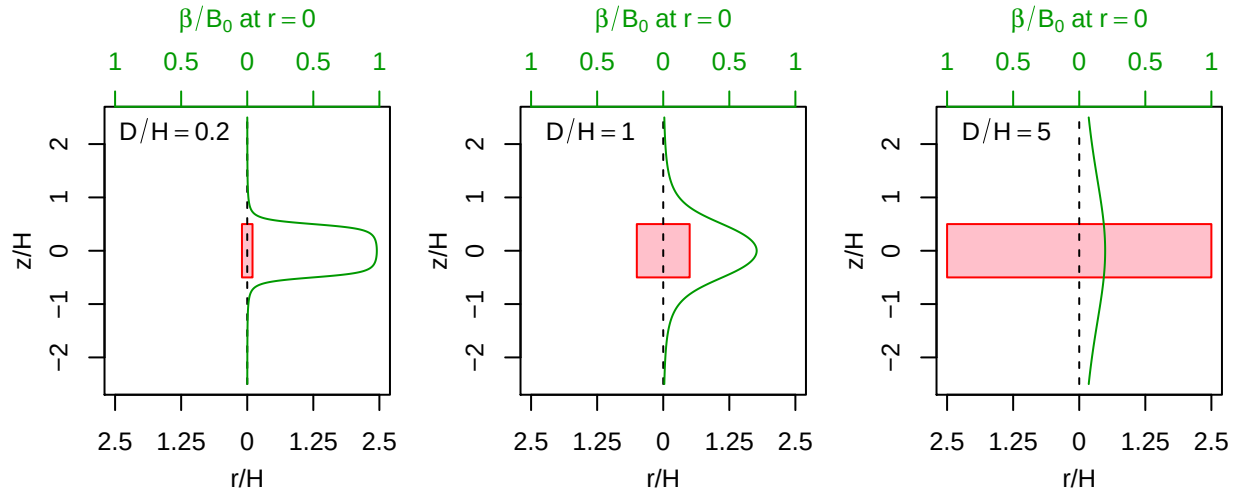

Figure 3.3: The curves $\beta(z)$ (in green) from Eqn. (3.9) for free cylinders of various aspect ratios D/H. The cylinders themselves are depicted to scale in pink. As D/H increases, there is a marked decrease in the maximum of $\beta(z)$, as well as an increase in the vertical scale over which β decays.

The function $\beta(z)$ is plotted as a function of z/H in Fig. 3.3 for various aspect ratios D/H, which are depicted to scale by pink boxes. Note that as D/H increases, the maximum of β decreases. This can be further illustrated by evaluating (3.9) at $z = 0$, which yields

$$\beta(0) = \frac{B_0}{\sqrt{1 + D^2/H^2}}. \tag{3.10}$$

This is plotted as a function of aspect ratio in Fig. 3.4, and quantifies the effect of aspect ratio on buoyant accelerations: for $D/H = 1$, the environmental response offsets the Archimedean buoyancy by 30%; for $D/H = 2$, 50%. For small aspect ratios $D/H \ll 1$ the plot of (3.10) in Fig. 3.4 flattens out, so narrow plumes do not become significantly more buoyant by splitting apart. In this regime we can also Taylor-expand the denominator in (3.10) to first order which yields

$$\beta(0) \approx \frac{B_0}{1 + D^2/(2H^2)} \quad \text{when } D/H \ll 1 \ ,$$

an expression very similar to (3.6). For the opposite, large aspect-ratio regime we have the alternate approximation

$$\beta(0) \approx B_0 \frac{H}{D} \quad \text{when } D/H \gg 1 \ . \tag{3.11}$$

We will contrast this expression with its analog for the surface cylinder in the next section.

These formulae quantify the decline of effective buoyancy with aspect ratio. What causes this decline, however? And why does it take the form (3.11) in the large-aspect ratio limit?

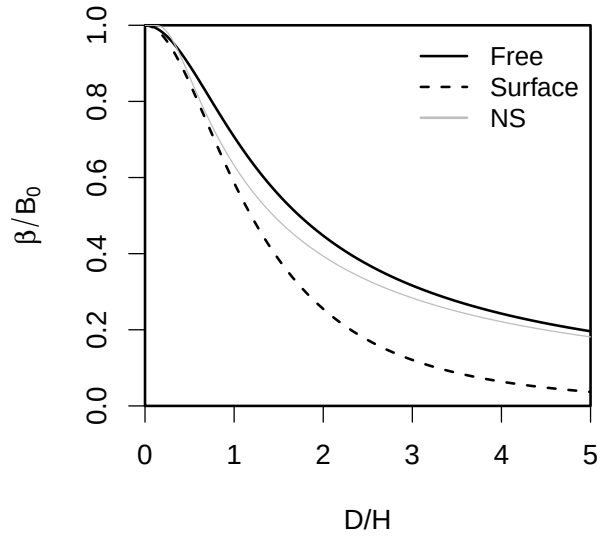

Figure 3.4: Effective buoyancies at the center of the free cylinder [Eqn. (3.10), solid line] and the surface cylinder [Eqn. (3.19), dashed line] as a function of D/H. Note that β is is always smaller for the surface cylinder than for the free one, and that it decreases much more rapidly as D/H increases. The thin gray line plots the result (3.25) of [56], which tracks our Eqn. (3.10) very closely.

To answer these questions we turn to the buoyancy pressure p_β introduced in Section 3.2. We must first find $p_\beta(z)$, which is easily obtained via (3.5) by integrating (3.9). Imposing the boundary condition $p_\beta \to 0$ as $z \to \infty$ yields

$$p_\beta(z) = \frac{\Delta p_{\rm hyd}}{2}\left(-\sqrt{D^2/H^2 + (1-2z/H)^2} + \sqrt{D^2/H^2 + (1+2z/H)^2} - 2\right) \qquad (3.12)$$

where

$$\Delta p_{\rm hyd} \equiv -\overline{\rho} B_0 H/2 \qquad (3.13)$$

is the $p_{\rm hyd}$ anomaly at the cylinder's center. Evaluating (3.12) at $z = 0$ yields

$$p_\beta(0) = -\Delta p_{\rm hyd}\ . \qquad (3.14)$$

This simple result is key for understanding the free cylinder, and does not hold for the surface cylinder. To gain intuition for it, consider a smooth, cylindrical buoyancy distribution (e.g., a Gaussian bubble as in Fig. 3.1), as depicted schematically in Figure 3.5a; the cylinder of uniform buoyancy given by (3.7) can be seen as a limit of such distributions. Figure 3.5a gives a heuristic derivation of (3.14), as follows.

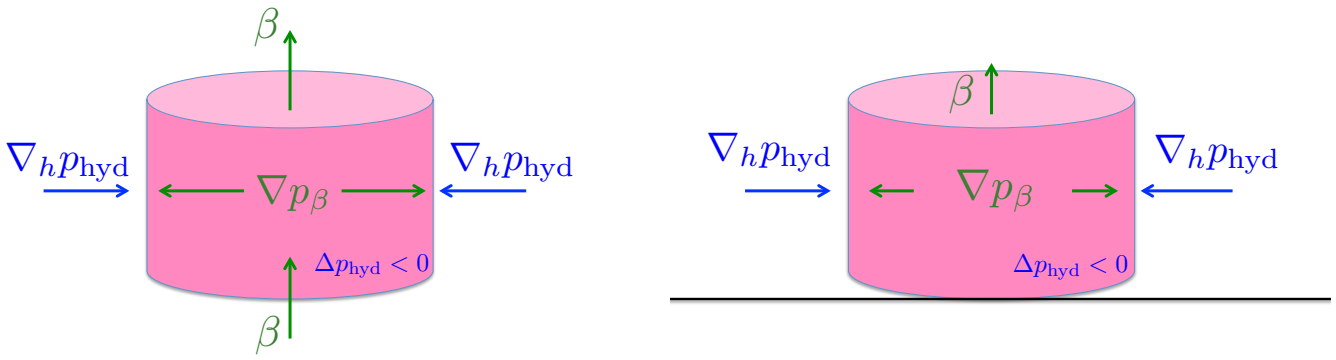

$$|\nabla_h p_\beta| = |\nabla_h p_{\rm hyd}|$$
$$p_\beta = -\Delta p_{\rm hyd}$$

(a) Free cylinder

$$|\nabla_h p_\beta| \neq |\nabla_h p_{\rm hyd}|$$
$$p_\beta < -\Delta p_{\rm hyd}$$

(b) Surface cylinder

Figure 3.5: Cartoon of the gradients $-\nabla_h p_{\rm hyd}$ and $-\nabla p_\beta$ and associated divergences for **(a)** the free cylinder and **(b)** the surface cylinder. Note that for the free cylinder, the vertical divergence from $-\nabla_z p_\beta = \overline{\rho}\beta$ is zero, so the horizontal convergence from $-\nabla_h p_{\rm hyd}$ must be balanced entirely by horizontal divergence from $-\nabla_h p_\beta$, which yields $p_\beta = -\Delta p_{\rm hyd}$. For the surface cylinder there is a vertical contribution to the divergence since $\beta(0) = 0$, and so a smaller value of $|-\nabla_h p_\beta|$ (and its divergence) is sufficient to balance the divergence from $-\nabla_h p_{\rm hyd}$, yielding $p_\beta < -\Delta p_{\rm hyd}$.

1. The hydrostatic pressure anomaly $\Delta p_{\rm hyd} < 0$ in the cylinder drives convergence into the cylinder via $-\nabla_h p_{\rm hyd}$ (blue arrows).

2. This must be balanced by divergence from $-\nabla p_\beta$, as per Eqn. (3.4). The $z \to -z$ symmetry of (3.3) implies that β at cylinder top and bottom must be equal, however, so the vertical component of $-\nabla p_\beta$ cannot contribute any divergence (vertical green arrows).

3. The horizontal divergence of $-\nabla p_\beta$ must then balance the convergence from $-\nabla_h p_{\rm hyd}$ (horizontal green arrows). Since this balance occurs over a common length scale D, we can infer Eqn. (3.14).

Now, a key feature of Eqn. (3.14) is that $p_\beta(0)$ is independent of horizontal scale. Why,

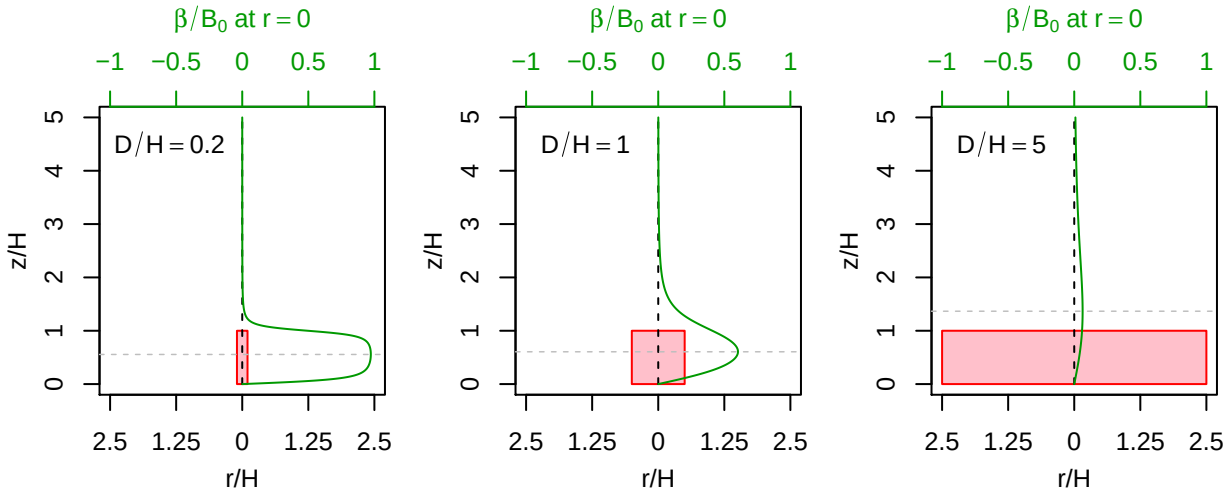

Figure 3.6: As in Fig. 3.3, but for surface cylinders with $\beta(z)$ given by (3.18). In addition to a decrease in β and increase in vertical scale as D/H increases, the location $z_{\max}$ (light gray dashed line) of $\beta_{\max}$ moves upward, with $z_{\max}$ located just above the cylinder for $D/H = 5$.

then, does β decline with increasing D/H for fixed H? As show in Appendix B.1, for large aspect ratios, the normalized field $p_\beta/p_\beta(0)$ is a fixed function of $\mathbf{x}/D$, with negligible H-dependence. In particular, this means that the height at which p_β decays to a given fraction of itself scales with D. Thus, $\beta = -(\partial_z p_\beta)/\overline{\rho}$ must scale as

$$\beta \sim \frac{p_\beta(0)}{\overline{\rho} D} . \tag{3.15}$$

If we combine this with Eqn. (3.14) and the definition (3.13) we get

$$\beta \sim -\frac{\Delta p_{\rm hyd}}{\overline{\rho} D} \sim B_0 \frac{H}{D}, \tag{3.16}$$

which is just the scaling we found in (3.11). Thus, the basic reason that aspect ratio matters for a free parcel is that *the vertical scale of p_β is a function of the parcel's horizontal scale D.* (This can also be inferred from Fig. 3.3.) If D increases while H (and hence $p_\beta(0) = -\Delta p_{\rm hyd}$) is fixed, a taller column of air must be moved with a fixed pressure differential, decreasing the gradient $\beta = (-\partial_z p_\beta)/\overline{\rho}$.

3.4 The surface cylinder

We now turn to parcels located at the lower boundary of a domain, where the vertical velocity w is identically 0 and hence so is β by (2.1). To solve (3.3) for a cylinder at

the surface (where the surface is at $z = 0$), we employ the method of images [DJ03; 25]. The idea of this technique is to enforce a $\beta(0) = 0$ boundary condition by solving the open boundary condition problem as in the previous section, but with an additional 'image cylinder' generated by reflecting the original surface cylinder across the $z = 0$ plane and switching the sign of its anomaly; see Fig. 3.2b. The source term $\nabla_h^2 B$ in (3.3) will then be odd with respect to z, which implies β will be odd too, ensuring $\beta(0) = 0$.

In this case, then, the Poisson equation for β is

$$-\nabla^2\beta = -\nabla_h^2 B_0\,\mathcal{H}(R-r)\,[\,\mathcal{H}(z)\mathcal{H}(H-z) - \mathcal{H}(-z)\mathcal{H}(H+z)\,]\ . \tag{3.17}$$

Integration against the Green's function as in the previous section yields the desired formula for β along the z-axis:

$$\beta(z) \;=\; \frac{B_0}{2}\left(\frac{1-z/H}{\sqrt{D^2/4H^2+(1-z/H)^2}} + \frac{2z/H}{\sqrt{D^2/4H^2+z^2/H^2}} \;-\; \frac{1+z/H}{\sqrt{D^2/4H^2+(1+z/H)^2}}\right). \tag{3.18}$$

This expression is the other main analytical result of this paper. This $\beta(z)$ is plotted as function of z/H for various D/H in Fig. 3.6. Similar to the free cylinder, the overall magnitude of β decreases with increasing D/H. To analyze this, we estimate the parcel's overall effective buoyancy by evaluating β at the center of the cylinder, yielding

$$\beta(H/2) = \frac{3B_0}{2}\left(\frac{1}{\sqrt{1+D^2/H^2}} \;-\; \frac{1}{\sqrt{9+D^2/H^2}}\right)\ . \tag{3.19}$$

We plot this function against D/H as the dashed line in Fig. 3.4. Note that *this curve is always less than that for the free cylinder*, consistent with Fig. 3.1, and declines much more rapidly with increasing D/H. In fact, the large aspect-ratio limit gives

$$\beta(0) \approx 6B_0\frac{H^3}{D^3} \quad \text{when } D/H \gg 1\ , \tag{3.20}$$

which should be compared with the H/D scaling in Eqn. (3.11).

Another noteworthy feature of Fig. 3.6 is that, like the free cylinder, the vertical scale over which β declines increases as D increases, but in this case the location $z_{\max}$ of the maximum of $\beta(z)$ (light grey dashed line in Fig. 3.6) also changes, and even appears outside the cylinder for $D/H = 5$. This may be surprising, but is consistent with the fact that, for $D \gg H$, $z_{\max}$ scales with D (Appendix B.1).

Why do surface parcels accelerate less than free ones? As in the previous section, we turn to p_β for insight. Again invoking (3.5), we integrate (3.18) with our $p_\beta \to 0$ as $z \to \infty$ boundary condition to obtain

$$p_\beta(z) = \frac{\Delta p_{\text{hyd}}}{2}\left(-\sqrt{D^2/4H^2 \;+\; (1-z/H)^2} + 2\sqrt{D^2/4H^2+z^2/H^2} \;-\; \sqrt{D^2/4H^2+(1+z/h)^2}\right). \tag{3.21}$$

Taking the $D/H \gg 1$ limit in (3.21) and evaluating at $z = 0$ then gives

$$p_\beta(0) \;\approx\; -\Delta p_{\rm hyd}\frac{H}{D} \;\ll\; -\Delta p_{\rm hyd}\;. \tag{3.22}$$

This stands in marked contrast to the free cylinder result (3.14), and is one of the main ways in which the surface cylinder differs from the free one. We again give a heuristic derivation for a smooth cylindrical density distribution, shown in Fig. 3.5b, as follows:

1. The hydrostatic pressure anomaly $\Delta p_{\rm hyd} < 0$ in the cylinder drives horizontal convergence into the cylinder via $-\nabla_h p_{\rm hyd}$ (blue arrows).

2. This must again be balanced by divergence from $-\nabla p_\beta$. For the surface cylinder, however, there is now a contribution from the vertical component of $-\nabla p_\beta$ (vertical green arrow). This is because the $\beta(0) = 0$ boundary condition at the surface breaks the reflection symmetry about the horizontal plane passing through the cylinder's center.

3. The horizontal component of $-\nabla p_\beta$ is thus no longer required to balance all of the convergence from $-\nabla_h p_{\rm hyd}$ (horizontal green arrows), and so can have a smaller magnitude $|-\nabla_h p_\beta| < |-\nabla_h p_{\rm hyd}|$. Since these gradients occur over a common length scale D we can infer $p_\beta(0) < -\Delta p_{\rm hyd}$, as expressed in (3.22).

We can now combine the foregoing with our earlier results to give a heuristic derivation of the scaling in (3.20). We have three scaling laws concerning the effective buoyancy of a surface parcel when $D \gg H$:

1. From Eqn. (3.15), we know that $\beta_{\rm max} \sim p_\beta(0)/(\overline{\rho}D)$.

2. From Eqn. (3.22), we know that the effect of a nonzero vertical divergence of $-\nabla p_\beta$, which arises from broken reflection symmetry, gives $p_\beta(0) \sim \Delta p_{\rm hyd} H/D$.

3. Assuming a linear increase of β with height from $z = 0$ to $z_{\rm max}$, the scaling $z_{\rm max} \sim D$ then gives $\beta(H/2) \;\sim\; \beta_{\rm max} H/D$.

Combining these three scaling laws then gives

$$\begin{aligned}
\beta\left(\frac{H}{2}\right) \;&\sim\; \beta_{\rm max}\frac{H}{D} && \text{by scaling law 3}\\
&\sim\; \frac{p_\beta(0)}{\overline{\rho}D}\frac{H}{D} && \text{by scaling law 1}\\
&\sim\; -\frac{\Delta p_{\rm hyd}}{\overline{\rho}D}\frac{H^2}{D^2} && \text{by scaling law 2}\\
&\sim\; B_0\frac{H^3}{D^3} && \text{by the definition (3.13) .}
\end{aligned}$$

Roughly speaking, each of our scaling laws yields a factor of H/D, combining to give a H^3/D^3 scaling just as in Eqn. (3.20).

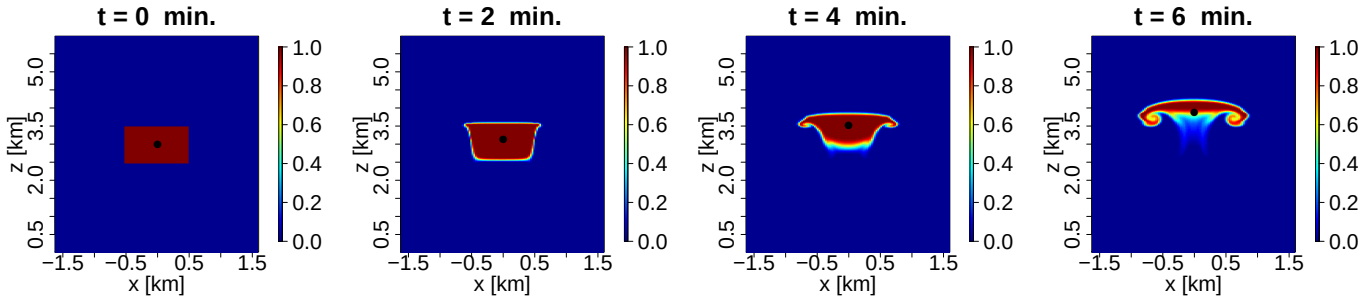

Figure 3.7: $x - z$ cross sections at $y = 0$ of q_{purity}, along with $z_{\text{cm}}(t)$ (black circle circles) for the $D = 1000$ m free cylinder. Only the middle 1/2 of the horizontal domain is shown.

3.5 LES tests

We now test the dependence of effective buoyancy on parcel aspect ratio and surface proximity by performing large-eddy simulations (LES) of the motion of our free and surface cylinders, again using DAM (cf. Section 2.3). We use a three-dimensional domain with doubly-periodic boundary conditions in the horizontal, and take a neutrally stratified, dry environment with a temperature of 300 K at the lower boundary, where w and β are zero. The neutral stratification and surface temperature, along with an assumption of hydrostatic balance, are sufficient to determine the environmental density profile $\overline{\rho}(z)$. For given cylinder parameters D (which we vary) and H (which we fix at 1000 m), the domain width and height must be taken large enough to sufficiently approximate the horizontally infinite and vertically (half) infinite boundary conditions of the free (surface) cylinders. Since the scale height of p_β scales with D when $D/H > 1$ (Appendix B.1), and since we must leave room for our cylinders to rise, we take the domain height $z_{\text{top}} = \max(2D, 6H)$ for free cylinders and $z_{\text{top}} = \max(D, 4H)$ for surface cylinders. We take the domain width to be $6.4D$. This is sufficient to ensure only small[2] differences between the idealized analytical and finite-domain numerical profiles of β/B_0.

Our density field is

$$\rho(\mathbf{x}) = \overline{\rho}(z) - \overline{\rho}(z_{\text{cm}})/300 \quad \text{for } r < D/2, \quad |z - z_{\text{cm}}| < H/2 \,,$$

with $\rho = \overline{\rho}(z)$ everywhere else. The center heights z_{cm} are $z_{\text{top}}/2$ for the free cylinder and $H/2$ for the surface cylinder. The grid spacings are $dx = dy = D/40$ and $dz = \min(dx, H/20)$. The adaptive time step is set to a maximum of $dz/(10\text{ m/s})$ to satisfy the CFL condition [17] for velocities up to at least ~ 10 m/s.

The cylinders are initialized with a purity tracer field q_{purity} that is set to 1 inside the cylinder and 0 outside and is advected passively by the flow. For each time t, we diagnose

[2]More specifically, the difference between the analytical and numerical profiles of β/B_0 never exceeds 0.04, with the relative error in in-parcel acceleration (the quantity we care about) never exceeding 5% at a given height for a given case.

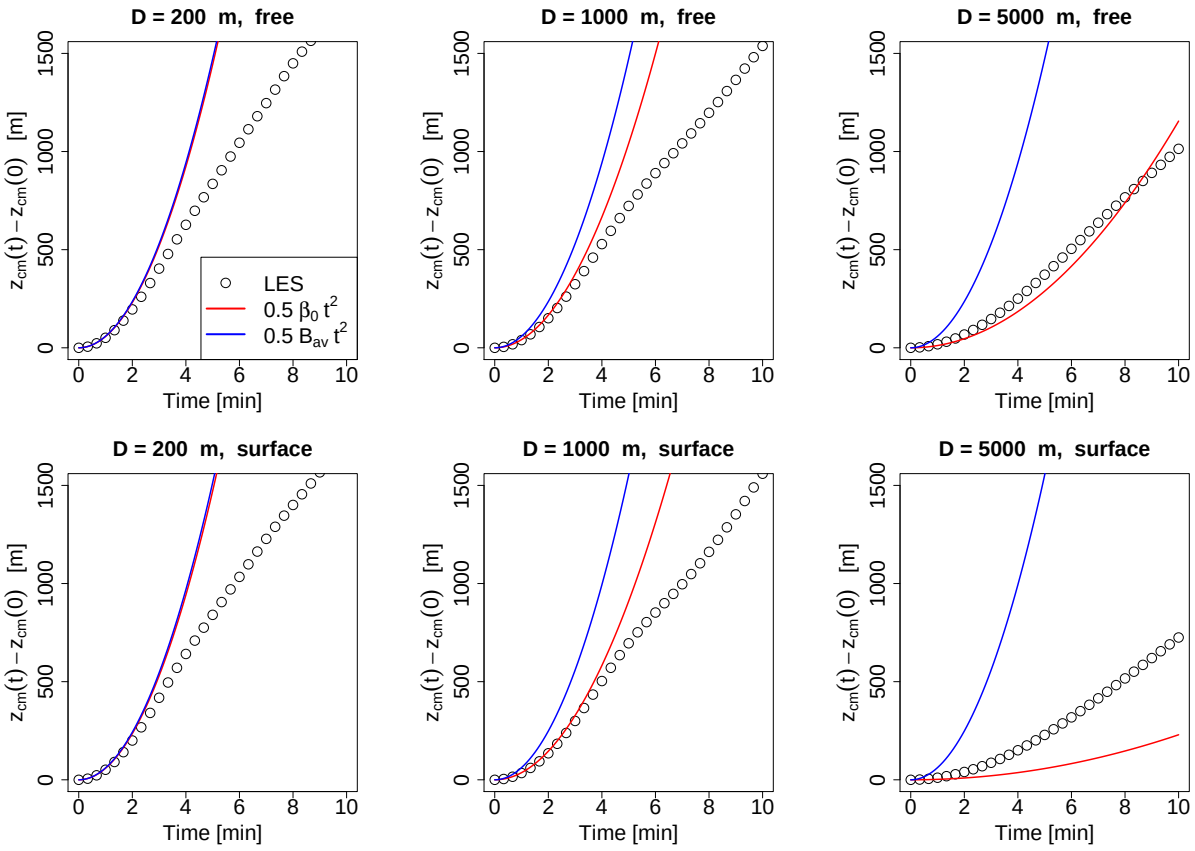

Figure 3.8: Diagnosed position of cylinder center-of-mass $z_{\rm cm}(t)$ (open black circles) for our cylindrical density anomalies with $H = 1000$ m and various D, as simulated by LES. The decreased acceleration with increasing aspect ratio is clear, especially when $D/H \gtrsim 1$ and for the surface cylinder in particular. The blue line shows the Archimedean buoyancy estimate $z_B(t)$ from Eqn. (3.23), which for the skinny cylinders agrees with the LES at early times, but cannot capture the initial acceleration of the wider cylinders. The red line shows the effective buoyancy estimate $z_\beta(t)$ from Eqn. (3.24), which fares better in capturing the parcel's initial acceleration for both free and surface cylinders, except for the $D/H = 5$ cylinders. See the text for further discussion.

the cylinder's center of mass z-coordinate as

$$z_{\rm cm}(t) \equiv \frac{\int\int\int d^3\mathbf{x}\, z\, q(\mathbf{x},t)\ \rho(\mathbf{x},t)}{\int\int\int d^3\mathbf{x}\, q(\mathbf{x},t)\ \rho(\mathbf{x},t)}$$

where the integrals are taken over the whole model domain. To get a sense of how these parcels evolve, the $q_{\rm purity}$ field, along with $z_{\rm cm}(t)$, is plotted at 3 minute intervals for the $D = 1000$ m free cylinder in Fig. 3.7.

Next, we plot the trajectories $z_{\rm cm}(t) - z_{\rm cm}(0)$ for free and surface cylinders in Fig. 3.8. We take $D = 200,\ 1000$, and 5000 m, so that $D/H = 1/5,\ 1$, and 5, just as in Figs. 3.3 and 3.6. Figure 3.8 shows that the $z_{\rm cm}(t)$ trajectories indeed exhibit the expected dependence of effective buoyancy on aspect ratio. The effect of the surface is not noticeable for $D/H = 1/5$ and 1, but is noticeable for $D/H = 5$; this is consistent with Fig. 3.4, and suggests that the effect of the surface becomes significant when $D/H \gtrsim 1$.

Figure 3.8 thus qualitatively confirms the physics presented in Sections 3.3 and 3.4. Can the formulae (3.10) and (3.19) derived in those sections be of any quantitative use? And how do they compare with the naive predictions of the Archimedean buoyancy? Let us take a first stab at this by focusing on the initial acceleration of our cylinders. The Archimedean estimate for this is simply the average initial Archimedean buoyancy $B_{\rm av}$ [B is not exactly constant throughout the cylinder, due to small variations in $\overline{\rho}(z)$], and so we plot the curve

$$z_B(t) \equiv 0.5 B_{\rm av} t^2 \tag{3.23}$$

in blue for each panel of Fig. 3.8. For the $D/H = 1/5$ cylinders, $z_B(t)$ matches $z_{\rm cm}(t)$ quite well for early times ($t < 2 - 3$ minutes), and thus the Archimedean buoyancy is a good approximation to the initial acceleration of these parcels. As aspect ratio increases, though, there is a growing discrepancy between the initial accelerations of $z_B(t)$ and $z_{\rm cm}(t)$ which is most pronounced for the surface cylinder. This is no surprise, though, as $B_{\rm av}$ is insensitive to aspect ratio and surface proximity; indeed, the curves $z_B(t)$ are virtually identical for all six cases.

Let us now turn to the effective buoyancy β. By its very definition (2.1) and the fact that our simulated atmosphere is initially motionless, we know that the average $\beta_{\rm av}$ of β over the cylinder must equal the initial acceleration of $z_{\rm cm}(t)$. The question, then, is to what degree the expressions (3.10) and (3.19), which strictly speaking only describe the center of the cylinder, approximate $\beta_{\rm av}$. To get a sense of this, we plot the trajectories

$$z_\beta(t) \equiv 0.5 \beta_0 t^2 \ , \tag{3.24}$$

where β_0 is just given by Eqns. (3.10) and (3.19) for the free and surface cases, respectively, against the diagnosed $z_{\rm cm}(t)$ in Fig. 3.8. For $D/H = 1/5$ the curves $z_B(t)$ and $z_\beta(t)$ are virtually identical, as one would expect, and both capture the initial acceleration of $z_{\rm cm}(t)$. For $D/H = 1$, $z_\beta(t)$ captures the diagnosed initial acceleration whereas $z_B(t)$ does not. For $D/H = 5$, $z_\beta(t)$ underestimates the initial acceleration quite significantly. This is because our uniform density anomalies with step function discontinuities feature a β that actually *increases* with r up to the cylinder's edge at $r = D/2$, since that is where the singular source for β is located in the Poisson equations (3.8) and (3.17). For $D/H \lesssim 1$, these radial variations in β are small and so Eqns. (3.10) and (3.19) are nonetheless good approximations to the average β, but for the $D/H > 1$ this is no longer true, and Eqns. (3.10) and (3.19) underestimates the cylinder's average β. This can also be seen in in the left column of Fig. 3.9, where the curves (3.10) and (3.19) are overlain on top of $\beta_{\rm av}/B_{\rm av}$ computed numerically for free and surface cylinders with $H = 1000$ m and various D. In the next section we will

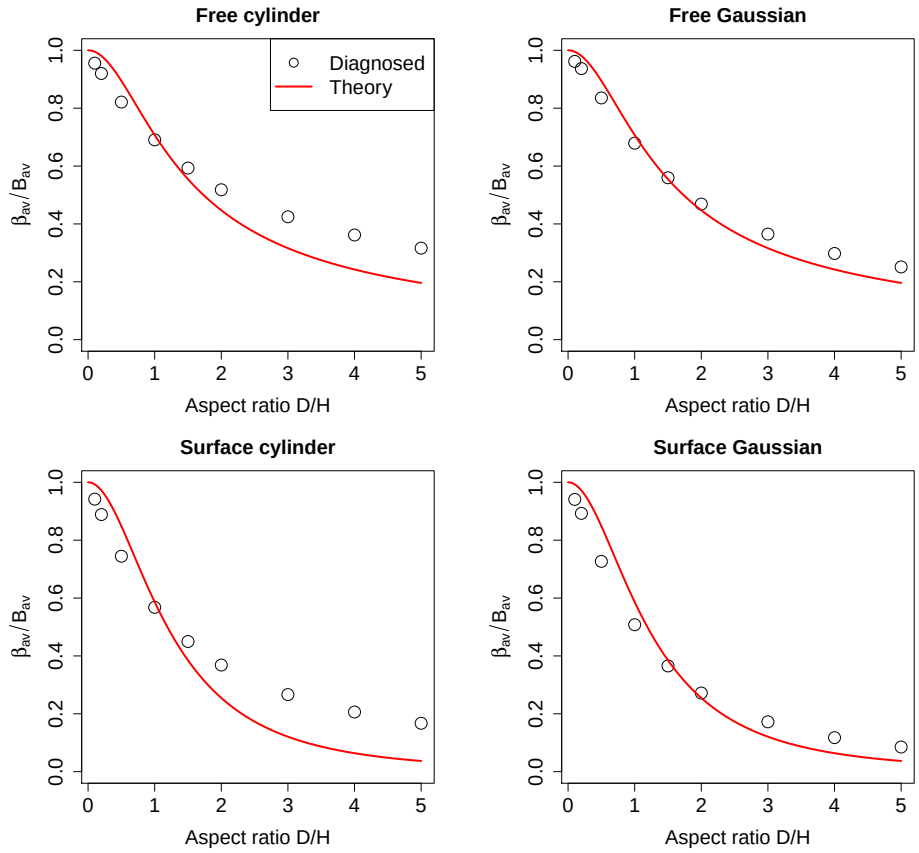

Figure 3.9: Comparison of the analytical expressions (3.10) and (3.19) with numerically diagnosed values of $\beta_{\rm av}/B_{\rm av}$ for our cylinders and for Gaussian bubbles of the form (3.1), with $H = 1000$ m and various D. Our formulae rather significantly underestimate $\beta_{\rm av}/B_{\rm av}$ for large aspect ratio cylinders, but give better agreement for large aspect ratio Gaussian bubbles.

come back to this figure, and discuss whether Eqns. (3.10) and (3.19) can be of quantitative use when $D/H > 1$.

As a final aside, we should comment on the over-prediction of $z_{\rm cm}(t)$ by $z_\beta(t)$ at later times ($t > 3$ minutes) for the $D/H \lesssim 1$ cases, where there is actually good initial agreement. Once a parcel begins to move, it experiences an internal circulation which may change its shape as well as entrain environmental air (Fig. 3.7), both of which will reduce its effective buoyancy. Furthermore, we expect drag forces to kick in and eventually balance any buoyant accelerations [64, 66], yielding a terminal velocity rather than continuing acceleration. Such a balance between buoyancy and drag at later times seems consistent with the diagnosed $z_{\rm cm}(t)$ in Fig. 3.8, and would also contribute to an overestimation of $z_{\rm cm}(t)$ by $z_\beta(t)$.

3.6 Summary and Discussion

We summarize our results as follows:

- The effective buoyancy of a fluid parcel depends on aspect ratio and surface proximity, as expressed in Eqns. (3.9) and (3.18) and depicted in Fig. 3.4.
- These effects can be understood in terms of the buoyancy pressure p_β, of which β is essentially just the vertical gradient.
- These effects indeed manifest in parcel motion as simulated by LES.

Many questions and potential applications remain, of course. An obvious first question is: what determines the aspect ratio of real convecting elements in the atmosphere? Our work here quantifies the well-known advantage that skinny parcels have over squat parcels in convecting. But a parcel that is too skinny will likely suffer too much dilution from entrainment to convect very far, and so the aspect ratio of real clouds is most likely determined by a balance between effective buoyancy and entrainment. Settling this question quantitatively, however, would require a more solid understanding of how entrainment varies with aspect ratio [68].

Another obvious follow-up question is: to what extent do Eqns. (3.10) and (3.19), which even for our highly idealized uniform cylinders only capture β_{av} for $D/H \lesssim 1$, apply to real convective clouds, which have highly heterogenous density distributions and irregular shapes? Interestingly, if we consider slightly less artifical density distributions such as Gaussian bubbles of the form (3.1) , then we no longer get a increase of β with r (Fig. 3.1), and Eqns. (3.10) and (3.19) give a better approximation of $\beta_{\text{av}}/B_{\text{av}}$, as shown in the right-hand column of Fig. 3.9. Thus, we may hold out some hope that our analytical expressions apply to more realistic convection. However, a comparison with density distributions derived from (say) cloud-resolving simulations would be necessary to confirm this.

We should note here that Eqn. (3.10) is not the only published candidate for β as a function of aspect ratio. Recently, [56] calculated β for a horizontally infinite slab of height H with sinusoidal density variations in x and y, and found that for such density distributions

$$\beta = B\left[1 - \exp\left(-H/D\right)\right] \tag{3.25}$$

where $D = 2/\sqrt{k^2 + l^2}$ is an effective diameter and k, l are the horizontal wavenumbers of the distribution. This curve is plotted in Fig. 3.4 in light gray, and matches quite closely the curve (3.10). Eqn. (3.25) can also be obtained by integrating a uniform buoyancy profile of height H and center-of-mass height $z_{\text{cm}} \to \infty$ against the Green's function in Eqn. (15) of [58]. That paper also touches upon the effect of the surface, and emphasizes the application of formulae such as their Eqns. (18) and (21) [analogous to our Eqns. (3.10) and (3.19)] to understanding the transition from hydrostatic to non-hydrostatic regimes in numerical modeling. In this regard, note that Eqn. (3.19) tells us that a grid-point

surface plume of height 1 km in a 'convection-permitting' model of horizontal resolution 4 km [the threshold identified in the recent review by [59]] should experience a roughly order-of-magnitude reduction in acceleration from the Archimedean value.

Finally, we note that the basic physics investigated here, namely the effect of environmental inertia on an accelerating parcel, is well known in the fluid dynamics literature as the 'virtual mass' or 'induced mass' effect [see, e.g., 2, 18]. This effect is usually incorporated into parameterizations of the vertical velocity equation, which often take the form [67]

$$\frac{dw}{dt} = aB - b\epsilon w^2 \,, \tag{3.26}$$

where a and b are dimensionless, a is often referred to as a 'virtual mass coefficient' [e.g., 8], and ϵ is an entrainment rate (units m^{-1}). The $-\epsilon w^2$ expression captures the effect of entrainment (mixing) drag, and b accounts for other types of drag such as form drag and wave drag, all of which are expected to be proportional to w^2. Before relating our results to such a parameterization, we should re-arrange (3.26) as it is unsatisfactory on two grounds. First, since b multiplies ϵ it introduces a spurious connection between (say) form drag and entrainment. Second, *any* force (not just buoyancy) will induce a back-reaction from the environment, and so the virtual mass coefficient a should multiply the drag term as well (assuming that the spatial distribution of buoyancy and drag forces is identical, so that we may use the same virtual mass coefficient). This suggests a drag term of the form $a[c_d A/(2V) + \epsilon]w^2$, where A is the projected area of the parcel, V is its volume, and c_d is a drag coefficient representing form and wave drag. Equation (3.26) can then be re-written as

$$\frac{1}{a}\frac{dw}{dt} = B - \left[\frac{c_d A}{2V} + \epsilon\right] w^2 \,, \tag{3.27}$$

which combined with the definition (2.1) yields

$$a = \beta/B \,.$$

Thus, our results (3.10) and (3.19) are just highly idealized calculations of the virtual mass coefficient a. Furthermore, they show that this coefficient depends on surface proximity.

Other analytical calculations of virtual mass coefficients exist in the fluid dynamics literature, but are often for foreign objects such as gas bubbles or solid spheres accelerating through a fluid [see, e.g., 2, 18]. Our case differs from that treated in textbooks in that the mass we are considering is part of the fluid, and so may accelerate non-uniformly and develop an internal circulation (as seen in Fig. 3.7). Mathematically, the difference is that we have no boundary condition on the environmental fluid velocity at the parcel's edge, as there would be for a solid body. It could, however, be of theoretical and perhaps practical interest to compare our expressions (3.10) and (3.19) to analogous expressions for solid bodies of similar geometries, such as the results of [9]. That there may be some connection is suggested by the special case of a sphere. To approximate this case we set $D = H$ in Eqn. (3.10), which yields an acceleration of $B_0/\sqrt{2} \approx 0.71 B_0$; this is quite close to the solid-body value of $2B_0/3$, typically derived by other means [18].

Chapter 4

On the sizes and lifetimes of cold pools

4.1 Introduction

The previous chapters studied the triggering of convection at cold pool edges, as well as the buoyant accelerations experienced by cold pools and other approximately cylindrical density anomalies. As mentioned in the introduction, however, there are basic questions about cold pool *thermo*dynamics for which we have little theoretical explanation. In particular, we have little sense of what determines the ultimate size and lifetime of cold pools, before they die by being warmed up to the ambient temperature.

To investigate this, we develop an "integral" or "box" model of a uniform, cylindrical cold pool. Such models have been used with some success to study gravity currents in a wide range of applications [34, 11, 33, 27, 69, 29]. Here, we develop the governing equations for a cold pool that is subject to entrainment, form drag, and surface fluxes of enthalpy and momentum. With these governing equations, we aim to develop a theory for the sizes and lifetimes of cold pools in the tropical atmosphere. As mentioned in the introduction, such a theory would be particularly relevant to global climate models, many of which have begun to include representations of cold pools in their convective parameterizations [60, 71, 23, 24, 62, 14].

4.2 Cylindrical cold pool

Consider a cylindrical cold pool that is characterized by a radius R, height H, uniform density anomaly ρ' (relative to the environmental air at the same height), and a radial velocity u^r that is independent of z and proportional to the radial coordinate r. Let us denote the volume of a cold pool by V, which is related to R and H by

$$V \;=\; \pi H R^2 \,. \tag{4.1}$$

We will denote the rate of change of the cold pool's radius as $U \equiv dR/dt$. Within the cold pool, the radial velocity u^r will be defined as

$$u^r = \frac{U}{R} r \,. \tag{4.2}$$

By continuity,

$$w = -\frac{2U}{R} z \,. \tag{4.3}$$

Therefore, the total kinetic energy of the cold pool is

$$\begin{aligned} \text{KE} &= \rho \int_0^R dr(2\pi r) \int_0^H dz \frac{1}{2} \left(u^{r\,2} + w^2 \right) \\ &= \rho V \left[\frac{1}{4} + \frac{2}{3} \left(\frac{H}{R} \right)^2 \right] U^2 \,. \end{aligned} \tag{4.4}$$

For $R \gg H$, the specific kinetic energy is simply $U^2/4$. The gravitational potential energy of the cold pool is simply

$$\text{PE} = \frac{g \rho' V H}{2} \,. \tag{4.5}$$

Changes in volume occur through entrainment. We write this as

$$\frac{d}{dt} V = \varepsilon U V \,, \tag{4.6}$$

where ε, which has units of m^{-1}, is the fractional entrainment per distance traveled by the cold pool's front. For example, if a cold pool has a volume of 1 km^3 and an entrainment rate of $\varepsilon = 10^{-4}$ m^{-1}, then it will entrain 10^5 m^3 as its radius increases by one meter. By entraining environmental air with zero density anomaly, entrainment tends to reduce the cold pool's density anomaly according to the following equation:

$$\left(\frac{d}{dt} \rho' \right)_{\text{entrainment}} = -\varepsilon U \rho' \,. \tag{4.7}$$

4.3 Sinks of energy

Our goal is to obtain a set of governing equations for the cold pool, including an equation for dU/dt. The gravity-current box models constructed by Huppert and Simpson [34], Ross, Tompkins, and Parker [69], and many others have neglected cold-pool dynamics entirely. Instead, those studies have assumed that the cold pool's front moves at a speed U that is proportional to $\sqrt{Hg\rho'/\rho}$; this is equivalent to assuming that the Froude number $U/\sqrt{Hg\rho'/\rho}$ is constant. This is a poor assumption because, in reality, the Froude number starts at zero (for an initially stationary cold pool), grows to positive values (as U grows),

goes to infinity (as ρ' goes to zero), and then becomes imaginary (for negative ρ'). In this study, all of the large-eddy simulations (LES) of cold pools with surface enthalpy fluxes exhibit this behavior regardless of whether H and ρ' are calculated for the entire cold pool or just its head. Clearly, the assumption of a constant Froude number is inadequate for modeling cold-pool dynamics.

We will find the governing equation for U by constructing the budget for the cold pool's total energy TE, which is the sum of its potential energy PE and its kinetic energy KE. If we can determine the sources and sinks of TE, then we can write down the energy equation, which will take the form

$$\frac{d}{dt}\mathrm{TE} \;\equiv\; \frac{d}{dt}(\mathrm{KE}+\mathrm{PE}) \;=\; \mathrm{sinks}\,. \tag{4.8}$$

Only one dU/dt will appear in this equation, and it is generated by d/dt acting on the U^2 in the definition of KE. By rearranging, this will give us our prognostic governing equation for U.

There are five sinks of total energy, which are caused by entrainment, surface drag, form drag, other pressure forces, and surface enthalpy fluxes. These five sinks are described in the following subsections.

Entrainment

Entrainment reduces kinetic energy by diluting the momentum. Consider a parcel with mass m and speed u. Its momentum is mu and its kinetic energy KE is $mu^2/2$. If the parcel entrains a mass dm with no momentum, then its mass goes to $m+dm$ by conservation of mass and its speed goes to $mu/(m+dm)$ by conservation of momentum. Therefore, KE goes to $(1-dm/m)$KE. By analogy, when the cold pool entrains a mass fraction $\varepsilon U dt$, we will assume that the cold pool's KE goes to $(1-\varepsilon U dt)$KE. Therefore, entrainment affects total energy by

$$\left(\frac{d}{dt}\mathrm{TE}\right)_{\mathrm{entrainment}} \;=\; -\varepsilon U \mathrm{KE}\,. \tag{4.9}$$

Note that entrainment will also "puff up" the cold pool, leading to a lifting of the center of mass of ρ' and, as a result, an increase in PE. We assume, however, that this increase in PE is obtained at the expense of KE so that this has no net effect on the total energy. (Note that turbulent entrainment can only occur if there is motion, i.e., positive KE, so this effect will never drive KE to negative values.)

Surface drag

Surface drag reduces kinetic energy by operating on the cold pool with a force opposite its motion. Using a bulk formula for the surface momentum flux, surface drag reduces total

energy according to

$$\left(\frac{d}{dt}\mathrm{TE}\right)_{\text{surface drag}} = -\int_A d^2x\, c_{ds}\rho u^{r3} = -\frac{2}{5}\pi c_{ds}\rho R^2 U^3\,, \tag{4.10}$$

where A is the area underneath the cold pool and $c_{ds} = 1.5 \times 10^{-3}$ is the surface drag coefficient.

Form drag

Form drag, caused by pressure forces between the cold pool and the environment, also reduces kinetic energy. Dissipation of energy from form drag is given by the integral of $c_{df}\rho U^3/2$ over the cold pool's outer boundary area $2\pi RH$, where c_{df} is the form drag coefficient. This gives

$$\left(\frac{d}{dt}\mathrm{TE}\right)_{\text{form drag}} = -\pi c_{df}\rho RHU^3\,. \tag{4.11}$$

The correct value for c_{df} is unknown. It will be treated as a tunable parameter and found by optimization.

Other pressure forces

Form drag is not the only force acting between the cold pool and its environment, as a cold pool will also experience the ''buoyancy perturbation pressure' discussed in Appendix A.1 which will cause the cold pool to accelerate less rapidly than would be estimated from buoyancy alone. The effect of this is precisely the reduction of Archimedean buoyancy to effective buoyancy, discussed at length in the previous chapter. From that chapter's Eqn. (3.19) we can estimate that for a cylindrical cold pool at the surface with $H = R$, the effective buoyancy is only about 1/4 that of the buoyancy. This does not mean, however, that only 1/4 of the cold pool's initial PE is converted to the cold pool's KE. Instead, the cold pool treats the overlying environment like a flywheel, pumping energy into it initially only to extract much of that energy as the cold pool is squashed by the descending environment. Rather than attempt to model this complicated dynamics in any detail, we will simply define α as the fraction of the cold pool's initial potential energy that is immediately or eventually converted to kinetic energy of the cold pool; $1-\alpha$ is the fraction that is permanently lost to the environment by pressure forces not attributable to form drag. Rather than write this as an explicit sink, we will simply introduce a factor of α in the definition of the cold pool's potential energy PE, modifying equation (4.5) to

$$\mathrm{PE} = \frac{\alpha g\rho' VH}{2}\,. \tag{4.12}$$

The correct value for α is unknown other than the fact that it must be between zero and one. Like c_{df}, its value will be found by optimization.

Surface enthalpy fluxes

Surface enthalpy fluxes reduce the density anomaly ρ' and, therefore, the potential energy. For the surface fluxes of density anomaly, we can write

$$\left(\frac{d}{dt}\rho'\right)_{\text{surface fluxes}} = \frac{1}{V}\int_A d^2x\, c_{ds}u^r(\rho'_s - \rho') = -\frac{2}{3}c_{ds}\left(1-\frac{\rho'_s}{\rho'}\right)\frac{U}{H}\rho', \tag{4.13}$$

where ρ'_s is the density of air that would be in equilibrium with the surface. Since PE is proportional to ρ', these surface enthalpy fluxes reduce TE according to

$$\left(\frac{d}{dt}\text{TE}\right)_{\text{surface fluxes}} = -\frac{2}{3}c_{ds}\left(1-\frac{\rho'_s}{\rho'}\right)\frac{U}{H}\text{PE}. \tag{4.14}$$

4.4 Governing equations

We can now specify the right-hand side of equation (4.8) as the sum of all of the sinks given by equations (4.9), (4.10), (4.11), and (4.14). This gives

$$\frac{d}{dt}\text{KE} + \frac{d}{dt}\text{PE} = -\varepsilon U\text{KE} - \frac{2}{5}\pi c_{ds}\rho R^2U^3 - \pi c_{df}\rho RHU^3 - \frac{2}{3}c_{ds}\left(1-\frac{\rho'_s}{\rho'}\right)\frac{U}{H}\text{PE}. \tag{4.15}$$

Next, we need to write $d\text{PE}/dt$ and $d\text{KE}/dt$ in terms of U and dU/dt. For $d\text{PE}/dt$, we first need to get an expression for the total time derivative of ρ', which we obtain by combining equations (4.7) and (4.13). This gives

$$\frac{d}{dt}\rho' = -\left[\varepsilon + \frac{2}{3}c_{ds}\left(1-\frac{\rho'_s}{\rho'}\right)\frac{1}{H}\right]U\rho'. \tag{4.16}$$

The equation for $d\text{PE}/dt$ then becomes

$$\begin{aligned}
\frac{d}{dt}\text{PE} &= \frac{d}{dt}\left(\frac{\alpha g\rho' VH}{2}\right)\\
&= \frac{d}{dt}\left(\frac{\alpha g\rho' V^2}{2\pi R^2}\right)\\
&= \left(\frac{2}{V}\frac{d}{dt}V - \frac{2}{R}\frac{d}{dt}R + \frac{1}{\rho'}\frac{d}{dt}\rho'\right)\text{PE}\\
&= \left[\varepsilon - \frac{2}{R} - \frac{2}{3}c_{ds}\left(1-\frac{\rho'_s}{\rho'}\right)\frac{1}{H}\right]U\text{PE}.
\end{aligned} \tag{4.17}$$

For $d\text{KE}/dt$, we can proceed in a similar way after taking the derivative of equation (4.4). This gives

$$\frac{d}{dt}\text{KE} = \rho U^3\left[\frac{1}{4}\varepsilon V + 2\pi H^3(\varepsilon - 2/R)\right] + \rho U\left(\frac{1}{2}V + \frac{4\pi}{3}H^3\right)\frac{d}{dt}U. \tag{4.18}$$

Substituting the expression for $d\mathrm{PE}/dt$ and $d\mathrm{KE}/dt$ from equations (4.17) and (4.18) into the left-hand side of (4.15), we get

$$\frac{d}{dt}U = \left[\frac{V}{2}+\frac{4\pi H^3}{3}\right]^{-1}\left\{-\left[\frac{1}{4}\varepsilon V+2\pi H^3\left(\varepsilon-2/R\right)\right]U^2+\left(2/R-\varepsilon\right)\frac{\alpha g\rho' VH}{2\rho}\right.$$
$$\left.-\varepsilon\left[\frac{1}{4}V+\frac{2\pi}{3}H^3\right]U^2-\frac{2}{5}\pi c_{ds}R^2U^2-\pi c_{df}RHU^2\right\}, \quad (4.19)$$

The other governing equations are:

$$\frac{d}{dt}R = U\,, \quad (4.20)$$
$$\frac{d}{dt}V = \varepsilon UV\,, \quad (4.21)$$
$$\frac{d}{dt}\rho' = -\left(\varepsilon+\frac{2}{3}c_{ds}(1-\rho'_s/\rho')\frac{1}{H}\right)U\rho'\,, \quad (4.22)$$
$$H = V/(\pi R^2)\,. \quad (4.23)$$

4.5 Simplified governing equations

Although equations (4.19–4.23) form a complete set of governing equations for the uniform, cylindrical cold pool, they are too complicated to provide much insight. Fortunately, many of the terms can be dropped because they are negligible in magnitude. To find out which terms can be dropped, we first need to find the minimum height of the cold pool.

Note that (4.21) and (4.23) can be combined to give

$$\frac{d}{dR}H = (\varepsilon-2/R)H\,, \quad (4.24)$$

which, assuming a constant ε, integrates to

$$H = H_0\left(\frac{R_0}{R}\right)^2\exp\left[\varepsilon(R-R_0)\right], \quad (4.25)$$

where R_0 and H_0 are the initial radius and height, respectively. The minimum value of H occurs where $dH/dR=0$, which, according to (4.24), is when $R=2/\varepsilon$. As we will see in section 4.9, a typical value for the fractional entrainment rate is $\varepsilon = 0.2$ km^{-1}. Therefore, the minimum H occurs around $R=10$ km. Assuming $R_0=H_0=1$ km, equation (4.25) gives a minimum H of 60 m.

Now, let us turn our attention to the governing equation for ρ', which can be written as

$$\frac{d}{dR}\rho' = -\left(\varepsilon+\frac{2c_{ds}}{3H}+\frac{2c_{ds}}{3H}\frac{|\rho'_s|}{\rho'}\right)\rho'\,, \quad (4.26)$$

where we have assumed that $\rho'_s < 0$, meaning that the virtual potential temperature flux off the surface is positive. Assuming that $\varepsilon = 0.2$ km^{-1} and $c_{ds} = 1.5 \times 10^{-3}$, the $2c_{ds}/3H$ is equal to or larger than ε only if $H < 5$ m. As we just learned, however, H never gets smaller than about 60 m, which is an order of magnitude larger than this threshold. Therefore, the second term in parentheses can be dropped. Note that we cannot drop the last term because ρ' can become very small compared to $|\rho'_s|$. After dropping the $2c_{ds}/3H$ term, we can then use (4.25) to replace H in (4.26), and then we can integrate, yielding

$$\rho' \;=\; e^{-\varepsilon(R-R_0)} \left[\rho'_0 + \frac{2}{9} c_{ds} \rho'_s \frac{1}{R_0^2 H_0} (R^3 - R_0^3) \right] . \tag{4.27}$$

Note that this is an analytical expression for ρ' as a function of R.

Next, we need to simplify equation (4.19), which is the governing equation for U. First, we will set the form drag coefficient c_{df} to zero; this will be justified in section 4.9. Second, we will discard all of the H^3 terms. The H^3 terms all stem from the contribution of vertical momentum to the cold pool's kinetic energy. Intuitively, we know that the contribution of vertical momentum to the kinetic energy of a cylindrical cold pool is only relevant in the initial stages as it begins to fall, as some of the potential energy gets briefly routed through vertical kinetic energy on its way to becoming horizontal kinetic energy. Indeed, all of the H^3 terms in (4.19) are added to V terms, and $H^3/V \propto H/R$, which decreases rapidly in the initial stages of a cold pool. So, we throw away all of the H^3 terms; this is tantamount to writing

$$\mathrm{KE} \;=\; \rho V \frac{1}{4} U^2 \tag{4.28}$$

rather than the full expression in equation (4.4). Of course, throwing away the H^3 terms adds some error to the initial development of our theoretical cold pool. If we were interested in studying the initial stages of cold pools – say, for R in the range of R_0 to $2R_0$ – then this could be a problem. But, our focus here is on the lifetimes and eventual sizes of cold pools, not the initial stages of cold pools, so this approach will suit us fine. In addition, this approximation overestimates the kinetic energy only for $R_0 \le R \lesssim 2R_0$, which occupies an exceedingly small fraction of the cold pool's lifetime and maximum area: only ∼6 minutes of a lifetime that is measured in hours, and only ∼1% of the cold pool's eventual area.

At this point, the governing equation for U has been simplified to

$$\frac{d}{dt} U \;=\; \underbrace{-\varepsilon U^2}_{\substack{\text{entrainment} \\ \text{drag}}} \; \underbrace{+ \left(\frac{2}{R} - \varepsilon \right) \frac{\alpha g \rho' H}{\rho}}_{\text{descent and puffing}} \; \underbrace{- \frac{4 c_{ds}}{5H} U^2}_{\text{surface drag}} . \tag{4.29}$$

On the right-hand side, there are three sources and sinks of U, which are due to entrainment drag, exchange of energy between PE and KE, and surface drag. As discussed above, H never becomes small enough for c_{ds}/H to approach the magnitude of ε, so we may discard the third term on the right-hand side. The middle term, however, requires more thought. The piece proportional to $2/R$ is the force that accelerates the cold pool by converting gravitational

potential energy to kinetic energy: cold-pool spreading leads to descent that lowers its center of mass. The piece proportional to ε is a force that decelerates the cold pool by converting kinetic energy to potential energy: cold-pool entrainment causes the cold pool to puff up and raise its center of mass. For $R < 2/\varepsilon$, the center of mass descends with time, accelerating the cold pool. For $R > 2/\varepsilon$, the center of mass ascends with time, decelerating the cold pool. This is something of a strange notion: for $R > 2\varepsilon$, expansion of the cold pool saps it of kinetic energy. As we will see in section 4.9, the LES cold pools have an entrainment rate that tends to decrease at large R in a way that keeps ε equal to or less than $2/R$, so this behavior is largely avoided.

Qualitatively, the middle term on the right-hand side of (4.29) has its biggest moment at the very beginning of the cold pool's life. In the short time that it takes for the cold pool to increase its radius from R_0 to $2R_0$, about 75% of the initial potential energy is expended. For a cold pool with $R_0 = H_0 = 1$ km and a 1-K temperature anomaly, this only takes about 6 minutes. Therefore, rather than try to model the detailed interactions between PE and KE, we will simply put all of the initial PE into KE at the very start. This allows us to drop the middle term on the right-hand side of (4.29). By equations (4.12) and (4.28), we must give the cold pool an initial U equal to

$$U_0 \;=\; \sqrt{\frac{2\alpha g \rho_0' H_0}{\rho}}\,. \tag{4.30}$$

With the understanding that U is to be set to U_0 as given by equation (4.30) at time $t = 0$, we now have

$$d\log(U) \;=\; -\varepsilon dR\,.$$

Integrating, again assuming a constant ε, we get

$$U \;=\; U_0 \exp\Big[-\varepsilon(R - R_0)\Big]\,, \tag{4.31}$$

which is an analytical expression for U as a function of R. Note that this describes a very simple process: the reduction of kinetic energy by entrainment.

Since this is a very simple equation, it can be written in many convenient forms. For example, we can solve for time t as a function of cold-pool radius R,

$$t \;=\; \frac{1}{\varepsilon U_0}\Big(\exp\Big[\varepsilon(R - R_0)\Big] - 1\Big)\,. \tag{4.32}$$

We can also write down an expression for $R(t)$,

$$R \;=\; R_0 + \frac{1}{\varepsilon}\log(1 + t\varepsilon U_0)\,, \tag{4.33}$$

and an expression for $U(t)$,

$$U \;=\; \frac{U_0}{1 + t\varepsilon U_0}\,. \tag{4.34}$$

Although there are many such equations that can be written down, the simplified theory for a cylindrical cold pool can be completely and succinctly described by the following three equations:

$$R(t) = R_0 + \frac{1}{\varepsilon}\log(1 + t\varepsilon U_0) \tag{4.35}$$

$$H(R) = H_0 \left(\frac{R_0}{R}\right)^2 \exp\Big[\varepsilon(R - R_0)\Big] \tag{4.36}$$

$$\rho'(R) = e^{-\varepsilon(R-R_0)} \left(\rho'_0 + \frac{2}{9} c_{ds} \rho'_s \frac{1}{R_0^2 H_0}(R^3 - R_0^3)\right) . \tag{4.37}$$

4.6 Radius and time of death

These equations can be used to predict the demise of cold pools. Let us define the termination – or, more colloquially, the death – of a cold pool as the time when it ceases to be cold. Or, to acknowledge the virtual-temperature effect of water vapor, we can be more precise by defining the termination of a cold pool as the time when $\rho' = 0$. Note that we will be using the equations derived in the previous section, which apply to an isolated cold pool over a flat surface with no mean wind; a mean wind, topography, or collisions with other cold pools could all hasten a cold pool's demise. Throughout the paper, we will denote the terminal time and terminal radius as $t_{\rho'=0}$ and $R_{\rho'=0}$, respectively.

We can solve for the terminal radius by setting $\rho' = 0$ in (4.37). This gives

$$R_{\rho'=0} = R_0 \left(1 + \frac{9}{2c_{ds}} \frac{H_0}{R_0} \frac{\rho'_0}{|\rho'_s|}\right)^{1/3} , \tag{4.38}$$

which, surprisingly, has no dependence on the entrainment rate. Note that, for $c_{ds} = 1.5 \times 10^{-3}$, $9/2c_{ds}$ equals 3000. Therefore, so long as $R_0|\rho'_s|$ is not three orders of magnitude larger than $H_0\rho'_0$, then the terminal R is very well approximated by the second term in parentheses. In fact, inspection of cold-pool transects from the simulations performed for Chapter 2 reveals that $H_0/R_0 \sim 1$ and $\rho'_0/|\rho'_s| \sim 1$. Therefore, we can safely simplify this expression to

$$R_{\rho'=0} = R_0 \left(\frac{9}{2c_{ds}} \frac{H_0}{R_0} \frac{\rho'_0}{|\rho'_s|}\right)^{1/3} . \tag{4.39}$$

Due to the 1/3 exponent, the dependence of $R_{\rho'=0}$ on H_0/R_0 and $\rho'_0/|\rho'_s|$ is weak. If we take $H_0/R_0 \approx 1$ and $\rho'_0/|\rho'_s| \approx 1$, then

$$R_{\rho'=0} \approx R_0 \left(\frac{9}{2c_{ds}}\right)^{1/3} = 14R_0 . \tag{4.40}$$

Therefore, from pure physical reasoning, we can conclude that the terminal radius of a cold pool is about 14 times its initial radius. Figure 4.1 shows the dependence of $R_{\rho'=0}/R_0$ as

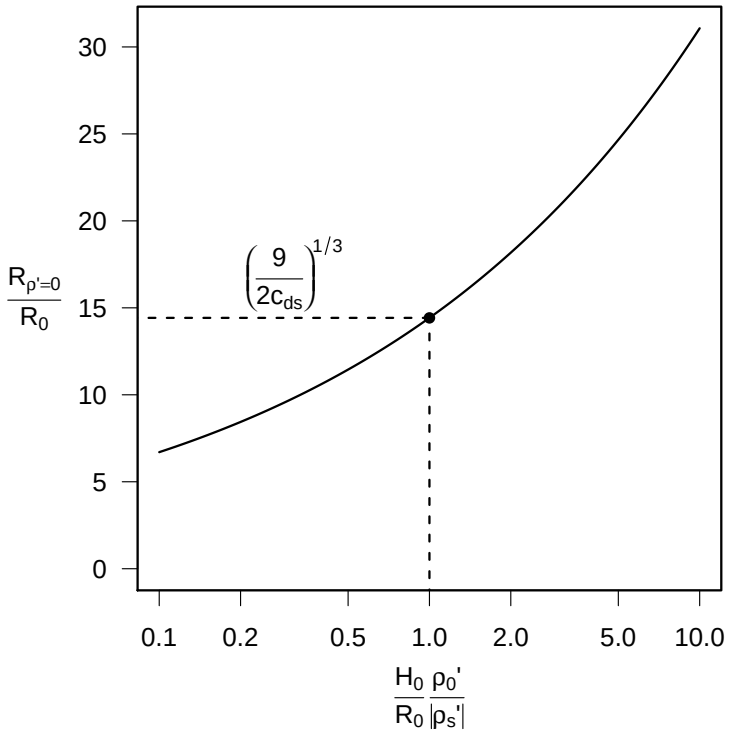

Figure 4.1: The terminal radius $R_{\rho'=0}$ from equation (4.38) plotted as a function of $H_0\rho_0'/R_0|\rho_s'|$. Thanks to the 1/3 exponent in equation (4.38), $R_{\rho'=0}$ ranges only over a factor of 4 as $H_0\rho_0'/R_0|\rho_s'|$ varies over a factor of 100. The dashed lines denote the values of $H_0\rho_0'/R_0|\rho_s'| = 1$ and $R_{\rho'=0}/R_0 = 14$ from equation (4.40).

a function of $H_0\rho_0'/R_0|\rho_s'|$. Thanks to the 1/3 exponent in equation (4.38), the terminal radius varies over a small range (7 to 31 km) even as $H_0\rho_0'/R_0|\rho_s'|$ is varied over two orders of magnitude (from 0.1 to 10).

Using $R = R_{\rho'=0}$ in (4.32) gives the time when the cold pool ceases to be cold,

$$t_{\rho'=0} \;=\; \frac{1}{\varepsilon U_0}\left(\exp\left[\varepsilon(R_{\rho'=0} - R_0)\right] - 1\right) . \tag{4.41}$$

While the terminal radius of a cold pool is constrained to lie within roughly a factor of two of $14R_0$, the terminal time can vary over a much larger range. This occurs because, in the expression for $t_{\rho'=0}$, there is both a factor of $1/U_0$ and an exponential of $R_{\rho'=0}$. Note that the terminal radius does not depend on U_0 because the two processes that reduce ρ' – entrainment and surface fluxes – operate on a per-distance fashion. Therefore, a halving of U_0 leaves the terminal radius unchanged, but it doubles the terminal time. The sensitivity of $t_{\rho'=0}$ is illustrated in Figure 4.2, which shows $R_{\rho'=0}$ and $t_{\rho'=0}$ as heat maps plotted on axes of

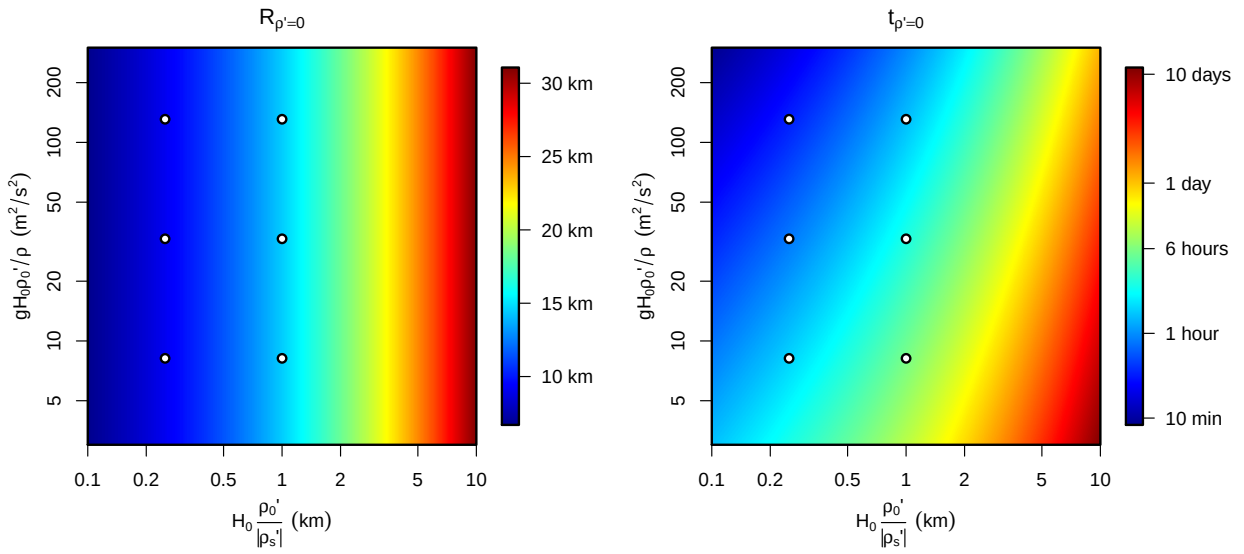

Figure 4.2: (left) The terminal radius $R_{\rho'=0}$ given by equation (4.38) plotted as a function of $H_0\rho_0'/R_0|\rho_s'|$ and $gH_0\rho_0'/\rho$ for $R_0 = 1$ km and $\varepsilon = 0.2$ km^{-1}. Note that $R_{\rho'=0}$ depends only on $H_0\rho_0'/R_0|\rho_s'|$ and varies only over a factor of 4 for a 100-factor range in $H_0\rho_0'/R_0|\rho_s'|$. (right) Same, but for the terminal time $t_{\rho'=0}$ obtained from equation (4.41). Unlike the terminal radius, the terminal time depends on both expressions and it ranges here over three orders of magnitude. The circles denote the locations in parameter space of the large-eddy simulations presented in section 4.8.

$H_0\rho_0'/R_0|\rho_s'|$ and $gH_0\rho_0'/\rho$, assuming $R_0 = 1$ km and $\varepsilon = 0.2$ km^{-1}. Both axes are chosen to range over two orders of magnitude, centered on the values obtained using $R_0 = H_0 = 1$ km and $\rho_0' = |\rho_s'| = 1$ K. As in Figure 4.1, $R_{\rho'=0}$ varies by only a factor of four from its lowest value to its highest value (i.e., within a factor of two of 14 km). In contrast, $t_{\rho'=0}$ varies over a range covering more than three orders of magnitude, from about 10 minutes to 10 days.

Since equation (4.38) has no dependence on ε, it is tempting to think that entrainment plays no role in setting the terminal radius. To the contrary, entrainment plays a very important role in setting $R_{\rho'=0}$. In the derivation of equation (4.26) for ρ', entrainment allowed us to neglect the piece of the surface flux that scales as ρ' (this was the argument about H having a finite lower bound). Why were we able to neglect this term? After all, the surface enthalpy flux is proportional to $\rho' - \rho_s'$, so it might seem odd that we could neglect the ρ' part of this. The reason, though, is simple. Entrainment quickly reduces ρ' towards zero, and it does so without changing the total mass anomaly $V\rho'$. As a result, entrainment "hides" the coldness of the cold pool from the surface without changing the total amount of enthalpy needed from the surface to terminate the cold pool, which is proportional to the mass anomaly $V\rho'$. So, entrainment plays a vital role in generating equation (4.38) even

though it does not show up explicitly there.

In fact, we can see this mechanism at work in equation (4.39). Noting that the initial cold-pool volume V_0 is equal to $\pi R_0^2 H_0$, we can write (4.39) as

$$R_{\rho'=0} \;=\; \left(\frac{9 V_0 \rho_0'}{2\pi c_{ds} |\rho_s'|} \right)^{1/3} . \tag{4.42}$$

In the numerator, $V_0 \rho_0'$ is the cold pool's initial mass anomaly, which can only be reduced by surface fluxes. Since entrainment quickly hides the coldness of the cold pool (i.e., $\rho' \to 0$), $|\rho_s'|$ is the density difference between the cold pool and the air in direct contact with the surface. Therefore, the $c_d |\rho_s'|$ in the denominator is proportional to the surface enthalpy flux. The cube root is explained by the fact that the integrated surface flux is proportional to the product of the cold-pool surface area (order R^2) and the total translation of the cold pool over the surface (order R).

To quantify the effect of entrainment on $R_{\rho'=0}$, we can recalculate the expression for $R_{\rho'=0}$ assuming zero entrainment. To do this, we need to start over from equation (4.26), set $\varepsilon = 0$, and retain the $c_{ds}\rho'$ term. The resulting expression is

$$R_{\rho'=0} \;=\; R_0 \left[1 + \frac{9}{2 c_d} \frac{H_0}{R_0} \log \left(1 + \frac{\rho_0'}{|\rho_s'|} \right) \right]^{1/3} \qquad (\text{for } \varepsilon = 0) \,. \tag{4.43}$$

This is practically the same as equation (13) in Ross, Tompkins, and Parker [69], who derived a box model for cold pools by ignoring entrainment entirely. The one difference is the factor of 9/2 here, which is 3 in Ross, Tompkins, and Parker [69] stemming from the mistake of using $u^r = U$ rather than $u^r = Ur/R$. For small $\rho_0'/|\rho_s'|$, equation (4.43) simplifies to equation (4.38). For large $\rho_0'/|\rho_s'|$, however, equations (4.43) and (4.38) differ substantially. If a cold pool with $R_0 = H_0 = 1$ km is 2 K colder than its surroundings, and if the ambient air-sea temperature difference is 0.2 K, then $\rho_0'/|\rho_s'|$ equals 10. In this case, equation (4.38) predicts $R_{\rho'=0} = 31$ km while equation (4.43) predicts $R_{\rho'=0} = 19$ km. By hiding the cold pool's total thermal deficit (equivalently, its $\rho' V$), entrainment reduces surface fluxes and increases the terminal sizes of cold pools.

Before concluding this section, let us consider whether the initial condition assumed here – a static cylinder of cold air – is appropriate and generalizable to more realistic conditions. In a real rain event, there is a finite time during which cold air is generated and fed into the cold pool. Given a typical updraft speed of 10 m s^{-1} and an atmospheric scale height of 10 km, we might expect the duration of precipitation shafts to be about 10 km/10 m s^{-1} $\approx$ 20 minutes. Indeed, this is the typical lifetime of precipitation shafts in the large-eddy simulations (LES) of radiative-convective equilibrium (RCE) performed in Chapter 2. Since 20 minutes is short compared to the lifetimes of cold pools predicted here, the use of instantaneously generated cold pools is appropriate.

To apply equations (4.41) and (4.42) to cold pools that are measured in observations or LES, we must generalize the definitions of R_0, V_0, ρ_0', and U_0 to those cases. For R_0, this is straightforward: we can define R_0 as the halfwidth of the precipitation shaft or, for

non-circular rain footprints, we can define R_0 as the square root of the footprint divided by π. For V_0, U_0, and ρ_0', we can calculate these variables based on the air that flows laterally out of the rain shaft. For notational simplicity, imagine that the rain shaft has a circular footprint of radius R_0. Then, the total initial cold-pool mass ($\rho_0 V_0$), mass anomaly ($\rho_0' V_0$), and kinetic energy ($\rho_0 V_0 U_0^2/4$) are given by

$$\rho_0 V_0 = R_0 \int_0^T dt \int_0^{2\pi} d\phi \int_0^{z_{\rm BL}} dz\, u^r \mathcal{H}(u^r) \rho \tag{4.44}$$

$$\rho_0' V_0 = R_0 \int_0^T dt \int_0^{2\pi} d\phi \int_0^{z_{\rm BL}} dz\, u^r \mathcal{H}(u^r) \rho' \tag{4.45}$$

$$\rho_0 V_0 \frac{1}{4} U_0^2 = R_0 \int_0^T dt \int_0^{2\pi} d\phi \int_0^{z_{\rm BL}} dz\, u^r \mathcal{H}(u^r) \left[\rho' g z + \frac{1}{2} \rho {u^r}^2 + \frac{1}{2} \rho w^2 \right] , \tag{4.46}$$

where $z_{\rm BL}$ is the depth of the boundary layer, ρ_0 is the density of boundary-layer air, ϕ is the azimuth about the cold-pool center, T is the duration of the precipitation shaft, and $\mathcal{H}$ is the Heaviside unit step function. After solving these equations for V_0, U_0, and ρ_0', the results can be plugged into (4.41) and (4.42) to estimate the terminal time and radius.

4.7 Measuring in LES

To evaluate this theory, we will use large-eddy simulations of individual cold pools initialized as cold cylinders of air. To keep track of a cold pool's evolution, we will use a passive tracer whose mixing ratio is initialized to one within the initial cold pool and zero outside. As in Romps and Kuang [65], we will refer to this as the purity tracer. Since cold pools in LES do not retain a uniform, cylindrical shape, we must make some choices about how to calculate the cold pool's volume, radius, and density anomaly.

Let us define

$$\langle X \rangle = \int_0^\infty dz\, X q \rho \,,$$

where q is the purity mixing ratio and X is one of the following: 1, q, u, v, and ρ'. Here, u and v are the horizontal wind components and $\rho' = \rho(x,y,z,t) - \rho_{\rm env}(z, t=0)$, where $\rho_{\rm env}(z, t=0)$ is the initial profile of density in the environment. In all of the LES, the instantaneous two-dimensional distributions of these quantities are saved every two minutes. From these quantities, we can define a cold-pool height distribution $h(x,y,t)$, total mass $M(t)$, radial-velocity distribution $u^r(x,y,t)$, density-anomaly distribution $\rho'(x,y,t)$, mean density anomaly $\rho'(t)$, and radius $R(t)$. To find the correct expressions for these variables, we will find the expressions that give the correct answers for a uniform cylinder. For a cylinder with uniform density ρ, uniform purity q, and depth h,

$$\langle X \rangle = h \rho q X \,.$$

From this equation, we can see, for example, that $\langle 1\rangle^2/\rho\langle q\rangle$ equals the cold pool's height h. Therefore, for the LES output, we define the cold-pool height $h(x,y,t)$ as

$$h(x,y,t) \;=\; \frac{\langle 1\rangle^2}{\rho\langle q\rangle}\,, \tag{4.47}$$

where ρ is a constant representative density near the surface, and we define the total mass of the cold pool as

$$M(t) \;=\; \int_A d^2x\,\frac{\langle 1\rangle^2}{\langle q\rangle}\,, \tag{4.48}$$

where A is the area over which $\langle q\rangle$ is above some threshold value (we use 0.01 kg/m^2). Proceeding in the same way, we find that $u^r(x,y,t)$, $\rho'(x,y,t)$ and $\rho'(t)$ should be defined as

$$u^r(x,y,t) \;=\; \frac{\langle u\rangle x + \langle v\rangle y}{\langle 1\rangle\sqrt{x^2+y^2}} \tag{4.49}$$

$$\rho'(x,y,t) \;=\; \frac{\langle \rho'\rangle}{\langle 1\rangle} \tag{4.50}$$

$$\rho'(t) \;=\; \frac{1}{M}\int_A d^2x\frac{\langle \rho'\rangle\langle 1\rangle}{\langle q\rangle}\,. \tag{4.51}$$

To borrow a phrase from computer science, we are "overloading" the symbol ρ' to mean different things in different contexts in order to simplify the notation. When ρ' refers to a four-dimensional variable, it equals $\rho(x,y,z,t) - \rho_{\rm env}(z,t=0)$. When ρ' refers to a three-dimensional variable, it is given by equation (4.50). When ρ' refers to a one-dimensional variable, it is given by equation (4.51). In the text and figures that follow, context will make clear which definition is being used.

We define the cold-pool radius $R(t)$ somewhat differently so that it captures the location of the cold-pool front as accurately as possible. For a uniform cylinder, the radius R can be written as the following integral for any $n \geq 1$:

$$R \;=\; \frac{n+1}{n}\frac{\int_A d^2x\,\langle 1\rangle r^{n-1}}{\int_A d^2x\,\langle 1\rangle r^{n-2}}\,. \tag{4.52}$$

For a non-uniform cold pool, this will give the distance from the center to the edge that is farthest away in the limit of $n \to \infty$. Since this limit is noisy, we use $n = 10$, which gives an accurate and smooth $R(t)$. The radius obtained in this way is very similar to the one obtained by taking the square root of the area of $\langle q\rangle > 0.01$ divided by π. Finally, we diagnose the fractional entrainment rate ε as

$$\varepsilon \;=\; \frac{d}{dR}\log(M)\,. \tag{4.53}$$

LES #	Surface drag?	Enthalpy fluxes?	$T_{\rm cp}(K)$	$T_{\rm env}(K)$	$T_{\rm surf}(K)$
1	No	No	299	300	301
2	No	Yes	299	300	301
3	Yes	No	299	300	301
4	Yes	Yes	299	300	301
5	Yes	Yes	299	300	304
6	Yes	Yes	299.75	300	301
7	Yes	Yes	296	300	304
8	Yes	Yes	296	300	316
9	Yes	Yes	299.75	300	300.25

Table 4.1: A list of the large-eddy simulations indicating whether or not surface drag was present, whether or not surface enthalpy fluxes were present, the temperature of the cold pool $T_{\rm cp}$, the temperature of the environmental surface air $T_{\rm env}$, and the temperature of the sea surface $T_{\rm surf}$.

4.8 The large-eddy simulations

Table 4.1 describes the nine LES that are used to compare with the theory developed in the previous sections. All of the simulations were initialized with a motionless, cylindrical cold pool with a uniform temperature perturbation defined relative to the environment at the same height. For computational feasibility, all of the cold pools have an initial height H_0 and initial radius R_0 equal to one kilometer; larger initial heights and radii would have required larger computational domains. Both the cold pool and the environment are dry and have a dry-adiabatic lapse rate. A small amount of random noise is added to the initial temperature field to break the symmetry. For each of the nine simulations, Table 4.1 specifies whether or not surface fluxes of momentum (i.e., drag) or enthalpy are communicated between the surface and the atmosphere. In either case, the fluxes are calculated using the bulk aerodynamic formula, i.e., $-c_{ds}\rho|\vec{u}|\vec{u}$ or $c_{ds}\rho|\vec{u}|(T_{\rm surf}-T)$, with a drag coefficient $c_{ds}=1.5\times10^{-3}$. The temperatures in Table 4.1 specify the initial cold-pool surface air temperature $T_{\rm cp}$, the initial environmental surface air temperature $T_{\rm env}$, and the surface temperature $T_{\rm surf}$. The identifying numbers (i.e., #1 through #9) assigned to each simulation in Table 4.1 will be used throughout the paper.

All of the LES are performed using Das Atmosphärische Modell [DAM; 63], which is a fully compressible large-eddy model. All of the simulations are performed without radiation, without microphysics (all of the simulations are dry), and without planetary rotation. The domains have a model top at 3 km and a square horizontal domain that is sufficiently large to encompass the cold pool throughout the 3.5 hours of simulation (38.4 km square for all of the simulations). The horizontal grid spacing is $\Delta x=\Delta y=50$ m and the vertical grid spacing is $\Delta z=10$ m for $z<600$ m, $\Delta z=50$ m for $z>1300$ m, and smoothly transitioning in between.

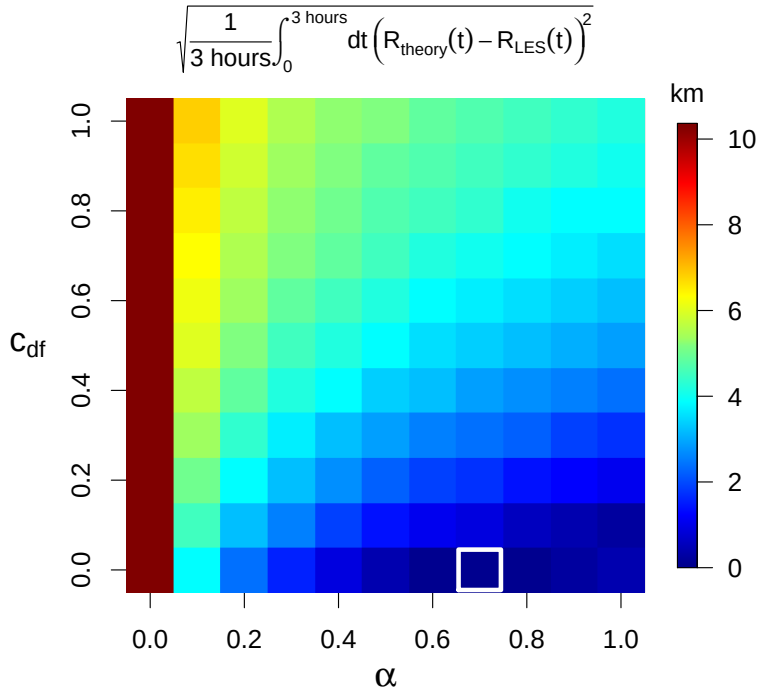

Figure 4.3: For LES #1 (no surface fluxes of momentum or enthalpy, and an initial 299/300/301 K temperature distribution), the 3-hour root-mean-square difference between the $R(t)$ diagnosed from the LES and the $R(t)$ governed by equations (4.19–4.23) for different values of (abscissa) α and (ordinate) c_{df}. The best fit occurs for $c_{df} = 0$ and $\alpha = 0.7$, which is highlighted with a white box; these values are used in all subsequent figures.

4.9 Comparing LES and theory

Our objective in this section is to compare the cold-pool theory with the large-eddy simulations of cold pools. Before we can do that, however, we must use the LES to find the appropriate values of α (the fraction of gravitational energy converted to cold-pool kinetic energy) and c_{df} (the form-drag coefficient). For this purpose, we use LES #1 and our full theoretical equations (4.19–4.23) to find the best choice of α and c_{df}. We use LES #1 for this exercise because it is the simplest of all the LES in the sense that it has neither surface drag nor enthalpy fluxes; including those surface fluxes would only increase the sources of potential error in the theoretical calculation and, therefore, add error to the calculated best-fit α and c_{df}. Also, to reduce the treatment of entrainment as a potential source of error, we give the theoretical equations the actual $\varepsilon(R)$ diagnosed from the LES.

Figure 4.3 plots the root-mean-square difference between $R(t)$ calculated from equations (4.19–4.23) and $R(t)$ calculated from equation (4.52). The best fits are obtained for $c_{df} = 0$, indicating that form drag is negligible. This is an interesting result, especially in comparison

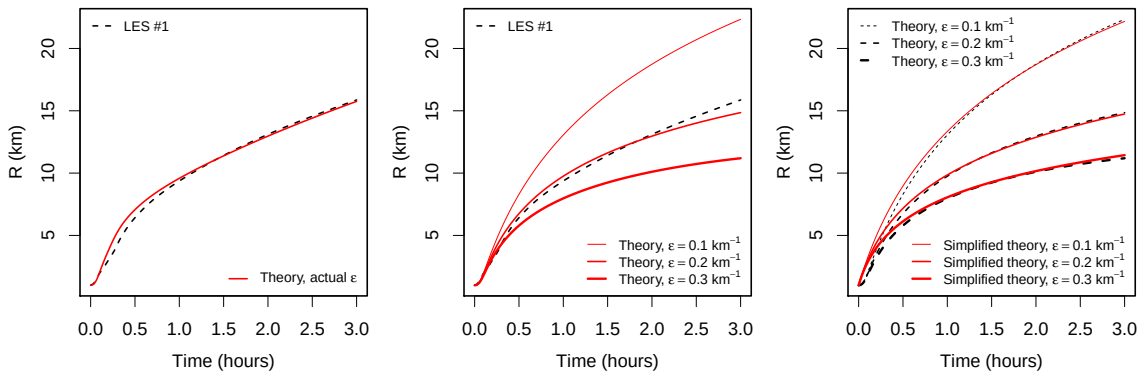

Figure 4.4: (left) A comparison of $R(t)$ for (dashed black) LES #1 and (solid red) the full theory given by equations (4.19–4.23) using the actual $\varepsilon(R)$ diagnosed from the LES. (middle) A comparison of $R(t)$ for (dashed black) LES #1 and (solid red) the full theory using a constant ε equal to 0.1, 0.2, and 0.3 km^{-1}. (right) A comparison of (dashed black) the full theory using constant ε and (solid red) the simplified theory given by equations (4.35–4.37) using the same constant ε. These panels demonstrate that the full numerical theory is an excellent match to the LES, and very little error is introduced by assuming a constant entrainment rate or by using the simplified governing equations.

with recent findings that cloud thermals experience significant drag [64] despite having, like cold pools, an internal vortex-ring circulation. These results are not inconsistent because wave drag was identified as a likely dominant source of drag for cloud thermals [66], whereas there is no wave drag in these simulations with neutral stratification. (Waves can be supported on the interface between the cold pool and the environment, but there is no way for those waves to propagate away from the cold pool and, therefore, no way for them to remove momentum from the cold pool.) Also, it is important to note that the entrainment drag is calculated as if the entrained air has zero momentum, which may overestimate the entrainment drag and, therefore, give a best fit with a less-than-realistic c_{df}. As for α, although it is difficult to tell from Figure 4.3, the best fit occurs for a value of 0.7. In other words, 70% of the cold pool's gravitational potential energy is converted to kinetic energy of the cold pool, with the remainder going into the kinetic energy of the environment. These values of $c_{df} = 0$ and $\alpha = 0.7$ will be used in all theoretical calculations henceforth.

The left panel of Figure 4.4 shows that the theoretical solution for $R(t)$ using the full theory with the $\varepsilon(R)$ diagnosed from the LES is, indeed, a good fit to the LES. But, in order to use the simplified equations derived in section 4.5, we must pick a constant fractional entrainment rate. The middle panel of Figure 4.4 shows that the full theory – i.e., equations (4.19–4.23) from section 4.4 – with a constant fractional entrainment rate of $\varepsilon = 0.2$ km^{-1} is also a good fit to the LES. For comparison, the solutions with $\varepsilon = 0.1$ and 0.3 km^{-1} are shown, which are poor fits. Next, we can evaluate the simplified theory – i.e., equations

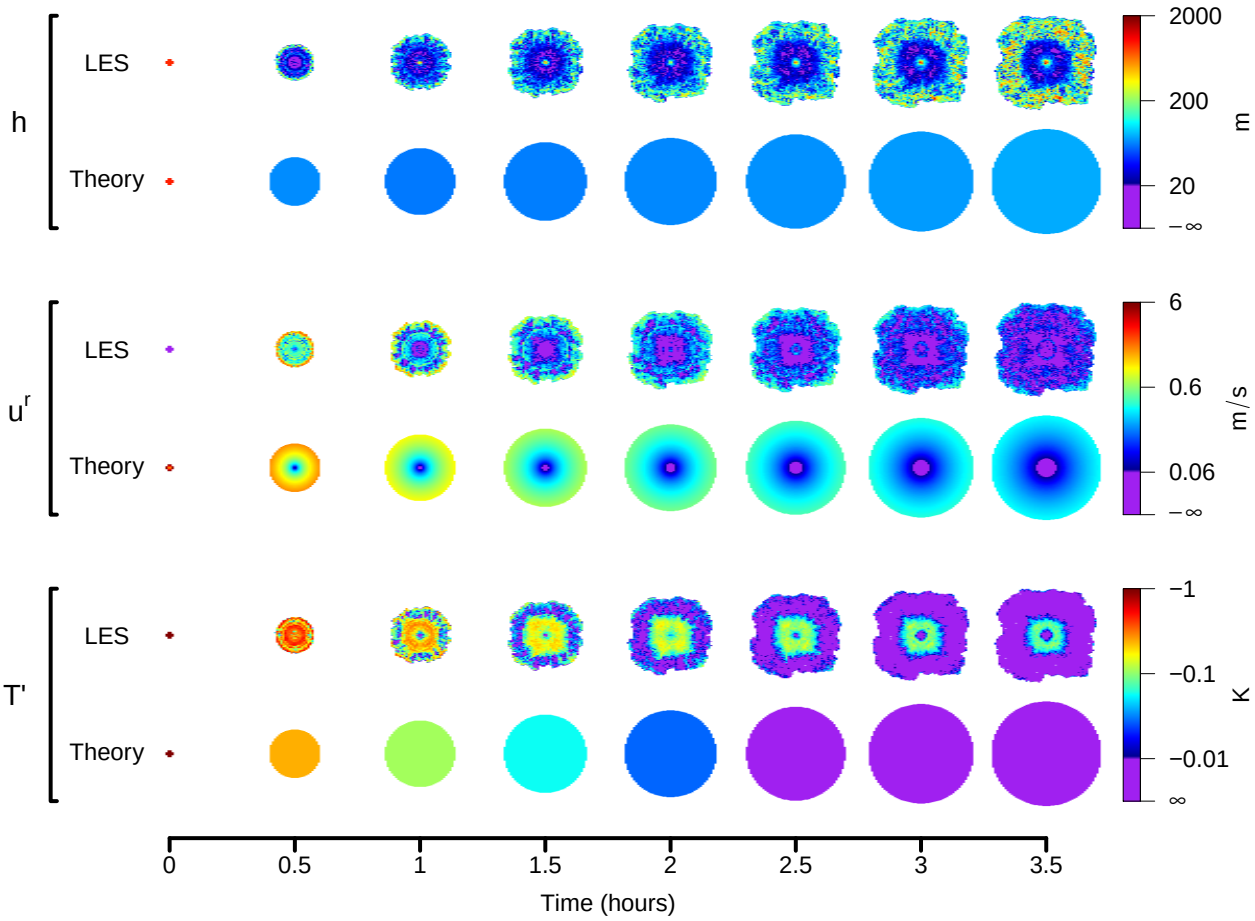

Figure 4.5: Snapshots of cold-pool properties from LES #4 in Table 4.1 (i.e., with surface enthalpy fluxes, surface drag, and an initial 299/300/301 K temperature distribution) and the corresponding theoretical solution using equation (4.36) for h, equations (4.2) and (4.31) for u^r, and equation (4.37) for ρ', which is then multiplied by $-\rho/T$ to express it as a temperature perturbation T'.

(4.35–4.37) from section 4.5 – by plotting their $R(t)$ against the $R(t)$ from the full theory. As argued in section 4.5, the full theory and simplified theory should agree quite well. Indeed, the right panel of Figure 4.4 confirms this.

Now, what do these LES and theoretical cold pools look like from a bird's-eye view? To give a sense for this, Figure 4.5 gives the plan view of $h(x, y, t)$, $u^r(x, y, t)$, and $\rho'(x, y, t)$ (multiplied by $-\rho/T$ to convert it to a temperature perturbation) for LES #4 (arguably, the most realistic of the nine simulations) at 30-minute intervals, along with the corresponding fields predicted from the simplified theory (equations 4.35–4.37). Figure 4.6 plots the same information, but azimuthally averaged at 30-minute intervals. Of course, there is a great

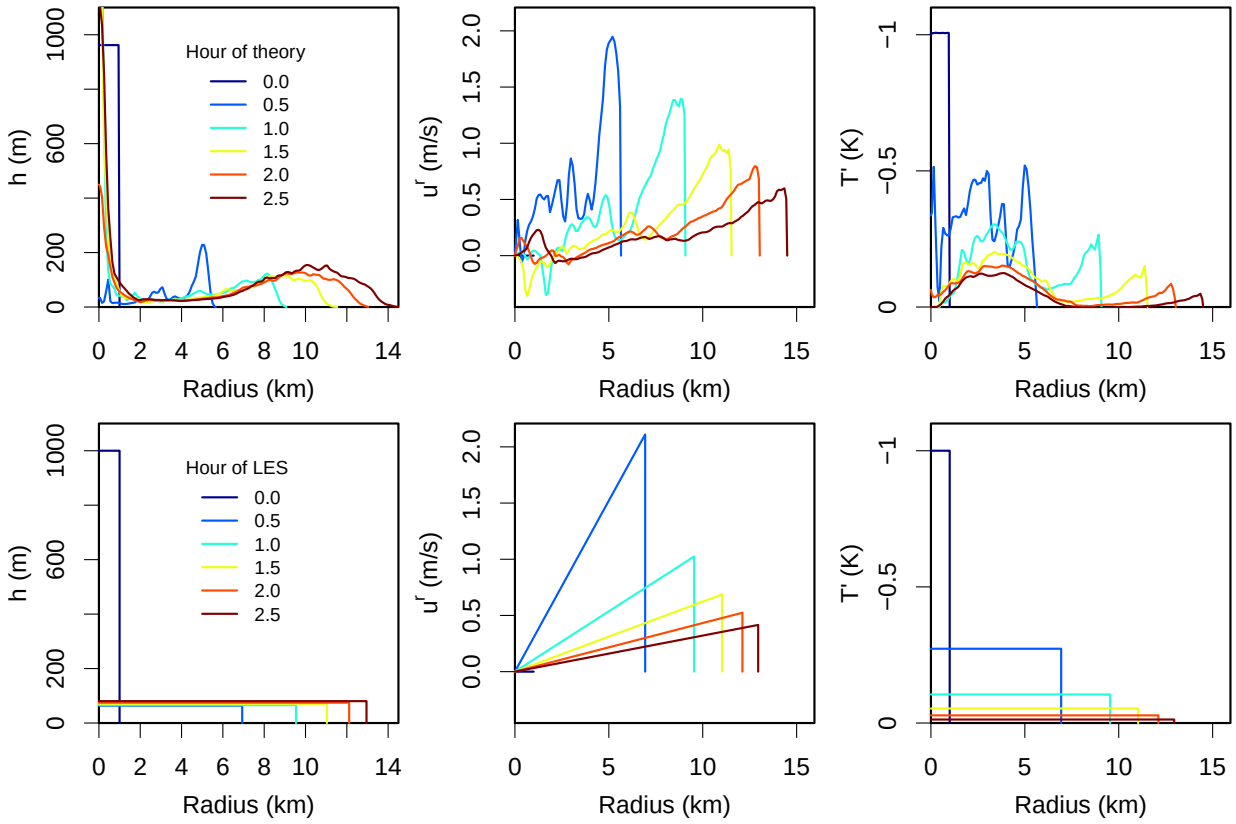

Figure 4.6: (top) Azimuthal averages of cold-pool height h, radial velocity u^r, and temperature anomaly T' for LES #4 at 30-minute intervals and (bottom) same, but from the corresponding theoretical solution using equation (4.36) for h, equations (4.2) and (4.31) for u^r, and equation (4.37) for ρ', which is then multiplied by $-\rho/T$ to express it as a temperature perturbation T'.

deal of internal structure to real cold pools that cannot be captured by a uniform cylinder. Nevertheless, the simplified theory does a decent job of capturing the size and horizontally averaged properties of the LES cold pool. Note that, in the azimuthal averages, many of the largest discrepancies between the LES and theory occur at small radii, which make a small contribution to the cold pool's area.

A key conclusion from section 4.5, and codified in equation (4.35), is that $R(t)$ is largely insensitive to drag and surface enthalpy fluxes. We can check this by comparing the $R(t)$ from LES #1 through #4, which share the same initial temperature distribution but differ in whether or not they have surface drag. These $R(t)$ are plotted in the left panel of Figure 4.7, where $R(t)$ is on the abscissa to be consistent with the other panels. The dashed curves have no surface drag, while the solid curves do. The black curves have no surface enthalpy

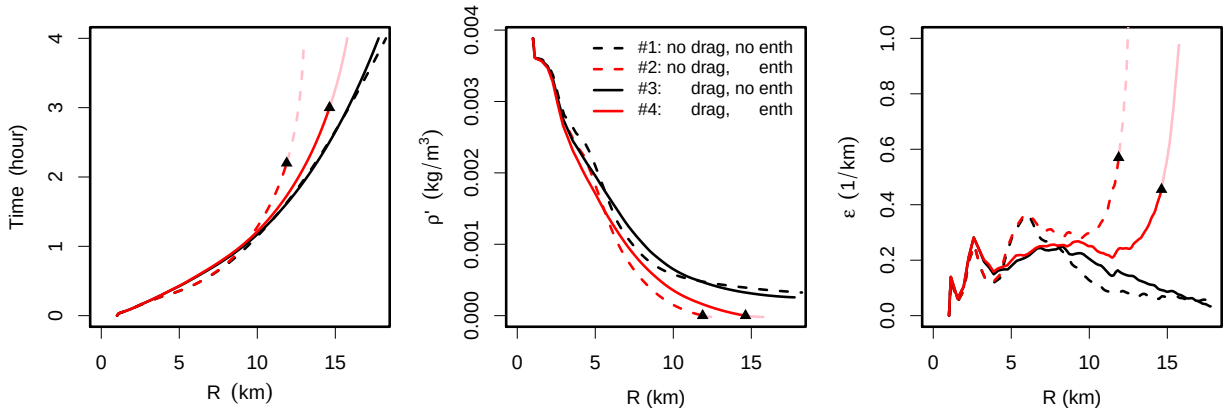

Figure 4.7: As a function of cold-pool radius R, (left) time, (middle) cold-pool density anomaly, and (right) cold-pool entrainment rate for LES #1–4 in Table 4.1 (i.e., with an initial 299/300/301 K temperature distribution). Simulations with surface enthalpy fluxes are red; those without are black. Simulations with surface drag are solid; those without are dashed. Triangles denote where the cold pools cease to be "cold" pools; curves beyond those points are faded to emphasize that those are no longer cold pools, strictly speaking. In the left panel, note that the four $R(t)$ curves are very similar, indicating an insensitivity to surface enthalpy and momentum fluxes. In the right panel, note that the entrainment rates are also very similar up to the point where cold pools start to have enhanced mixing due to patches of neutrally or positively buoyant air.

flux, while the red curves do. The triangles denote where the cold pools terminate (i.e., cease to be cold); trajectories beyond those radii are plotted in pink. All of the cold pools have very similar $R(t)$, in agreement with the theory.

Significant deviations from a common $R(t)$ occur only when the cold pools begin to have significant regions of $\rho' \lesssim 0$, i.e., as they are dying. This only occurs for the red curves because only those simulations have surface enthalpy fluxes. The middle panel of Figure 4.7 shows the mean ρ' as a function of radius. As the mean ρ' approaches zero, the entrainment rate, shown in the right panel of Figure 4.7, starts to grow rapidly. This occurs because the stratification between the cold pool and its environment is removed, allowing enhanced mixing by mechanical forcing and even by buoyant convection for regions of the "cold" pool with $\rho' < 0$.

For LES #1 and #3, which have no surface enthalpy fluxes, the total mass anomaly $V\rho'$ does not change in time, so the cold pool remains cold forever. It is intuitive that such a cold pool would continue to spread until it has blanketed the entire domain. Equation (4.29), however, suggests that this might not happen if ε exceeds $2/R$. As discussed in section 4.5, this would cause PE to grow as the cold pool expands, which would happen at the expense of KE. If ε remained larger than $2/R$ for long enough, this could grind the cold pool to a

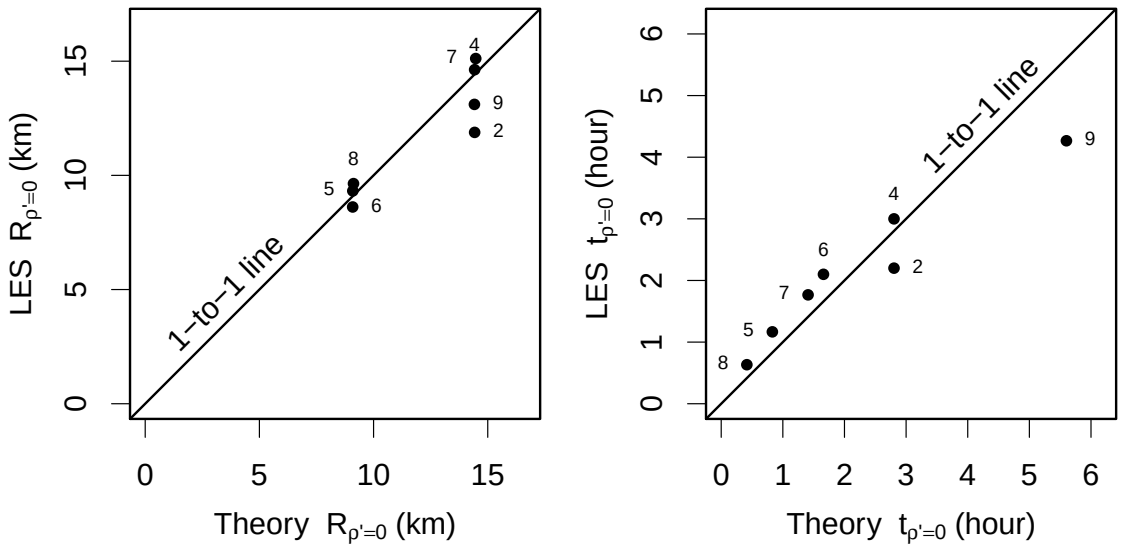

Figure 4.8: (left) For LES #2 and #4–#9, the radii at which the cold pools terminate (i.e., cease to be cold) plotted against the corresponding theoretical prediction. Note that LES #1 and #3 are not included because their lack of surface enthalpy fluxes means that they never cease to be cold (i.e., never achieve $\rho' = 0$). (right) Same, but for the time at which the cold pools terminate.

halt, leaving untapped PE sitting motionless in the atmosphere. This is an absurd result, so something must prevent this from happening. That "something" is that ε must decrease with radius to stay roughly at or below a bound of $2/R$. This behavior can be seen in the black curves in the right panel of Figure 4.7. At about 7 km, $2/R$ becomes small enough to equal ε, but ε decreases to stay at or under the $2/R$ bound for all $R > 7$ km.

Another set of key theoretical predictions are equations (4.38) and (4.41), which give expressions for the terminal radius $R_{\rho'=0}$ and the terminal time $t_{\rho'=0}$. Figure 4.8 plots the terminal radius and time from the seven LES with surface enthalpy fluxes against the corresponding predictions from equations (4.38) and (4.41), respectively. One-to-one lines are added for visual reference. Although not perfect, the simple theory does a good job of predicting the location and timing of cold-pool death.

It is interesting to note that LES #4, which has surface drag, terminates at a *larger* radius and *later* time than LES #2, which is the same in all respects except that it has no surface drag. This may be counterintuitive since it is natural to imagine that surface drag would slow down the cold pool, leading to an earlier demise at a smaller radius. To the contrary, the addition of surface drag reduces the low-level wind speed relative to the bulk of the cold pool, thereby reducing the enthalpy fluxes. Since it is the zero crossing of ρ' that terminates a cold pool, surface drag leads to a later termination at a larger radius.

4.10 Summary and Discussion

With the goal of understanding the dynamics of real cold pools, we have derived the governing equations for a uniform, cylindrical cold pool. Inspection of the magnitudes of terms in the equations reveals that the cold-pool dynamics has only a weak dependence on surface drag that can be neglected. With this and some other well-justified approximations, the governing equations reduce to a very simple theory for cold-pool dynamics, given by equations (4.35–4.37). The cold-pool radius is a function of time that depends only on the initial radius, the initial gravitational potential energy, and the fractional entrainment rate.

These equations make predictions for the lifetime and final size of cold pools, defining the demise of a cold pool as when it ceases to be cold on average. The expressions for those terminal sizes and times are given by equations (4.38) and (4.41) for an initially stationary cold pool, or by equations (4.41) and (4.42) for a more realistic cold pool with initial values estimated according to equations (4.44–4.45). Although entrainment dramatically reduces ρ', the terminal radius – defined as the cold-pool radius when $\rho' = 0$ – has no dependence on the entrainment rate. By quickly "hiding" the coldness of the cold pool from the surface, entrainment simplifies the estimation of surface fluxes without affecting the total enthalpy fluxes needed to terminate the cold pool; this leads to a very predictable terminal radius that does not depend on the precise value of the entrainment rate. The equations show that the final radius is tightly constrained to be in the vicinity of $\sim$14 times the initial radius, while the terminal time can range over several orders of magnitude. Comparison with large-eddy simulations, as shown in section 4.9, validates the simple theory and its predictions for cold-pool sizes and lifetimes.

We can also compare our results to previous studies that have measured the sizes and lifetimes of cold pools. Tompkins [78] studies cold pools in a large-eddy simulation of tropical unorganized convection and finds the mean maximum radius to be 8.6 km. It is important to note, however, that Tompkins [78] uses a very different definition of cold-pool radius. Here, we measure the radius as the distance from the center of the cold pool to the outer perimeter of the original cold-pool air, whether or not it is still "cold"; Tompkins [78] measures the radius from the center of the cold pool to the perimeter of the currently "cold" air (specifically, air with buoyancy less than -0.005 m s^{-2}, or a potential temperature anomaly less than -0.15 K). Feng et al. [19] studies cold pools in an LES using a similar definition (with a buoyancy threshold of -0.003 m s^{-2}) and finds a similar result: a mean maximum radius of 6.4 km. As seen in Figure 4.5, the definition of radius used by Tompkins [78] and Feng et al. [19] gives a maximum radius that is only about half as large as the terminal radius. If we account for this by doubling their reported maximum radii, we infer that they simulated cold pools with mean maximum radii of about 13–17 km. This agrees with the theory presented here, which predicts a $\sim$14-km terminal radius for a cold pool with an initial radius of 1 km and $H_0\rho_0'/R_0|\rho_s'| \sim 1$.

The theory also agrees well with the reported lifetimes. Tompkins [78] reports a mean cold-pool lifetime of 2.5 hours and a mean initial temperature anomaly of -1 K. Using this temperature anomaly to set ρ', using a fractional entrainment rate of 0.2 km^{-1} (as diagnosed

in section 4.9), and using an initial radius and height of 1 km, equation (4.41) predicts a lifetime of 2.8 hours, which is in close agreement with 2.5 hours. Feng et al. [19] report a shorter lifetime of 1.2 hours, but this agrees, at least qualitatively, with their smaller initial temperature anomaly of −0.5 K (see their Figure 6d). Changing the temperature anomaly from −1 K to −0.5 K, while holding the other variables constant, reduces the lifetime predicted by equation (4.41) from 2.8 hours to 2.1 hours. Differences in the air-sea temperature difference or in the initial cold-pool height or radius could easily explain the remaining discrepancy.

It is more difficult to observe cold pool sizes in nature, and even more difficult to measure their lifetimes. At least anecdotally, it appears that cold pools reach a wider range of sizes over the real tropical oceans than they do in large-eddy simulations of the tropical maritime atmosphere. For example, Black [3], Zuidema et al. [84], and Feng et al. [19] observe real cold pools over tropical oceans with radii of 50–100 km, 20–30 km, and 5–25 km, respectively. As noted in the discussion of equation (4.38), it is difficult to generate a wide range of terminal radii by varying just the normalized height H_0/R_0 or the normalized density-anomaly $\rho_0'/|\rho_s'|$ since they contribute to the terminal radius with only a one-third power. Instead, the variance in the initial radius in equation (4.38) or initial mass anomaly in (4.42) is likely the single largest contributor to the observed variance in the terminal radius. For example, assuming a plausible boundary-layer depth H_0 of 1 km and a plausible ratio of $\rho_0'/|\rho_s'| = 1$, equation (4.38) would require an initial radius of $R_0 = 20$ km to produce a terminal radius of 100 km. Of course, this does not imply a need for a single cylindrical rain shaft that is 40-km across. By equation (4.42), it would also suffice to have five, nearby, 2-km-radius rain shafts of 30-minute duration that replenish the air in their boundary-layer volume 20 times during their lifetime, which would be possible with modest radial winds of 10 m s^{-1} at the edge of the rain shafts.

In the study of convection, convective entrainment is often cited as the biggest obstacle to developing advanced theories of convective updrafts [68]. Based on the results shown here, we suspect that cold-pool entrainment may prove to be as thorny an issue for cold pools as convective entrainment has been for convection. The similarities are striking. Consider, for example, that a bulk-plume model treats updrafts as homogeneous at each height, and our "bulk-pool" model treats cold pools as homogeneous at each time. And, as in a bulk-plume model, we have been forced to specify an entrainment rate that is motivated by empiricism rather than theory. Fortunately, a cold pool's terminal radius is independent of the entrainment rate, so the theory presented here for cold-pool sizes is likely to stand the test of time. On the other hand, the equations given here for a cold pool's velocity $U(t)$ and terminal time $t_{\rho'=0}$ are highly dependent on the chosen entrainment rate. Since ε may vary significantly with initial radius, or it may evolve in important ways at larger radii (as suggested by the black curves in the right panel of Figure 4.7), the extrapolation of our results for $U(t)$ and $t_{\rho'=0}$ to cold pools with R_0 much larger than those simulated here is not without risk. To know for sure how well these equations and assumptions apply to larger cold pools, more work is needed on simulating and observing a wide range of cold pool types, and on developing theories for cold-pool entrainment.

Chapter 5

Convective Self-Aggregation, Cold Pools, and Domain Size

In this final chapter we study cold pools not in isolation (Chapters 3 and 4), nor in interaction with individual convective cells (Chapter 2), but rather in interaction with a whole system of *organized* convection.

In organized convection the spatial pattern of convection is fixed and persistent over time. It has been found in both observations and numerical studies [31, 22, 75], across a wide range of scales. In particular, recent numerical studies [7, 36, 54] with cloud-resolving models (CRMs) have shown that horizontally quasi-homogeneous tropical convection can be unstable, yielding spontaneous development of a circulation featuring a moist, convecting patch and a dry, non-convecting patch. This *self-aggregated* state has significantly different horizontal-mean properties than the quasi-homogeneous state from which it formed: it is significantly drier in the mean, for instance, and hence exhibits much stronger mean longwave radiative cooling (LRC). Horizontal variations in LRC are important as well, as differences in LRC between moist and dry columns play a critical role in the feedbacks responsible for self-aggregation; see Bretherton, Blossey, and Khairoutdinov [7] and Muller and Held [54] for details.

These two papers also investigated the sensitivity of aggregation to various parameters, one of these being the domain size L. Both studies found that quasi-homogeneous states will only self-aggregate if $L \gtrsim$ 200–300 km. We will show in this chapter that this threshold behavior is due to cold pools, and will investigate more generally why aggregation is favored by larger domains.

5.1 Numerical simulations

All simulations in this paper were performed using DAM (See Section 2.3 for details and further references). For this study, we performed runs on both three-dimensional (3D) square domains as well as effectively two-dimensional (2D) bowling-alley domains, all of various

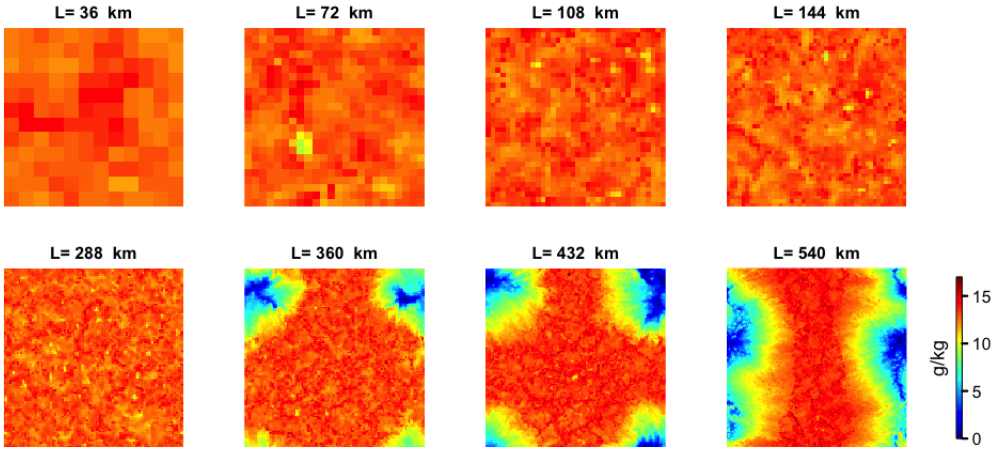

Figure 5.1: Horizontal specific-humidity distribution [g/kg] at $z = 500$ m on day 60 for various domain sizes L in the presence of cold pools. Note the sharp transition to an aggregated state between $L = 288$ and $L = 360$ km.

sizes. All domains were doubly-periodic with a horizontal grid spacing of 3 km, and simulations were run over a non-dynamical ocean with a fixed sea-surface temperature of 301 K.[1] Surface enthalpy fluxes were calculated using a bulk aerodynamic formula and interactive shortwave and longwave radiative fluxes were calculated using the Rapid Radiative Transfer Module [53].

Each run was 60 days long and was initialized with an aggregated distribution of water vapor similar to that used in Muller and Held [54].[2] The initial temperature profile was obtained from a small-domain (i.e., non-aggregated) simulation of radiative convective equilibrium. We turned off large-scale dynamical forcings, set initial horizontal winds to zero, and nudged the horizontal mean winds to zero over a time scale of two hours, both for consistency with previous work [54, 7] and because we found these adjustments conducive to aggregation.

[1] This choice of SST is typical of the tropical oceans, and is the same as that used in Bretherton, Blossey, and Khairoutdinov [7]. It is also squarely in the range of SSTs shown to be conducive to aggregation in Khairoutdinov and Emanuel [36].

[2] Here, the lowest-level specific humidity q started at 16 g/kg in the center of the domain and decreased to 8 g/kg at the edge, and this horizontal distribution decreased exponentially with height with a scale height of 3 km. The initial horizontal q distribution was a radial function for the square domains and was linear along the long dimension in the bowling-alley domains.

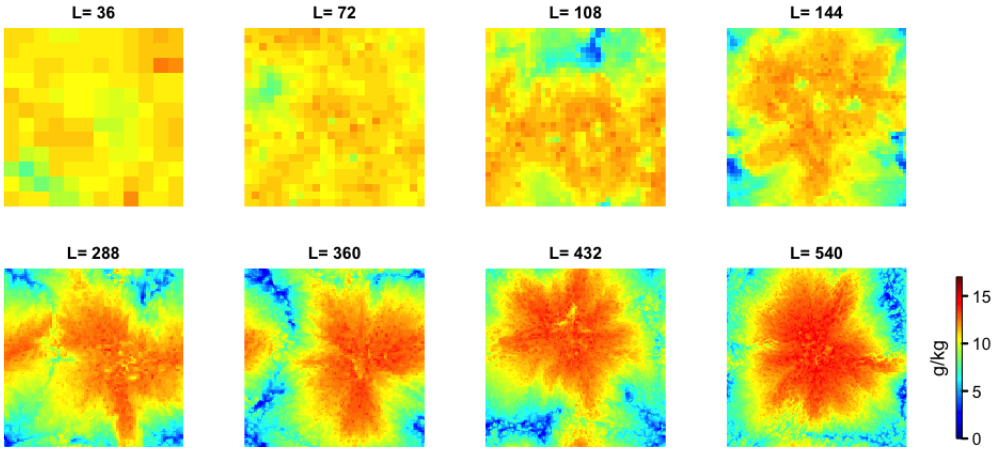

Figure 5.2: Same as Figure 5.1, but in the absence of cold pools. Note that, in contrast to Figure 5.1, aggregation occurs at domain sizes less than 300 km and only gradually weakens as L decreases.

5.2 Aggregation in 3-D

As a first task, we reproduced the phenomenon of convective self-aggregation in 3D, as well as its critical dependence on domain size. Figure 5.1 shows x-y snapshots of specific humidity q on day 60 at $z = 500$ m for various domain sizes L. Aggregation, with its trademark dry patches in regions of steady-state subsidence, is clearly evident for domain sizes larger than $L \approx 300$ km. This is in rough agreement with the critical domain size of 200–300 km found in Bretherton, Blossey, and Khairoutdinov [7] and Muller and Held [54].

To investigate the role of the boundary layer (BL) in convective aggregation, we eliminated cold pools by turning off low-level ($z < 1000$ m) evaporation of precipitation.[3] In this no-cold-pool scenario, we found that self-aggregation *occurs at all domain sizes*, but gradually decreases in strength as the domain size L decreases. This can be seen in Figure 5.2, which plots the same quantities as Figure 5.1 for the simulations with no cold pools. It appears that cold pools are responsible for inhibiting convective aggregation in small domains, and for generating a discontinuous dependence of self-aggregation on domain size.

As stated above, our ultimate goal is to explain why larger domains favor convective aggregation. Since cold pools neither generate nor maintain convective self-aggregation, it is natural to study self-aggregation in their absence. Although self-aggregation is a continuous function of domain size in the absence of cold pools – as opposed to discontinuous with cold pools – our working hypothesis is that the underlying physics of self-aggregation is the same

[3]We chose $z = 1000$ m for the evaporation cut-off height simply because it seemed sufficiently high enough to kill the cold pools. Lowering the cut-off height from 1000 to 600 m was enough to reintroduce cold pools.

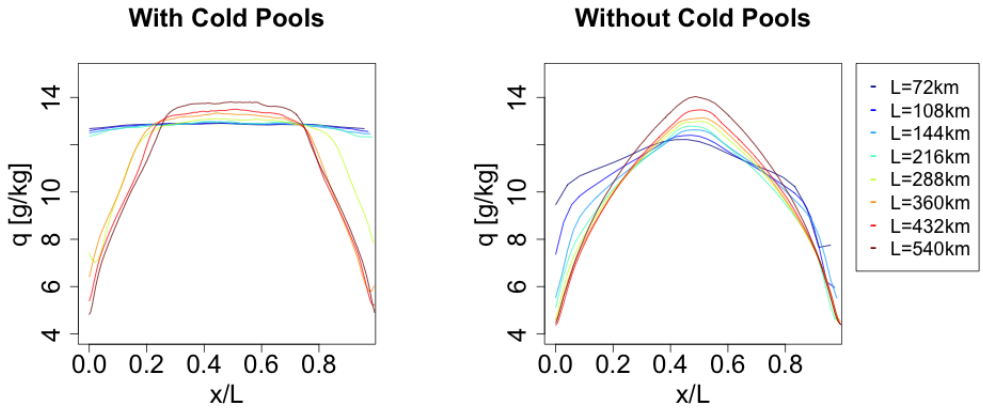

Figure 5.3: **Left**: Steady-state B-L specific humidity q for 2-D runs of various L with cold pools. Note the sharp transition from constant to unimodal humidity between $L = 216$ and $L = 288$ km, analogous to the 3-D results in Figure 5.1. **Right**: Same as left panel but without cold pools. Note the existence of aggregation below the threshold exhibited in the left-hand panel and the gradual weakening of aggregation as L decreases, analogous to the 3-D results in Figure 5.2.

in both cases. Furthermore, as a practical matter, it is easier to diagnose the mechanisms responsible for a continuous transition than for a discontinuous one.

5.3 Aggregation in 2-D

To facilitate the analysis of the domain-size dependence of self-aggregation, we performed a suite of similar 60-day runs over a bowling-alley domain where the long domain edge (along the x-axis) varied and the short domain edge (along the y-axis) was fixed at 12 km. We averaged over y, yielding what were effectively 2D runs, which were then amenable to streamfunction analysis and study of the steady-state circulation. The set-up of the simulations was identical to that of the full 3D runs above except for the domain dimensions. Steady-state values of variables were obtained by averaging over the last twenty days of each run. Boundary-layer averages were also employed, where the height h of the BL is defined by the height z at which $d^2\theta/dz^2$ is a maximum, where θ is the steady-state potential temperature and z is restricted to 200 m $< z <$ 4000 m.[4]

We first performed simulations with cold pools. The left-hand panel of Figure 5.3 shows horizontal profiles of steady-state q, averaged from $z = 0$ to h. Aggregation is evident for

[4]For unaggregated domains the $\theta(z)$ profile is obtained by horizontally-averaging θ over the whole domain. For aggregated domains, however, the $\theta(z)$ profile is obtained by horizontally-averaging over only the driest 10% of columns, since the BL height is lowest there due to the large-scale subsidence over those columns.

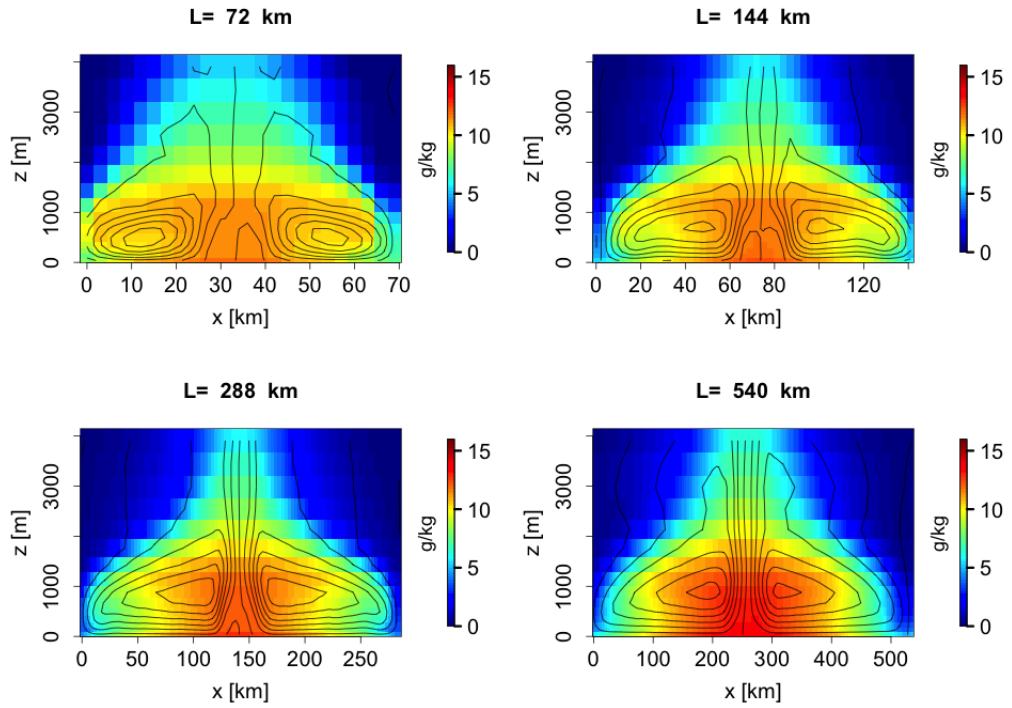

Figure 5.4: Steady-state specific humidity q overlaid with streamfunction contours for 2D runs without cold pools for domains with L= 72, 144, 288, and 540 km. The contour spacings are 100, 125, 175, and 275 kg/m/s respectively. These values are chosen so that each plot has the same number of contour lines. In each plot, the circulation around the streamfunction maximum consists of a shallow circulation confined to $z \lesssim 3500$ m, as well as a deep circulation that extends above $z \approx 3500$ m. Note that the number of deep convection contours increases with L, implying that the magnitude of the deep circulation relative to that of the shallow circulation increases as L increases.

domain sizes bigger than $L \approx 250$ km, again in agreement with a critical domain size in the 200–300-km range.

We then performed these runs without cold pools, as in the previous section. The results are shown in the right-hand panel of Figure 5.3. Note the gradual, but pronounced, increase in aggregation strength as L increases towards 200 km, similar to that of the 3D runs in Figure 5.2. This shows that the 2D and 3D phenomena are quite analogous, so studying the 2D case should provide insight into the 3D case. We perform streamfunction analyses of our 2D runs in the next section.

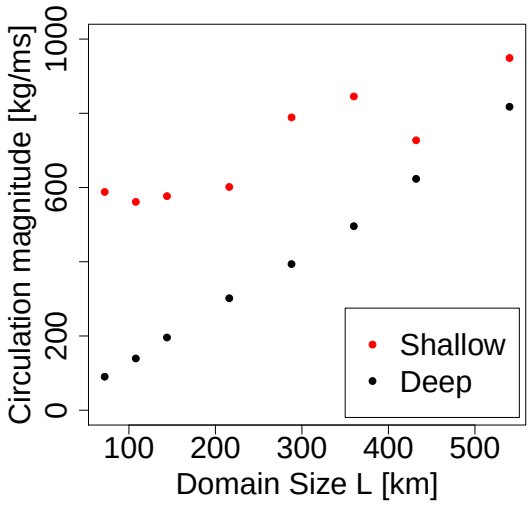

Figure 5.5: Circulation magnitudes as a function of domain size L. The magnitude D of the dry, deep circulation is given by the black dots, while the magnitude S of the humid, shallow circulation is given by the red dots. Note that D varies linearly with L, whereas S varies by only $\sim 50\%$. Therefore, at small L, the shallow circulation dominates, moistening the dry region and weakening aggregation.

5.4 Streamfunction analysis

We begin by plotting the steady-state water-vapor distribution and streamfunction contours for a few representative cases in Figure 5.4. The streamfunction may be naturally divided into a shallow circulation[5] (confined below $z \sim 3500$ m) and a deep circulation (extending above $z \sim 3500$ m). The contour spacings for each plot in Figure 5.4 are chosen so that each plot has the same number of contour lines. Note that the number of deep convection contours increases with L, implying that the magnitude of the deep circulation relative to that of the shallow circulation increases as L increases. We check this by plotting the magnitudes of these circulations as functions of L in Figure 5.5. We take S to be the difference between the low-level streamfunction maximum C and the maximum value of the streamfunction along the $z = 3500$ m contour. We then take D to be the maximum value of the streamfunction along the $z = 3500$ m contour, so that $D + S = C$.

Figure 5.5 confirms that the ratio of D to S grows as L increases: the shallow circulation S varies by only about 50% as L ranges from 72-540 km, whereas D varies almost perfectly

[5] A secondary shallow circulation was also observed in Bretherton, Blossey, and Khairoutdinov [7] and Muller and Held [54].

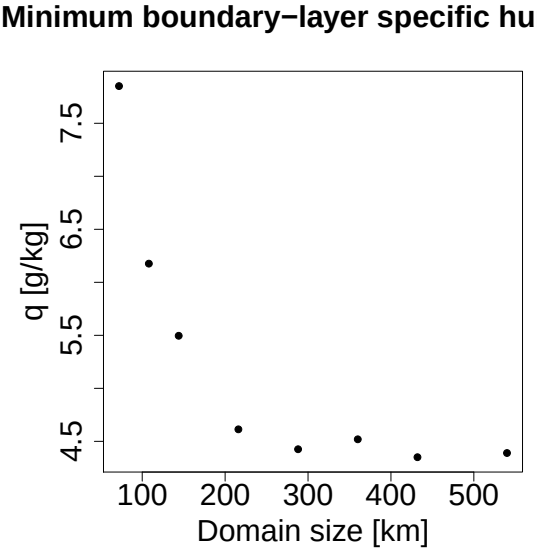

Figure 5.6: Aggregation strength, as measured by the minimum BL specific humidity $q_{\min}$, plotted as a function of domain size L. Note that $q_{\min}$ approaches its asymptotic value at a characteristic domain size of 200–300 km, which is where the critical domain size lies in the simulations with cold pools.

linearly with L. Thus *D scales with L whereas S does not*, and we contend that this is the root cause of the observed domain-dependence of aggregation: S dominates at small domains, moistening the dry region and weakening aggregation. More precisely, if we consider the half of the dry region between $x = 0$ and the x-value of the low-level streamfunction maximum, then C is the magnitude of the circulation feeding the BL of this half. The average specific humidity q_C of the air subsiding into this region will be a weighted sum of contributions from S and D, which have characteristic specific humidities $q_S > 0$ and $q_D \approx 0$. Since D is the only quantity in q_C that scales with L, *q_C will increase as L decreases.*

To assess the length scales over which this transition occurs, we calculated the minimum values $q_{\min}$ of the steady-state BL humidity distributions in the right-hand panel of Figure 5.3. These values are shown in Figure 5.6 as a function of domain size L. It is apparent that $q_{\min}$ approaches an asymptotic value at a characteristic domain size of 200–300 km, just where the critical domain size lies in the simulations that include cold pools.

5.5 The effect of cold pools on aggregation

The analysis of the previous section explains why aggregation gradually weakens as L decreases in our no-cold-pool simulations, but does not address how or why cold pools inhibit

aggregation below the critical domain size. To investigate this, we performed a 2D simulation with $L = 216$ km with initial conditions given by the day 60 snapshot of our earlier $L = 216$ km no-cold-pool run; this gave our run an initial aggregated water-vapor distribution similar to that shown for $L = 216$ km in the right panel of Figure 5.3. For this new run, we turned the cold pools back on and watched the convection disaggregate. We found that the boundary layer in the dry region becomes fully moistened by about day 11, whereas the lower and upper troposphere do not fully moisten until about day 17. This points to a sequence of events whereby the cold pools first moisten the dry-patch boundary layer, followed by deepening convection that moistens the free troposphere. The larger the domain, the drier the boundary layer in the dry patch and the longer the distance the cold pools must travel to bring moisture there. Both of these effects prevent the cold pools from homogenizing moisture and convection above the observed critical domain size.

Chapter 6

Concluding Material

6.1 Summary of main results

The introduction to this thesis posed several questions about cold pools, their dynamics and thermodynamics, and their interaction with convection. We compile the central results addressing these questions in Table 6.1 below.

6.2 Observational tests and future work

Given these results, it is natural to ask how they might be confirmed in the real world (rather than just in simulations), and what some logical next steps might be.

Let us begin with empirical confirmation. Some of our results could be empirically verified quite easily. For instance, to test the effect of the surface in inhibiting buoyant accelerations, one could simply take blocks of wood of various aspect ratios and submerge them in a tank of water, both far from and close to a lower boundary, and then release them, observing the differences in acceleration. Empirical tests of our formulae for the radius and time of death of density currents might similarly be made with laboratory density currents in a lock-release type experiment [26], but with a temperature difference between the current and its lower boundary.

Testing the dominance of inertial forcing over buoyant forcing in triggering new convection is probably not possible in a laboratory setting, since moist convection does not scale down and the observation of vertical velocities in dry convection (without cloud condensate serving as a natural conditional tracer) is difficult. With ample resources, though, one could take comprehensive observations of naturally occurring cold pools and ask, for instance, whether vertical accelerations at the gust fronts depend linearly on the downdraft height H, with all other variables (such as B_0 and h) held equal; if so, that confirms that the inertial forcing (which is proportional to H) dominates over the buoyant forcing, which is insensitive to H.

As for future work: the conclusions of each individual chapter have discussed directions for future work on each specific topic. But perhaps it is worth stepping back here to ask how

Ch.	Eqn.	Meaning
2.	$\frac{a_i}{a_b} \sim \frac{H}{h} > 1$	The inertial acceleration a_i dominates over the buoyant acceleration a_b at a cold pool's edge because the former scales with the initial heigh H of the downdraft, whereas the latter scales with the smaller height h of the gust front.
3.	$\beta = (-\partial_z p_\beta)/\overline{\rho}$ $p_\beta^{\text{free}} = \frac{gH\lvert\Delta\rho\rvert}{2} > p_\beta^{\text{surf}}$	The effective buoyancy β is the gradient of the buoyancy pressure p_β , whose magnitude for a free parcel is set by the hydrostatic pressure anomaly $gH\lvert\Delta\rho\rvert/2$. When parcel diameter D increases β decreases, because for $D/H > 1$, D sets the vertical scale over which p_β declines. Surface parcels experience smaller p_β, hence smaller β, due to symmetry breaking by the surface.
4.	$R_{\rho'=0} \approx R_0 \left(\frac{9V_0\rho_0'}{2\pi c_{ds}\lvert\rho_s'\rvert}\right)^{1/3}$	The radius $R_{\rho'=0}$ at which a cold pool terminates is determined by the cold pool's initial heat deficit, expressed as a mass anomaly $V_0\rho_0'$, and the rate-per-unit-distance at which this anomaly is depleted, determined by $c_{ds}\lvert\rho_s'\rvert$. A typical value is $R_{\rho'=0} \approx 14R_0$, give or take a factor of two.
5.	$D \sim L$ $S \nsim L$	The magnitude of the deep circulation D in a self-aggregated convective system scales with domain size L, whereas the shallow circulation S does not. Since the former feeds dry air and the latter moist air into the dry patch, larger L favors a drier dry patch, and hence stronger aggregation.

Table 6.1: A summary of this thesis's central results.

future long-term projects, like this thesis, should be directed to maximize impact on climate modeling and global warming uncertainty.

While we advocated in the introduction for a bottom-up approach to cloud physics which can put cloud parameterizations on a firmer footing, the unanswered questions about clouds and convection are too numerous to try and tackle all at once. Thus, we must somehow identify which questions are most crucial for reducing cloud-related uncertainty in climate models. This should also be done in light of the fact that computational capabilities will soon allow for non-hydrostatic, convection-permitting GCMs, which may not require convective parameterizations but will still require parameterizations of cloud microphysics, turbulence, and radiation, all of which influence cloud-related uncertainty in present-day GCMs.

With this in mind we propose an experiment in which a CRM with modular plug-and-

play microphysics, turbulence, and radiation parameterizations [such as the System for Atmospheric Modeling, 37] is used to create a virtual 'ensemble' of models, each with different permutations of the various parameterizations. This could be thought of as a cloud-resolving analog of the ensembles used for global warming intercomparison projects, e.g. CMIP5 [76]. One could perform warming experiments with this ensemble, and diagnose feedbacks and their uncertainties across the ensemble, just as for CMIP5. In contrast to CMIP5, though, for any two models that differ, there would be a sequence of models *differing in only one parameterization at a time* connecting them. Thus it would be possible to diagnose the source of differences amongst models, and thus determine which parameterizations cause the most uncertainty. Furthermore, if the coefficient of variation in cloud feedbacks is significantly less than for CMIP5, then this suggests that convection itself (which is resolved by the CRM but not the GCM) may be the leading cause of uncertainty in GCMs, rather than microphysics or turbulence schemes.

Such knowledge would be extremely helpful in guiding first-principles, physics-oriented research like that presented in this thesis. If cloud microphysics was the largest source of uncertainty, for instance, that would then suggest shifting our focus to that subject, rather than continuing to study, say, convective fluid dynamics. Such knowledge would also help us calibrate our expectations for convection-permitting GCMs, whose ability to reduce uncertainty in cloud feedbacks is as yet unclear.

Progress thus seems to require a combination of bottom-up physics research, along with top-down studies aimed at guiding that research. To date both bottom-up and top-down approaches have of course been tried, but not always in concert. We hope that such an approach will finally bear fruit in solving the persistent puzzle of clouds and climate.

Appendix A

A.1 Comparison of two approaches to effective buoyancy

Solving (2.10) is not the only way to obtain the buoyant acceleration. One can use the momentum equation (2.4) and take its divergence to obtain a Poisson equation for p', which has $-\overline{\rho}\partial_z B$ as one of its source terms. One can then define a 'buoyancy perturbation pressure' p'_b as the solution to $-\nabla^2 p'_b = -\overline{\rho}\partial_z B$ (modulo ambiguous boundary conditions, see [49] pg. 29), and it can be shown (DJ03) that

$$a_b = B - (\partial_z p'_b)/\overline{\rho}\,. \tag{A.1}$$

Thus, one can compute a_b by computing B, solving $-\nabla^2 p'_b = -\overline{\rho}\partial_z B$, and then summing. This approach has been taken by other authors, e.g., [82] and [40]. Though the two approaches must yield the same result, they lend themselves to different interpretations. The $B - (\partial_z p'_b)/\overline{\rho}$ expression says that Archimedean buoyancy drives buoyant accelerations, and $-(\partial_z p'_b)/\overline{\rho}$ gives the environmental response. To analogously interpret a_b as computed via (2.10), we proceed as follows. We define a 'buoyant pressure' p_β (not to be confused with the buoyancy perturbation pressure p'_b) as the $p_{\rm nh}$ field resulting from zeroing out the wind fields, i.e. $p_\beta \equiv p_{\rm nh}|_{\mathbf{u}=0}$. It follows from (2.8) that

$$-\nabla^2 p_\beta = \nabla_h^2 p_{\rm h}, \tag{A.2}$$

and so $p_\beta$arises to enforce mass continuity in the face of horizontal hydrostatic pressure forces $-\nabla_h p_{\rm h}$. Furthermore, (A.2) implies $a_b = -\partial_z p_\beta/\rho$, and hence *the buoyant acceleration a_b can be seen as the vertical acceleration needed to compensate for horizontal motions driven by the hydrostatic pressure gradient*, as in the stack (or 'chimney') effect. The p_β field is discussed much further in Chapter 3.

We thus have two ways of thinking about the buoyant force. One significant disadvantage of the $B-(\partial_z p'_b)/\overline{\rho}$ approach is that it treats B as primary, even though B suffers significant arbitrariness due to its dependence on an arbitrary reference state (as pointed out in Section 2.2 and emphasized by [15]). The a_b approach does not suffer this ambiguity, and also lends itself to a straightforward derivation of (2.17).

A.2 Interpreting and calculating p_i

Defining and interpreting p_i

We mentioned in Section 2.2 that a_i can be viewed as the z-component of the gradient of an associated pressure, the *inertial pressure* p_i, defined here as

$$p_i \equiv p_{\rm nh}|_{\rho=\overline{\rho}}\,. \tag{A.3}$$

Applying this definition to (2.6) and taking its divergence yields the following Poisson equation for p_i:

$$-\nabla^2 p_i = \nabla\cdot[\overline{\rho}(\mathbf{u}\cdot\nabla)\mathbf{u}]. \tag{A.4}$$

Eqn. (2.7) yields Neumann BCs $\partial_z p_i = 0$ at model top and bottom. Applying $-\partial_z$ to both sides of this equation, comparing with (2.11), and noting that Neumann BCs for p_i imply Dirichlet BCs for $\partial_z p_i$ show that indeed $\overline{\rho}a_i = -\partial_z p_i$.

Eqn. (A.4) can be interpreted as enforcing the cancellation of the tendency of mass divergence generated by the inertial pressure with that generated by advection, in order to maintain anelastic continuity. In other words, *the p_i field produces whatever force is needed to ensure (anelastic) mass continuity in the face of the divergent tendencies generated by fluid inertia.*

To gain further intuition for p_i, we refer to [6] who showed that the source term $S_{\rm p_i}$, which we define to be the right hand side of (A.4), can be written (neglecting $\overline{\rho}$ variations) as

$$S_{\rm p_i} = \overline{\rho}\left(||\boldsymbol{e}||^2 - \frac{1}{2}||\boldsymbol{\omega}||^2\right), \tag{A.5}$$

where $\boldsymbol{e}$ is the strain tensor with components $e_{ij} = 1/2(\partial_i u_j + \partial_j u_i)$, $\boldsymbol{\omega}$ is the vorticity vector with components $\omega_i = \epsilon_{ijk}\partial_j u_k$, and the norm squared $||\cdot||^2$ of a vector or matrix denotes the sum of the squares of the components. Thus, strain is a source of positive pressure and vorticity a source of negative pressure.

We can understand this as follows. First consider a 2-D velocity field $\mathbf{u}$, vanishing at infinity, that, to first order around the origin, is given by the solid-body rotation field $\mathbf{u} = (-y, x)$ (Fig. A1(a)). If $\mathbf{u}$ is allowed to evolve solely under its own inertia, then, near the origin,

$$\partial_t\mathbf{u} = -(\mathbf{u}\cdot\nabla)\mathbf{u} = (x, y)\,.$$

In other words, $\mathbf{u}$ will develop a component pointing radially outward from the origin (Fig. A1(b)) as a consequence of the familiar centrifugal 'force'. *This advective tendency will cause a divergence of mass*, and since it is the job of p_i to generate a convergence of mass to counteract this, p_i must have a low at the origin. Thus, vorticity must be a source of negative p_i.

Next, consider another $\mathbf{u}$ field that vanishes at infinity but is given to first order at the origin by the irrotational field $\mathbf{u} = (-x, y)$ (Fig. A1(c)). This field converges along the x

axis and diverges along the y axis and thus has nonzero strain at the origin. If $\mathbf{u}$ is allowed to evolve solely under its own inertia, then, near the origin,

$$\partial_t \mathbf{u} = -(\mathbf{u}\cdot\nabla)\mathbf{u} = (-x,-y)\,.$$

In other words, $\mathbf{u}$ will develop a component pointing radially inward towards the origin (Fig. A1(d)). *This advective tendency will cause a convergence of mass*, and since it is the job of p_i to generate a divergence of mass to counteract this, p_i must have a high at the origin. Thus, strain must be a source of positive p_i.

Calculating p_i

When calculating the inertial pressure p_i, it is computationally expedient to rewrite $S_{\mathrm{p_i}}$ yet again to obtain the Poisson equation

$$-\nabla^2 p_i = \overline{\rho}(\partial_j u_i)(\partial_i u_j) - w^2\partial_z^2 \ln\overline{\rho}. \tag{A.6}$$

[The z-derivative of this is just the right-hand side of (2.14).] We solve (A.6) by first Fourier-transforming from (x,y) to $\vec{k}=(k_x,k_y)$ in the horizontal, periodic dimensions, which yields a set of algebraic equations for each $\vec{k}$ which are coupled only in z. This system can be written in terms of a $\vec{k}$-dependent tri-diagonal matrix which is (in general) easily inverted, whereupon we Fourier transform back and are done.

One issue that deserves further comment is that of the boundary conditions at model top ($z=z_t$) and model bottom ($z=0$). As noted above, p_i obeys the Neumann BCs

$$\partial_z p_i(z_t) = \partial_z p_i(0) = 0\,. \tag{A.7}$$

The rub is that these double Neumann BCs do not uniquely specify p_i, but only determine it up to a constant; thus these BCs are degenerate. This manifests computationally in a non-invertible tri-diagonal matrix for $\vec{k}=0$, i.e., the constant Fourier component $\overline{p_i}(z)$ (denoting horizontal averages with an overbar). We can thus keep our Neumann BCs for $\vec{k}\neq 0$ as well as for $\overline{p_i}$ at model bottom, and then specify our constant and remove the degeneracy by imposing the Dirichlet BC $\overline{p_i}(z_t)=0$ at model top. This, however, seems potentially inconsistent with (A.7), which implies $\partial_z\overline{p_i}(z_t)=0$ as well. Fortunately, the Poisson equation carries an integral constraint that saves the day. Integrating (A.4) over the entire domain, noting that the boundary of the domain consists of just the model top and bottom, and applying the divergence theorem yields

$$-\int\int dx\,dy\;\partial_z p_i\big|_0^{z_t} = \int\int dx\,dy\;\overline{\rho}(\mathbf{u}\cdot\nabla)w\,\big|_0^{z_t}\,. \tag{A.8}$$

The fact that $w\equiv 0$ at $z=0$ and $z=z_t$ implies that the right-hand side of (A.8) is zero. At the same time, one can recognize the left-hand side as $\partial_z\overline{p_i}(z_b)-\partial_z\overline{p_i}(z_t)$ times a constant. This yields the constraint

$$\partial_z\overline{p_i}(0) = \partial_z\overline{p_i}(z_t). \tag{A.9}$$

Thus, the Neumann BC at model bottom plus the constraint (A.8) implies that the Neumann BC holds at model top as well, *in addition* to our Dirichlet BC there.

As an aside, we should note here that numerically, the summed source term $\overline{\rho}(\partial_j u_i)(\partial_i u_j)$ on the right-hand side of (A.6) must be quite carefully computed in order for the constraint (A.9) to be obeyed. In particular, on an Arakawa C-grid [1] the terms with different (i, j) live at different points of the grid cell, but for a given (i, j) each factor $\partial_j u_i$ and $\partial_i u_j$ lives on the same point of the grid cell. To compute $S_{\mathrm{p_i}}$ one must interpolate each term to a common point before summing, but it is imperative to only perform this interpolation *after* multiplying $\partial_j u_i$ and $\partial_i u_j$ together. We found that interpolating before multiplying yielded a p_i field which did not obey (A.9).

Returning to analytics, we observe that one can, in fact, go beyond the constraint (A.9) and obtain an explicit expression for $\overline{p_i}$. We begin with the anelastic equation of motion

$$\overline{\rho}\frac{dw}{dt} = \overline{\rho}a_b - \partial_z p_i \tag{A.10}$$

and take a horizontal average over our domain with area A. We evaluate $\overline{\rho a_b}$ by applying a horizontal average to (2.10), which yields $-\partial_z^2(\overline{\rho a_b}) = \overline{g\nabla_h^2 \rho} = 0$. This, along with the BCs $a_b(0) = a_b(z_t) = 0$, implies $\overline{a_b} = 0$. Meanwhile, mass continuity implies $\overline{\rho}\frac{\partial \overline{w}}{\partial t} = 0$. Applying these results to the horizontal average of (A.10) yields

$$-\partial_z \overline{p_i} = \frac{1}{A}\int\int dx\, dy\, \overline{\rho}(\mathbf{u}\cdot\nabla)w = \frac{1}{A}\int\int dx\, dy\, \partial_i(\overline{\rho}u^i w) = \partial_z \overline{\rho w^2}.$$

Integrating down from model top then shows that

$$\overline{p_i} = -\overline{\rho w^2}. \tag{A.11}$$

We can interpret this equation as follows. The quantity $\overline{\rho w^2}$ is simply the domain-averaged flux of vertical momentum $\overline{\rho w}$. The convergence $-\partial_z \overline{\rho w^2}$ of this flux is a force, namely the rate at which inertial motions generate $\overline{\rho w}$. Continuity dictates that $\overline{\rho w} \equiv 0$, however, and so (A.11) just says that $\overline{p_i}$ provides the force necessary to ensure this, in consonance with our discussion in the last section.

As a final note, (A.11) and the Dirichlet BCs on w show that $\overline{p_i}$ obeys *both* Neumann and Dirichlet BCs, and so either (or a mix) may be used in practice. Also, the relation (A.11) serves as a useful diagnostic constraint against which one may check their calculation of p_i.

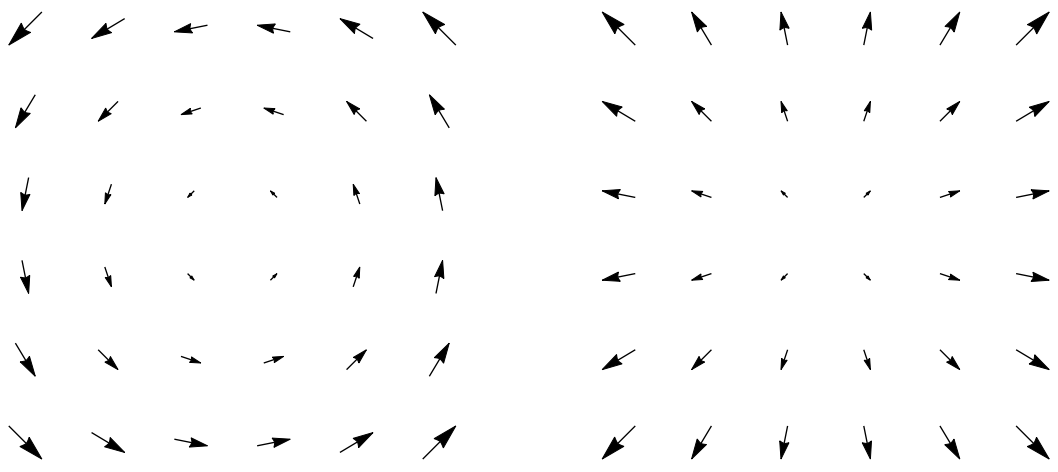

(a) $\mathbf{u} = (-y, x)$ **(b)** $-(\mathbf{u} \cdot \nabla)\mathbf{u} = (x, y)$

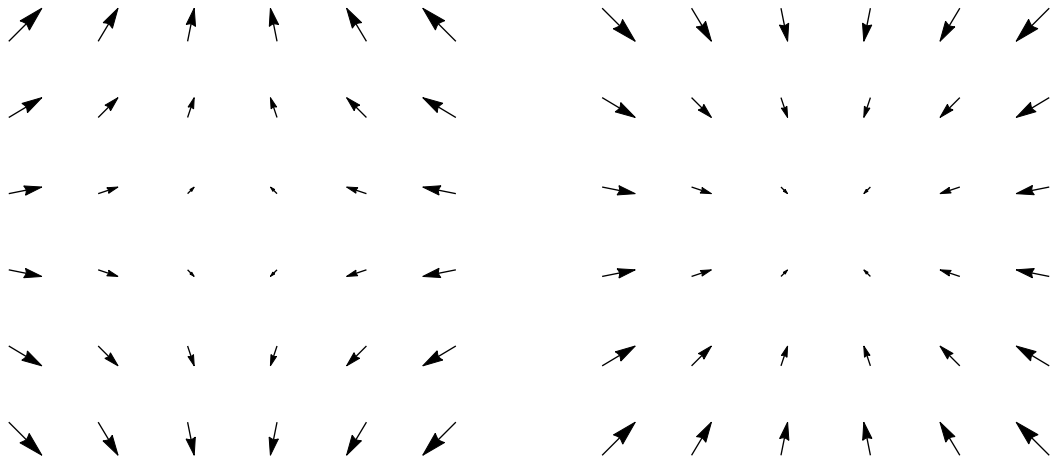

(c) $\mathbf{u} = (-x, y)$ **(d)** $-(\mathbf{u} \cdot \nabla)\mathbf{u} = (-x, -y)$

Figure A.1: Idealized vector fields and their advective tendencies. Panel **(a)** shows a pure rotational flow, while **(b)** shows its divergent advective tendency. Similarly, **(c)** shows a pure (irrotational) strain flow and **(d)** its convergent advective tendency. The inertial pressure p_i balances these tendencies by generating a low (high) at the origin in the case of pure rotation (strain).

Appendix B

B.1 The invariance of $p_\beta/p_\beta(0)$ in the $D/H \gg 1$ limit

Consider the free cylinder's buoyancy distribution, Eqn. (3.7). Setting $\mathbf{x}' = \mathbf{x}/D$ we can write this as

$$B(\mathbf{x}') = B_0\,\mathcal{H}(1/2 - r')\;\mathcal{H}(z' + H/2D)\;\mathcal{H}(H/2D - z')\;.$$

In the $D/H \gg 1$ limit the product of the last two Heaviside functions becomes a delta function $(H/D)\delta(z')$, i.e. the cylinder becomes a horizontal 'line source' in the primed coordinates. Feeding this B field into the definition of $p_{\rm hyd}$ and employing Eqns. (3.13) and (3.14) yields

$$-\nabla'^2\left(\frac{p_\beta}{p_\beta(0)}\right) = -2\mathcal{H}(-z')\nabla_h'^2\,\mathcal{H}\left(\frac{1}{2} - r'\right)\;. \tag{B.1}$$

This tells us that $p_\beta/p_\beta(0)$ is an invariant function of $\mathbf{x}'$, insensitive to changes in H and D within the $D/H \gg 1$ regime. In particular, we conclude that $p_\beta/p_\beta(0)$ will decay along the z-axis to a given fraction of itself at a fixed $z' = z/D$, and hence this 'scale height' of p_β scales with D.

Repeating this exercise but for the surface cylinder (or for a cylinder close to the surface, i.e. $z_{\rm cm} \ll D$) yields an expression identical to (B.1), except with the replacement $\mathcal{H}(-z') \to \delta(z')$. In this case, we conclude that both the scale height as well as the height $z_{\rm max}$ of maximum β scale with D.

Bibliography

[1] Akio Arakawa and Vivian R. Lamb. *General Circulation Models of the Atmosphere*. Elsevier Science, 2012, p. 348.

[2] G. K. Batchelor. *An Introduction to Fluid Dynamics*. Cambridge University Press, 2000, p. 615.

[3] Peter G. Black. "Mesoscale Cloud Patterns Revealed by Apollo-Soyuz Photographs". EN. In: *Bulletin of the American Meteorological Society* 59.11 (Nov. 1978), pp. 1409–1419.

[4] Steven J. Böing et al. "Influence of the Subcloud Layer on the Development of a Deep Convective Ensemble". In: *Journal of the Atmospheric Sciences* 69.9 (2012), pp. 2682–2698.

[5] O Boucher et al. "7. Clouds and Aerosols". In: *Climate Change 2013: The Physical Science Basis. Contribution of Working Group I to the Fifth Assessment Report of the Intergovernmental Panel on Climate Change* (2013), pp. 571–657.

[6] P. Bradshaw. "A note on Poisson's equation for pressure in a turbulent flow". In: *Physics of Fluids* 24.4 (Apr. 1981), p. 777.

[7] Christopher S. Bretherton, Peter N. Blossey, and Marat F. Khairoutdinov. "An Energy-Balance Analysis of Deep Convective Self-Aggregation above Uniform SST". In: *Journal of the Atmospheric Sciences* 62.12 (2005), pp. 4273–4292.

[8] Christopher S. Bretherton and James R. McCaa. "A New Parameterization for Shallow Cumulus Convection and Its Application to Marine Subtropical Cloud-Topped Boundary Layers. Part II: Regional Simulations of Marine Boundary Layer Clouds". In: *Monthly Weather Review* 132.4 (2004), pp. 883–896.

[9] Douglas R. Brumley, Michelle Willcox, and John E. Sader. "Oscillation of cylinders of rectangular cross section immersed in fluid". In: *Physics of Fluids* 22.5 (May 2010), p. 052001.

[10] Jule Charney et al. *Carbon Dioxide and Climate: A Scientific Assessment*. Tech. rep. National Academy of Sciences, Washington DC, 1979.

[11] W. Brian Dade and Herbert E. Huppert. "A box model for non-entraining, suspension-driven gravity surges on horizontal surfaces". In: *Sedimentology* 42.3 (June 1995), pp. 453–470.

[12] Phanindramohan Das. *A Non-Archimedean Approach to the Equations of Convection Dynamics*. 1979.

[13] Robert Davies-Jones. "An Expression for Effective Buoyancy in Surroundings with Horizontal Density Gradients". In: *Journal of the Atmospheric Sciences* 60.23 (2003), pp. 2922–2925.

[14] Anthony D. Del Genio et al. "Constraints on Cumulus Parameterization from Simulations of Observed MJO Events". EN. In: *Journal of Climate* 28.16 (Aug. 2015), pp. 6419–6442.

[15] Charles a. Doswell and Paul M. Markowski. "Is Buoyancy a Relative Quantity?" In: *Monthly Weather Review* 132.4 (2004), pp. 853–863.

[16] Kelvin K. Droegemeier and Robert B. Wilhelmson. *Three-Dimensional Numerical Modeling of Convection Produced by Interacting Thunderstorm Outflows. Part I: Control Simulation and Low-Level Moisture Variations*. 1985.

[17] Dale R. Durran. *Numerical Methods for Fluid Dynamics: With Applications to Geophysics*. Springer Science & Business Media, 2010, p. 532.

[18] Gregory Falkovich. *Fluid Mechanics: A Short Course for Physicists*. Cambridge University Press, 2011.

[19] Zhe Feng et al. "Mechanisms of convective cloud organization by cold pools over tropical warm ocean during the AMIE/DYNAMO field campaign". In: *Journal of Advances in Modeling Earth Systems* 7.2 (June 2015), pp. 357–381.

[20] Carl A. Friehe and Kurt F. Schmitt. *Parameterization of Air-Sea Interface Fluxes of Sensible Heat and Moisture by the Bulk Aerodynamic Formulas*. 1976.

[21] J. M. Fritsch, R. J. Kane, and C. R. Chelius. "The Contribution of Mesoscale Convective Weather Systems to the Warm-Season Precipitation in the United States". EN. In: *Journal of Climate and Applied Meteorology* 25.10 (Oct. 1986), pp. 1333–1345.

[22] Wojciech W. Grabowski and Mitchell W. Moncrieff. "Large-scale organization of tropical convection in two-dimensional explicit numerical simulations". In: *Quarterly Journal of the Royal Meteorological Society* 127.572 (Jan. 2001), pp. 445–468.

[23] Jean-Yves Grandpeix and Jean-Philippe Lafore. "A Density Current Parameterization Coupled with Emanuel's Convection Scheme. Part I: The Models". EN. In: (May 2010).

[24] Jean-Yves Grandpeix, Jean-Philippe Lafore, and Frédérique Cheruy. "A Density Current Parameterization Coupled with Emanuel's Convection Scheme. Part II: 1D Simulations". EN. In: (May 2010).

[25] David J. Griffiths. *Introduction to Electrodynamics*. Pearson Education, 2014, p. 625.

[26] J. Hacker, P.F. Linden, and S.B. Dalziel. "Mixing in lock-release gravity currents". In: *Dynamics of Atmospheres and Oceans* 24.1-4 (Jan. 1996), pp. 183–195.

[27] T. C. Harris, A. J. Hogg, and H. E. Huppert. "A mathematical framework for the analysis of particle-driven gravity currents". In: *Proceedings of the Royal Society A: Mathematical, Physical and Engineering Sciences* 457.2009 (May 2001), pp. 1241–1272.

[28] Dennis L. Hartmann. *Global Physical Climatology*. Newnes, 2015, p. 498.

[29] Andrew J. Hogg, Mark A. Hallworth, and Herbert E. Huppert. "On gravity currents driven by constant fluxes of saline and particle-laden fluid in the presence of a uniform flow". English. In: *Journal of Fluid Mechanics* 539.-1 (Sept. 2005), p. 349.

[30] James R. Holton and Gregory J Hakim. *An Introduction to Dynamic Meteorology*. Academic Press, 2012, p. 552.

[31] Robert A. Houze and Alan K. Betts. "Convection in GATE". In: *Reviews of Geophysics* 19.4 (1981), p. 541.

[32] Robert A. Houze and Jr. *Cloud Dynamics*. Academic Press, 2014, p. 496.

[33] H. E. Huppert. "Quantitative modelling of granular suspension flows". In: *Philosophical Transactions of the Royal Society A: Mathematical, Physical and Engineering Sciences* 356.1747 (Nov. 1998), pp. 2471–2496.

[34] Herbert E. Huppert and John E. Simpson. "The slumping of gravity currents". English. In: *Journal of Fluid Mechanics* 99.04 (Apr. 2006), p. 785.

[35] IPCC. "Summary for Policymakers". In: *Climate Change 2013: The Physical Science Basis. Contribution of Working Group I to the Fifth Assessment Report of the Intergovernmental Panel on Climate Change* (2013), p. 33.

[36] Marat F. Khairoutdinov and K. Emanuel. "Aggregated Convection and the Regulation of Tropical Climate". In: *29th Conference on Hurricanes and Tropical Meteorology* (2010), P2.69.

[37] Marat F. Khairoutdinov and David a. Randall. "Cloud Resolving Modeling of the ARM Summer 1997 IOP: Model Formulation, Results, Uncertainties, and Sensitivities". In: *Journal of the Atmospheric Sciences* 60.4 (2003), pp. 607–625.

[38] Joseph B. Klemp and Richard Rotunno. "A Study of the Tornadic Region within a Supercell Thunderstorm". EN. In: *Journal of the Atmospheric Sciences* 40.2 (Feb. 1983), pp. 359–377.

[39] S. K. Krueger, G. T. McLean, and Quiang Fu. "Numerical simulation of the stratus-to-cumulus transition in the subtropical marine boundary layer. Part II: boundary-layer circulation". en. In: *Oceanographic Literature Review* 3.43 (1996), p. 228.

[40] Steven K. Krueger et al. "Improvements of an Ice-Phase Microphysics Parameterization for Use in Numerical Simulations of Tropical Convection". EN. In: *Journal of Applied Meteorology* 34 (Mar. 1995), pp. 281–287.

[41] Zhiming Kuang and Christopher S. Bretherton. "A Mass-Flux Scheme View of a High-Resolution Simulation of a Transition from Shallow to Deep Cumulus Convection". In: *Journal of the Atmospheric Sciences* 63.7 (2006), pp. 1895–1909.

[42] Wolfgang Langhans and David M. Romps. "The origin of water vapor rings in tropical oceanic cold pools". In: *Geophysical Research Letters* (2015).

[43] Jia-Lin Lin et al. "Tropical Intraseasonal Variability in 14 IPCC AR4 Climate Models. Part I: Convective Signals". EN. In: (Feb. 2010).

[44] Yuh-Lang Lin, Richard D. Farley, and Harold D. Orville. *Bulk Parameterization of the Snow Field in a Cloud Model*. 1983.

[45] Roland List and Edward P. Lozowski. "Pressure Perturbations and Buoyancy in Convective Clouds". EN. In: *Journal of the Atmospheric Sciences* 27.1 (Jan. 1970), pp. 168–170.

[46] Stephen J. Lord, Hugh E. Willoughby, and Jacqueline M. Piotrowicz. "Role of a Parameterized Ice-Phase Microphysics in an Axisymmetric, Nonhydrostatic Tropical Cyclone Model". EN. In: *Journal of the Atmospheric Sciences* 41.19 (Oct. 1984), pp. 2836–2848.

[47] Brian E. Mapes. "Convective Inhibition, Subgrid-Scale Triggering Energy, and Stratiform Instability in a Toy Tropical Wave Model". EN. In: *Journal of the Atmospheric Sciences* 57.10 (May 2000), pp. 1515–1535.

[48] L. G. Margolin, W. J. Rider, and F. F. Grinstein. "Modeling turbulent flow with implicit LES". en. In: *Journal of Turbulence* 7 (Jan. 2006), N15.

[49] Paul Markowski and Yvette Richardson. *Mesoscale Meteorology in Midlatitudes*. John Wiley & Sons, 2011, p. 430.

[50] Thorsten Mauritsen and Bjorn Stevens. "Missing iris effect as a possible cause of muted hydrological change and high climate sensitivity in models". In: *Nature Geoscience* 8.April (2015), pp. 8–13.

[51] Saroj K. Mishra. "Influence of convective adjustment time scale on the tropical transient activity". In: *Meteorology and Atmospheric Physics* 114.1 (2011), pp. 17–34.

[52] Saroj K. Mishra and J. Srinivasan. "Sensitivity of the simulated precipitation to changes in convective relaxation time scale". In: *Annales Geophysicae* 28.10 (2010), pp. 1827–1846.

[53] Eli J. Mlawer et al. "Radiative transfer for inhomogeneous atmospheres: RRTM, a validated correlated-k model for the longwave". In: *Journal of Geophysical Research* 102.D14 (July 1997), p. 16663.

[54] Caroline J. Muller and Isaac M. Held. "Detailed Investigation of the Self-Aggregation of Convection in Cloud-Resolving Simulations". In: *Journal of the Atmospheric Sciences* 69.8 (2012), pp. 2551–2565.

[55] Richard B. Neale et al. "The Mean Climate of the Community Atmosphere Model (CAM4) in Forced SST and Fully Coupled Experiments". In: *Journal of Climate* 26.14 (2013), pp. 5150–5168.

[56] Alison D. Nugent and Ronald B. Smith. "Initiating Moist Convection in an Inhomogeneous Layer by Uniform Ascent". In: *Journal of the Atmospheric Sciences* 71.12 (2014), pp. 4597–4610.

[57] Matthew D. Parker and Richard H. Johnson. "Organizational Modes of Midlatitude Mesoscale Convective Systems". In: *Monthly Weather Review* 128.10 (2000), pp. 3413–3436.

[58] Olivier Pauluis and Stephen Garner. "Sensitivity of Radiative Convective Equilibrium Simulations to Horizontal Resolution". In: *Journal of the Atmospheric Sciences* 63.7 (2006), pp. 1910–1923.

[59] Andreas F. Prein. "A review on regional convection-permitting climate modeling: Demonstrations, prospects, and challenges". In: *Reviews of Geophysics* (2015), pp. 1–39.

[60] Liying Qian, George S. Young, and William M. Frank. "A Convective Wake Parameterization Scheme for Use in General Circulation Models". EN. In: *Monthly Weather Review* 126.2 (Feb. 1998), pp. 456–469.

[61] Yun Qian et al. "Parametric sensitivity analysis of precipitation at global and local scales in the Community Atmosphere Model CAM5". In: *Journal of Advances in Modeling Earth Systems* 7.2 (June 2015), pp. 382–411.

[62] Catherine Rio et al. "Control of deep convection by sub-cloud lifting processes: the ALP closure in the LMDZ5B general circulation model". In: *Climate Dynamics* 40.9-10 (Sept. 2012), pp. 2271–2292.

[63] David M. Romps. "The Dry-Entropy Budget of a Moist Atmosphere". In: *Journal of the Atmospheric Sciences* 65.12 (2008), pp. 3779–3799.

[64] David M. Romps and Alexander B. Charn. "Sticky Thermals: Evidence for a Dominant Balance between Buoyancy and Drag in Cloud Updrafts". In: *Journal of the Atmospheric Sciences* 72.8 (2015), pp. 2890–2901.

[65] David M. Romps and Zhiming Kuang. "Do Undiluted Convective Plumes Exist in the Upper Tropical Troposphere?" In: *Journal of the Atmospheric Sciences* 67 (2010), pp. 468–484.

[66] David M. Romps and Rusen Öktem. "Stereo photogrammetry reveals substantial drag on cloud thermals". In: *Geophysical Research Letters* May (2015).

[67] Stephan R. de Roode et al. "Parameterization of the Vertical Velocity Equation for Shallow Cumulus Clouds". In: *Monthly Weather Review* 140.8 (2012), pp. 2424–2436.

[68] Wim C. de Rooy et al. "Entrainment and detrainment in cumulus convection: an overview". In: *Quarterly Journal of the Royal Meteorological Society* 139.670 (Jan. 2013), pp. 1–19.

[69] A. N. Ross, Adrian M. Tompkins, and D. J. Parker. "Simple Models of the Role of Surface Fluxes in Convective Cold Pool Evolution". In: *Journal of the Atmospheric Sciences* 61.13 (2004), pp. 1582–1595.

[70] Richard Rotunno and Joseph Klemp. "On the Rotation and Propagation of Simulated Supercell Thunderstorms". EN. In: *Journal of the Atmospheric Sciences* 42.3 (Feb. 1985), pp. 271–292.

[71] John J. Rozbicki, George S. Young, and Liying Qian. "Test of a Convective Wake Parameterization in the Single-Column Version of CCM3". EN. In: *Monthly Weather Review* 127.6 (June 1999), pp. 1347–1361.

[72] Russ S. Schumacher and Richard H. Johnson. "Organization and Environmental Properties of Extreme-Rain-Producing Mesoscale Convective Systems". EN. In: (Feb. 2010).

[73] Steven C. Sherwood et al. "Slippery Thermals and the Cumulus Entrainment Paradox*". EN. In: *Journal of the Atmospheric Sciences* 70.8 (Aug. 2013), pp. 2426–2442.

[74] A. Pier Siebesma et al. "A Large Eddy Simulation Intercomparison Study of Shallow Cumulus Convection". EN. In: *Journal of Atmospheric Sciences* 60 (Feb. 2003), pp. 1201–1219.

[75] Graeme L. Stephens, Susan van den Heever, and Lyle Pakula. "Radiative Convective Feedbacks in Idealized States of Radiative Convective Equilibrium". In: *Journal of the Atmospheric Sciences* 65.12 (2008), pp. 3899–3916.

[76] Karl E. Taylor, Ronald J. Stouffer, and Gerald A. Meehl. "An Overview of CMIP5 and the Experiment Design". EN. In: *Bulletin of the American Meteorological Society* 93.4 (Apr. 2012), pp. 485–498.

[77] Isabelle Tobin, Sandrine Bony, and Remy Roca. "Observational evidence for relationships between the degree of aggregation of deep convection, water vapor, surface fluxes, and radiation". In: *Journal of Climate* 25.20 (2012), pp. 6885–6904.

[78] Adrian M. Tompkins. "Organization of Tropical Convection in Low Vertical Wind Shears: The Role of Cold Pools". In: *Journal of the Atmospheric Sciences* 58.13 (2001), pp. 1650–1672.

[79] Giuseppe Torri, Zhiming Kuang, and Yang Tian. "Mechanisms for convection triggering by cold pools". In: *Geophysical Research Letters* (2015), pp. 1–8.

[80] Xiaocong Wang and Minghua Zhang. "Vertical velocity in shallow convection for different plume types". In: *Journal of Advances in Modeling Earth Systems* 6.2 (June 2014), pp. 478–489.

[81] Morris L. Weisman and Richard Rotunno. "'A Theory for Strong Long-Lived Squall Lines', Revisited". EN. In: *Journal of the Atmospheric Sciences* 61.4 (Feb. 2004), pp. 361–382.

[82] Kuan-Man Xu and David A. Randall. "Updraft and Downdraft Statistics of Simulated Tropical and Midlatitude Cumulus Convection". EN. In: *Journal of the Atmospheric Sciences* 58.13 (July 2001), pp. 1630–1649.

[83] G.J. Zhang and Norman a. McFarlane. "Sensitivity of climate simulations to the parameterization of cumulus convection in the Canadian climate centre general circulation model". In: *Atmosphere-Ocean* 33.3 (1995), pp. 407–446.

[84] Paquita Zuidema et al. "On Trade Wind Cumulus Cold Pools". EN. In: *Journal of the Atmospheric Sciences* 69.1 (Jan. 2012), pp. 258–280.